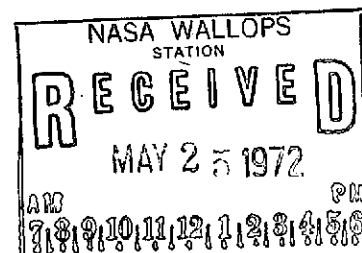# R E S E A R C H   T R I A N G L E   I N S T I T U T E
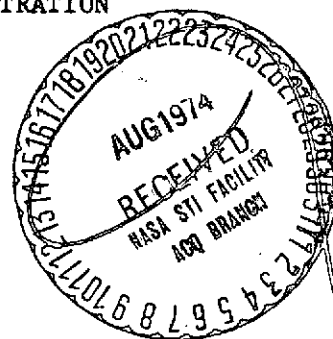
ANALYSIS OF SATELLITE ALTIMETER SIGNAL

CHARACTERISTICS AND INVESTIGATION OF SEA-TRUTH

DATA REQUIREMENTS

Final Engineering Report

April 1972

Prepared Under

NASA CONTRACT NO. NAS6-1952

for

NATIONAL AERONAUTICS AND SPACE ADMINISTRATION

WALLOPS STATION

WALLOPS ISLAND, VIRGINIA 23337

R E S E A R C H   T R I A N G L E   P A R K ,   N O R T H   C A R O L I N A   27709

159

ANALYSIS OF SATELLITE ALTIMETER SIGNAL

CHARACTERISTICS AND INVESTIGATION OF SEA-TRUTH

DATA REQUIREMENTS

Final Engineering Report

April 1972

Prepared Under

NASA CONTRACT NO. NAS6-1952

for

NATIONAL AERONAUTICS AND SPACE ADMINISTRATION

WALLOPS STATION

WALLOPS ISLAND, VIRGINIA 23337

FOREWORD

This report was prepared for the National Aeronautics and Space Administration by The Research Triangle Institute under Contract No. NAS6-1952. Messrs J. T. McGoogan and H. R. Stanley of NASA/Wallops Station acted as technical coordinators of the contract.

The study was performed by the Engineering Division of the Institute. The project staff consisted of Drs. L. S. Miller (Project Leader), G. S. Hayne, and G. S. Brown. Professors W. A. Flood and N. H. Huang of the North Carolina State University at Raleigh provided contributions to Chapter 4 of this report. E. L. Hofmeister of the General Electric Company, Utica, New York provided valuable assistance through numerous informal discussions.

ABSTRACT

This report presents the results of analysis of satellite signal
characteristics as influenced by ocean surface roughness and an inves-
tigation of sea-truth data requirements. The first subject treated is
that of post-flight waveform reconstruction for the Skylab S-193 radar
altimeter. Sea-state estimation accuracies are derived based on analytical
and hybrid computer simulation techniques. An analysis of near-normal
incidence, microwave backscattering from the ocean's surface is accomplished
in order to obtain the minimum sea-truth data necessary for good agreement
between theoretical and experimental scattering results. Sea-state bias
is examined from the point of view of designing an experiment which will
lead to a resolution of the problem. The report concludes with a discussion
of some deficiencies which were found in the theory underlying the Stilwell
technique for spectral measurements.

CONTENTS

CONTENTS (Continued)

CHAPTER 1

INTRODUCTION AND SUMMARY OF RESULTS

1.0 SCOPE OF THE REPORT

This report presents analyses of several technical factors related to geodetic altimetry. The categories which are covered comprise radar systems analysis, electromagnetic scattering analysis and investigation of sea truth measurement techniques. This study is largely motivated by requirements for experiment planning, development of post flight data processing methods, identification of potential sea-truth acquisition methods, and to yield a better understanding of the measurement characteristics of the two presently planned NASA geodetic satellite programs: the Skylab S-193 radar altimeter and the GEOS-C satellite.

Chapter 2 of this report examines the errors which arise from measurement process uncertainties, characteristics of the altimeter sampled data, considerations of the ground-based waveform reconstruction, and computational aspects of sea state extraction in a short pulse radar system. Details of a hybrid computer simulation of sea scattering and the geodetic altimeter system, upon which much of the results cited in Chapter 2 are based, are also given.

Chapter 3 examines the theoretical characteristics and sea-truth requirements of an experiment to investigate near-normal incidence, microwave backscattering. Specifically, the relationship between the ocean surface wavenumber spectrum and the radar cross-section per unit scattering area, σ^o, is calculated via the physical optics integral. We initially investigate σ^o as a function of surface wave height or wind speed and then determine the ocean surface wavenumber range which provides the major contribution to σ^o for isotropic, equilibrium ocean spectral conditions. Finally, the effects of ocean spectral anisotropy are considered.

Chapter 4 first examines the sea state bias problem, i.e., the difference that may exist between the radar observed wave height distribution and the true geometrical distribution. The characteristics of several currently used techniques for obtaining oceanographic information, especially as they relate to the bias problem, are then investigated. These techniques include near-surface radar measurements, sterographic photography, and the Stilwell method for obtaining ocean spectral information.

1.1 Conclusions and Recommendations

The following paragraphs provide a concise summary of the principal findings of this study. The interested reader is encouraged to examine the detailed conclusions contained in each section.

(1) The S-193 system is found to be capable of distinguishing ocean surface roughness values of 1/2 meter rms from values of 1 meter, for a data accumulation period of $\sim$10 seconds. In Significant Wave Height $(H_{1/3})$ units the corresponding figures are: 6.6 feet and 13.2 feet. For rougher seas the situation improves; a change of 3.3 feet may be distinguished for seas of 26.4 feet SWH (2 meters rms). These results indicate that major sea-state experimentation with the S-193 system should emphasize ocean areas characterized by rough seas, such as the North Atlantic. In the mid-latitudes it is possible that surface roughness changes during experimental periods will not be resolvable.

(2) We find that characteristics of the S-193 waveform and altitude data sampling processes are important contributors to the total system response, and ground based data processing techniques should be developed based on intimate knowledge of these hardware characteristics. For future satellite systems, we recommend sampling rates of at least four times the reciprocal pulse length with commensurate aperture periods. For 10 ns experiments this entails an advancement in the sampling art, in view of the power and size constraints present. More extensive altitude data sampling is required for systems in which sampling events are tied to the altitude tracker circuitry, for unambiguous data reconstruction. There are, at present, two information deficiencies relative to development of experiment software: measurements are needed on the S-193 hardware to (1) describe the differences between the sample-and-hold positioning functions and the altitude data output, and (2) provide information relative to the impulse response of the entire system including the sampling functions. A z-transform computational method is given which will allow derivation of the radar

observed wave height distribution from altimeter waveform information. Considerably more work remains to be done in regard to waveform reconstruction, because of the appreciable quantization noise present (which implies that the problem is not strictly one of classical sampled data reconstruction).

(3) Using a physical optics theory for 3 cm rf wavelength scattering at normal incidence from an ocean described by a Phillips type of equilibrium spectrum, it has been found that σ^o depends heavily on surface wavenumbers in the range .001 - 1.0 cm^{-1}, or ocean surface wavelengths of .06 - 60 meters, for surface winds $\leq$ 14 knots. This means that any σ^o experimentation must include acquisition of gravity wave-range spectral information, not the often-assumed capillary range, as sea-truth data for σ^o experimentation. The analysis also predicts negative results for σ^o vs. wind speed experiments since a saturation effect is found in the normal incidence case, similar to the effect noted by Guinard for scatterometer geometry. The Skylab σ^o experiment should provide a most valuable data base for this effect. Near-normal incidence scattering is found to be very insensitive to spectral anisotropy.

(4) Chapter 4 presents our interpretation of the nanosecond radar observations of Yaplee, et al. which indicates that the backscattering cross-section of the ocean's surface increases in a nearly linear fashion with increasing distance below the wave crests. We also discuss other methods of obtaining information related to the bias problem, particularly those which will shed light on the physical mechanism giving rise to the sea state bias effect. We conclude that only stereo photographs or a moving profilometer can acquire the desired information, and the laser profilometer is the more promising of these. Finally, our investigation of the Stilwell technique encountered several deficiencies in the theory underlying the method. For example we find that a false directionality exists in the derived spectrum. Because of these deficiencies we feel that the Stilwell technique should not, at present, be used as a primary source of sea-truth information.

CHAPTER 2

ANALYSIS OF THE CHARACTERISTICS OF ALTIMETER WAVEFORM
INFORMATION AND DATA PROCESSING CONSIDERATIONS

2.0 GENERAL DISCUSSION OF THE OCEAN SURFACE RESOLUTION CAPABILITIES OF
THE SKYLAB ALTIMETER

The objectives of this chapter are to provide information needed in
developing ground processing techniques for the Skylab S-193 waveform ex-
periments and to provide guidelines for the GEOS sampling problem. Speci-
fically the problem of measurement of ocean surface roughness through the
dependence of the received altimeter wave shapes upon ocean surface roughness
conditions is considered. In this discussion, it will be assumed that the
reader is generally familiar with the impulse response or waveform method of
surface roughness estimation [1]. Also, the terms "sea state" and "surface
roughness" will be used interchangeably, although it is recognized that sea
state is not a precise term. For cases in which quantitative descriptions are
needed, the terms "rms surface roughness" will be used. In the analysis, both
closed form and hybrid computer simulation results will be utilized. Details
of the computer simulation are given in section 2.3.

The principal problem areas to be considered in the impulse response
measurement process are as follows:

(a) The fluctuating received waveform requires that a large number of
individual waveforms must be averaged in order to estimate the
ensemble-mean waveform. Because of the limited number of waveforms
available per unit time and the limited region over which the ocean
surface can be regarded as homogeneous, the sea state measurement
process represents an attempt at estimating waveform fine structure
which is on the same scale as the uncertainty arising from the finite
averaging process. This problem is illustrated by the data shown in
Figure 1 and Figure 2. Figure 1 shows a Skylab waveform which
was obtained by averaging 100 individual waveforms. Figure 2
contains an overlay of five independently averaged waveforms, each
consisting of 100 sample averages.

(b) Altimeter hardware constraints are such that sampling operations and
bandpass characteristics significantly affect the waveform resolution
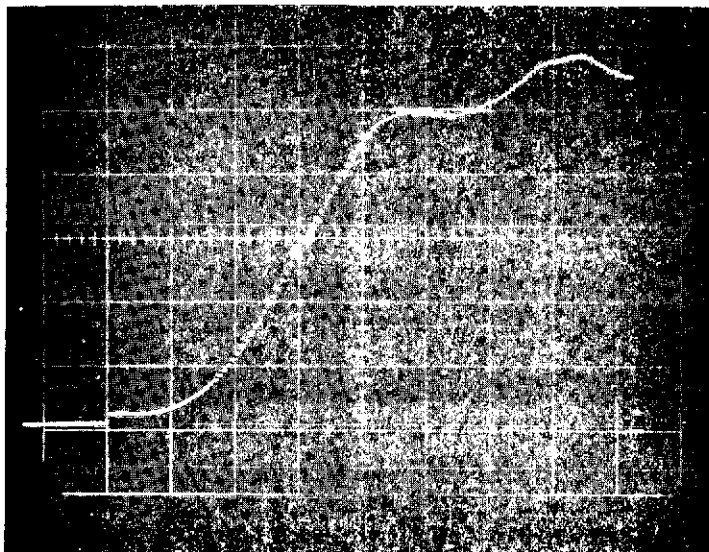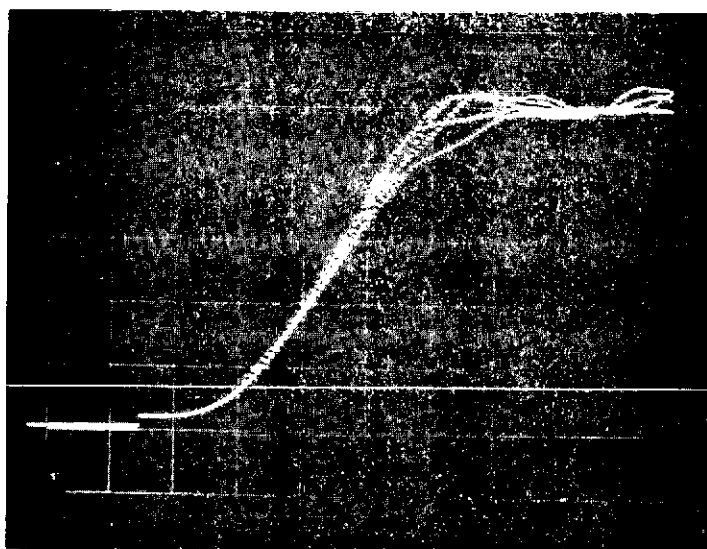
2-1

Figure 1. Signal only, single 100 sample case

Figure 2. Signal only, 5 independent 100 sample cases

Simulated mean waveforms obtained by averaging 100 individual waveforms (simulated sweep rate 2.5 ns/cm).

achievable. If the received waveforms are not adequately and reliably sampled, no degree of ground-based reconstruction can overcome this deficiency. As will be obvious in the following text, detailed knowledge of the system characteristics is required to support even qualitative estimates of ocean surface roughness resolution achievable with radar altimeters.

This chapter is organized in the following manner. The problem of reconstructing the time of occurrence of the waveform sampling events is first considered. In the S-193 system the sample functions are not fixed in time and the problem is to determine the extent to which the instantaneous sample-and-hold positions can be determined from the post-flight data. Next, characteristics of the zero sea-state response of the S-193 system are examined and this informatin is used to identify appropriate waveform reconstruction algorithms, estimate sensitivity of the sea state measurement process, specify experimental conditions matched to instrument capabilities, and examine data processing requirements.

2.1 Position Uncertainty of S-193 Waveform Sample Values

This section considers details of the waveform sampling process and discusses the S-193 system in the following context:

(1) Since the sample-and-hold circuits are positioned by the altitude tracking loop, what is the variance of the gate positioning process?

(2) What is the granularity of the gate positioning function?

(3) What is the expected location of the waveform leading edge relative to the sample-and-hold array? Over a typical sea-state experiment interval (approximately 10 seconds) will a significant percentage of the sample-and-hold measurements be outside the waveform region of interest (the signal "rise-time" region)?

(4) To what extent can the instantaneous sample-and-hold positions be defined in post-flight data?

Answers to these questions will permit specification of the effective number and spacing of the sampling events per unit time.

Beginning with category (1) above, a block diagram of the S-193 altitude tracking loop is shown in Figure 3. Note that the sample-and-hold circuits are positioned by the tracking gate generator and that altitude jitter in the tracking loop will result in corresponding positional jitter in the sample-and-hold circuit. Also note that the altitude data is sampled at approximately 8 per second (128 ms spacing), and that the altitude accumulator outputs the arithmetic average of the values over the 128 ms period. In the actual system, the tracking loop effectively averages over the returns from 4 pulses, and the accumulator then averages over the 8 groups of 4-pulse averages contained in the 128 ms time period. Assuming that the altitude accumulator is cleared after each sampling operation, each altitude sample constitutes a moving window average of the tracker excursions. These samples can then be filtered (although they are statistically dependent, due to the loop filter) to yield altitude data averaged over some other time interval such as a one second interval. The standard deviation of the sample-and-hold position jitter, σ_t (or, equivalently, the tracking error), may be estimated for the S-193 by the equation

$$\sigma_t = \frac{T}{\sqrt{\frac{PRF}{\pi B_1}}} \sqrt{\frac{7}{6} + \frac{6}{SNR} + \frac{8}{SNR^2}} \tag{1}$$

where T = width of early and late gates

SNR = signal to receiver IF noise ratio

PRF = pulse repetition frequency

B_1 = 3 db closed loop bandwidth,

and from other data, given in Ref. [2]. These data are summarized in Table 1.
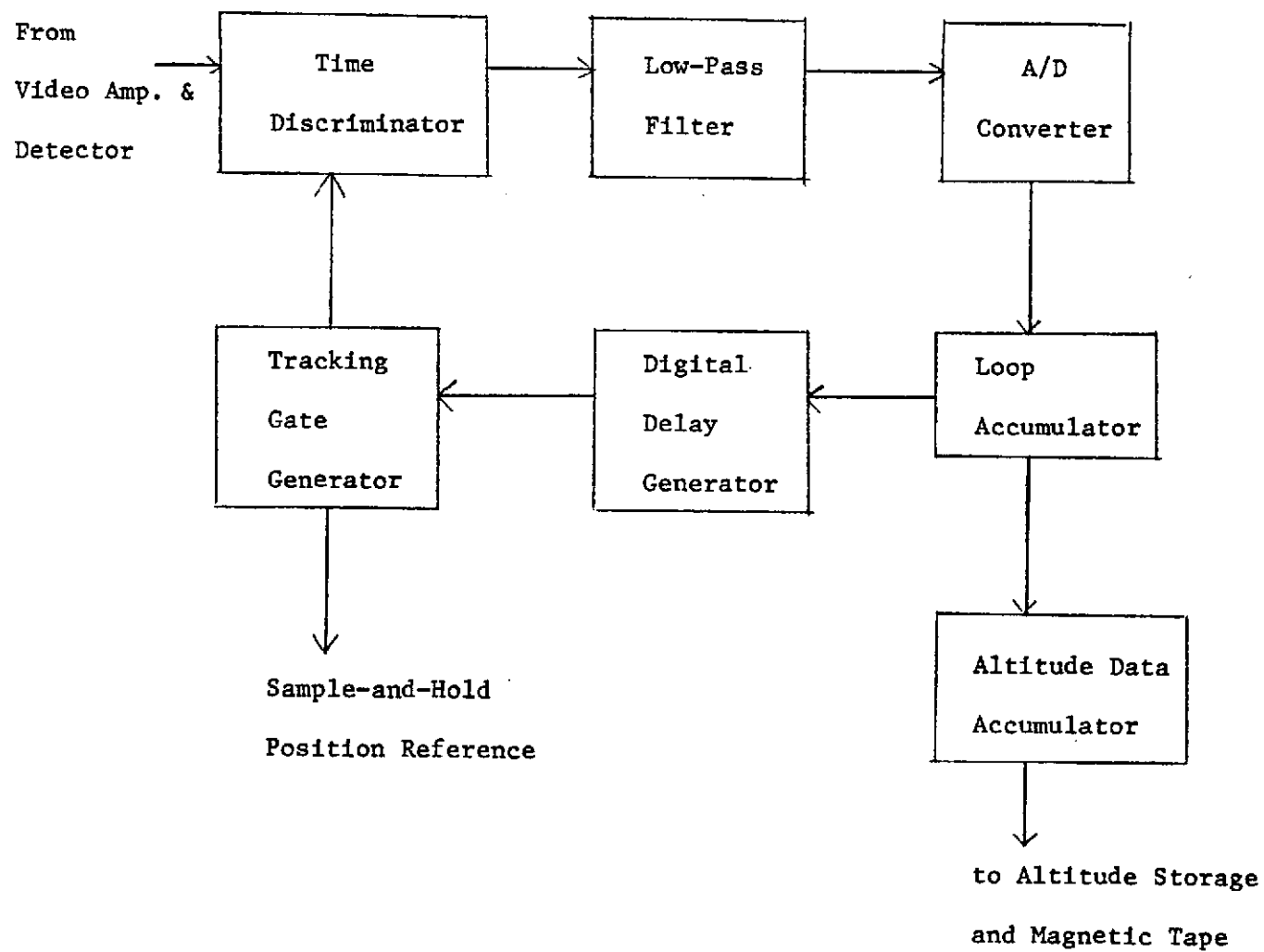
Figure 3. Block Diagram of S-193 Altitude Tracker.

TABLE 1

Comparison of Altitude Tracker Error Estimates

Source	SNR	σ_t
Equation 1	10 db	21.5 ns
Equation 1	20 db	18.0 ns
GE tracking loop simulation	>20 db	17.4 ns
S-193 hardware	>20 db	13.4 ns

The theoretical value and tracking loop simulation results in Table 1 are seen to be in good agreement. There is considerable disparity, however, between these two values and the hardware measurement. The initial reaction to this comparison might be to suspect the hardware measurement process (e.g., the sea state simulator), since the measured values are seen to be less than the theoretical estimates. However, the possibility of modeling deficiencies in the other results should not be discounted. The tracking loop simulation represents a digital simulation of the tracking circuitry only. In the absence of better information, the more conservative value shown in Table 1 will be used in subsequent discussions.

A somewhat smaller data base is presently available for use in estimating tracking jitter for 10 ns operation. Preliminary measurements by General Electric, Utica, New York, show the standard deviation of the tracker to be approximately 5 ns for 10 ns operation compared to the 13.4 ns standard deviation for 100 ns pulses (both for an SNR $\sim$ 20 db). Computer simulations of the two subsystems in Figure 4 have been conducted during this study, utilizing the fact that the video bandwidth and tracker gate widths remain at 5 MHz and 100 ns for the S-193 operating with either a 10 or 100 ns pulse length. The results show that altitude error is reduced by a factor of 3 for the 10 ns case compared to the 100 ns case, for an identical tracker and video amplifier in both instances. The theoretical improvement for a 10 ns system with a 50 MHz video amplifier and

Sea-scattered

100 ns

pulses

$f_c \pm 5$ MHz

5 MHz

100 ns gates

IF Amplifier ⊗ → Detector → Video Amp → Split gate tracker

L.O.

(A)   100 ns System

Sea-scattered

10 ns

pulses

$f_c \pm 50$ MHz

5 MHz

100 ns gates

IF Amplifier → Detector → Video Amp → Split gate tracker

L.O.
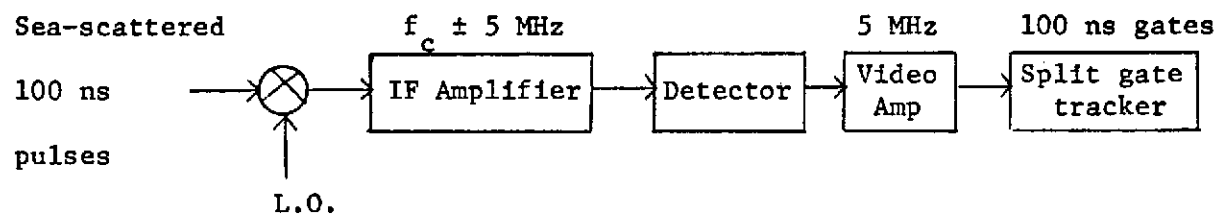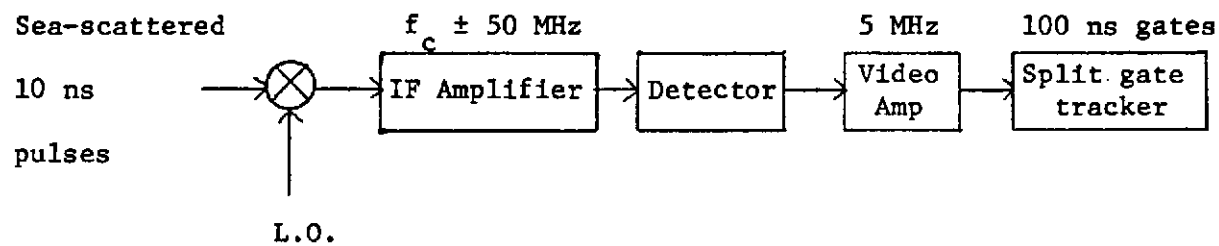
(B)   10 ns System

Figure 4. System parameters utilized in comparison of 10 and 100 ns altimeter variance.

10 ns tracking gates would be 10 to 1 (if SNR changes are ignored or for SNR $\geq$ 20 db). The 3:1 improvement in tracking jitter for the 10 ns case is obviously due to the much wider predetection bandwidth and transmitted pulse spectrum.

Before leaving this subject, note that the above data suggest the possibility that appreciable improvement in altimeter performance may be obtainable with IF and video amplifier characteristics selected on bases other than the usual radar rule of thumb (inverse pulse length relationship). It should also be noted that the improvement in tracking error for the S-193 10 ns case is not within the scope of present closed-form results. The principal limitations of these formulations arise from the approximate expressions used to represent bandwidth characteristics, particularly the IF amplifier, because of the mathematical intractability of complete system pole-zero descriptions. Histogram results to be shown in a later section of this report demonstrate the extent to which filtering operations affect altitude tracking error. For these reasons it is felt that the hardware measurements and system simulation results are more reliable than existing closed-form altimeter error estimates.

Based on the above discussed data, in the remainder of this report the sample-and-hold position jitter for 10 ns waveforms will be assumed to possess a standard deviation of 5 ns for the pulse compression case and 7 ns for the noncompressed case which will operate at lower SNR values. The tracking jitter will be assumed symmetrically distributed about mean-value. Granularity of the sample-and-hold positions is 5 ns since the digital delay generator is limited to delay increments of 5 ns [2]. It is fortunate that the sample-and-hold circuits are continuously positioned by the tracking gate circuits and not fixed during the experiment period, because of the sparse sampling pattern that exists in the S-193 hardware. Otherwise the sample rate would be equal to the sample-and-hold spacing of 10 ns, which would seriously degrade waveform reconstruction.

The next factor to be considered is the configuration of the eight sample-and-hold (S & H) operations relative to the expected position of the ramp portion of the returned signal. For a 10 ns waveform measurement only DAS 2 and DAS 3 of mode 5 are available. The expected position of the tracking gates, the mean

waveform, and the sample and hold array is shown in Figure 5. If finite antenna beamwidth effects on tracker bias in the 10 ns pulse length are taken into consideration, the gate positions will shift in the direction of early timing. Based upon available data concerning split gate tracker basis, the mean tracking position is estimated to shift approximately 25 ns, primarily because of the weights used in the split gate tracker. This location is shown as the dotted curve in Figure 5. On this basis, the ramp portion of the 10 ns measurements will contain an average of one sample position. That is, the shifted waveform shown in Figure 5 indicates that the position of the leading edge of the return pulses will occur at the break point between the first and second sample array position. This location is undesirable from the standpoint of sea-state or waveform measurements since sample-and-hold values recorded from the next position of the sampling array are not commensurate (oceanographic conditions cannot be assumed constant over the needed time period). For sea-state measurements, a figure of 10 seconds will be used in this report as a maximum period in which ocean surface homogeneity can be assumed. This represents a footprint expanse of approximately 50 kilometers.

Overall characteristics of the sampling operations available in the S-193 hardware which have been covered to this point are summarized in Table II.

TABLE II

S-193 Sampling Parameters for 10 Nanosecond Operation

RMS Position Jitter	$\sim$5 ns
Sample-and-Hold Spacing	10 ns
Position Granularity	5 ns
Sample Type	10 ns gate length with 5 ns RC time constant
Waveforms Sampled per Second	100
Approximate Number of Times per Second a 5 ns Locations is Sampled	50
Tracker Loop Bandwidth	2 Hz at 3 db 1.3 Hz Crossover 3.2 Hz Noise Bandwidth

Noise Gate   Early Gate Late Gate

position 1   2   3   4   5   6
references

10ns return ———————→ 100ns mean return
shifted by probable
tracker bias
(25ns) ——————————— 10ns return

Mode V
DAS-3
4 sample array
positions

8 S&H values/array

4 array positions

50 return samples/frame = 48 samples/sec.

250 returns/sec. → 62.5 tracker updates/sec.

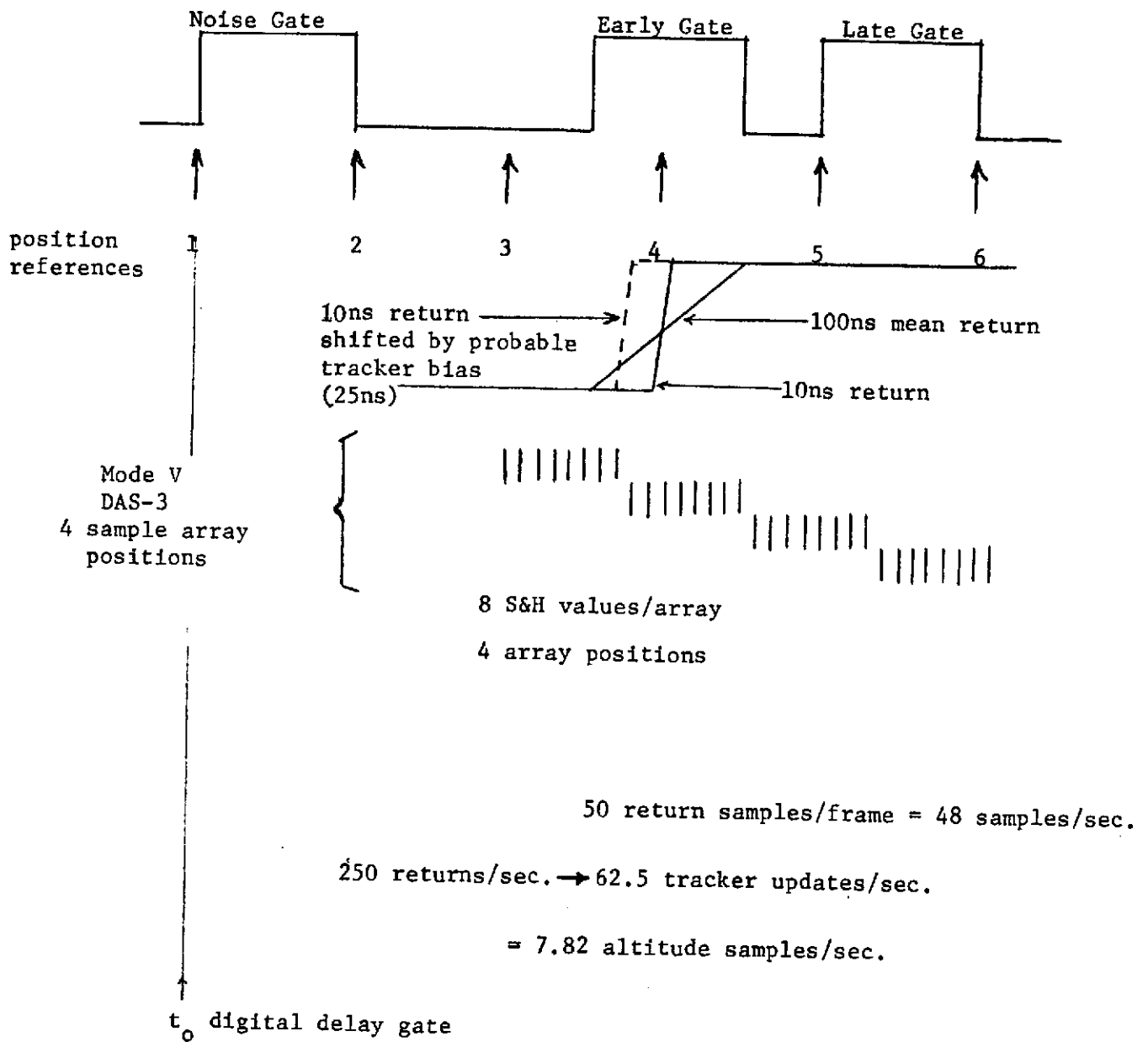= 7.82 altitude samples/sec.

t_o digital delay gate

Figure 5. Estimate of sample-and-hold positions relative to mean waveforms

2-10

As the final topic of this section, we consider the degree to which sample and hold positions can be ascertained in post flight data, and the effectiveness with which the sampling procedure on S-193 describes the altitude tracker excursions. Since the waveform sample values are subject to positional jitter identical to the altitude tracker, ground processing for waveform reconstruction must rely on sample location information derived from the ~8/sec. altitude samples available in the post-flight data. Figure 6   provides a graphical illustration of this problem; these data show that the tracking loop excursions between sampling events can be quite significant and that some form of tracking error reconstruction is certainly desirable in the 100 ns modes.

Referring to the altitude tracker block diagrams previously shown (Figure 3); the tracker must, in general, be regarded as nonlinear because of quantization characteristics of the digital delay generation (DDG). For operation with 100 ns pulse lengths, we found the altitude process standard deviation to be approximately three times larger than the step-size of the DDG, and to first-order may be represented by a linearized model. For operation with 10 ns pulse lengths the tracking jitter was found to be essentially equal to the DDG granularity (5 ns). For this case the tracker non-linearity cannot be neglected: it may in fact behave essentially as a Bang-Bang control system [3].

We may estimate characteristics of the tracking error data available in the 100 ns case as follows. The closed loop response of the altitude tracker is taken to be [2]

$$H_F(\omega) = \frac{70 \ j\omega + 280}{8 \ \omega^2 + 71 \ j\omega + 280}$$

and arithmetic averaging effects of the altitude accumulators is represented as a time-domain rectangular impulse response (or moving window) which has the transfer function
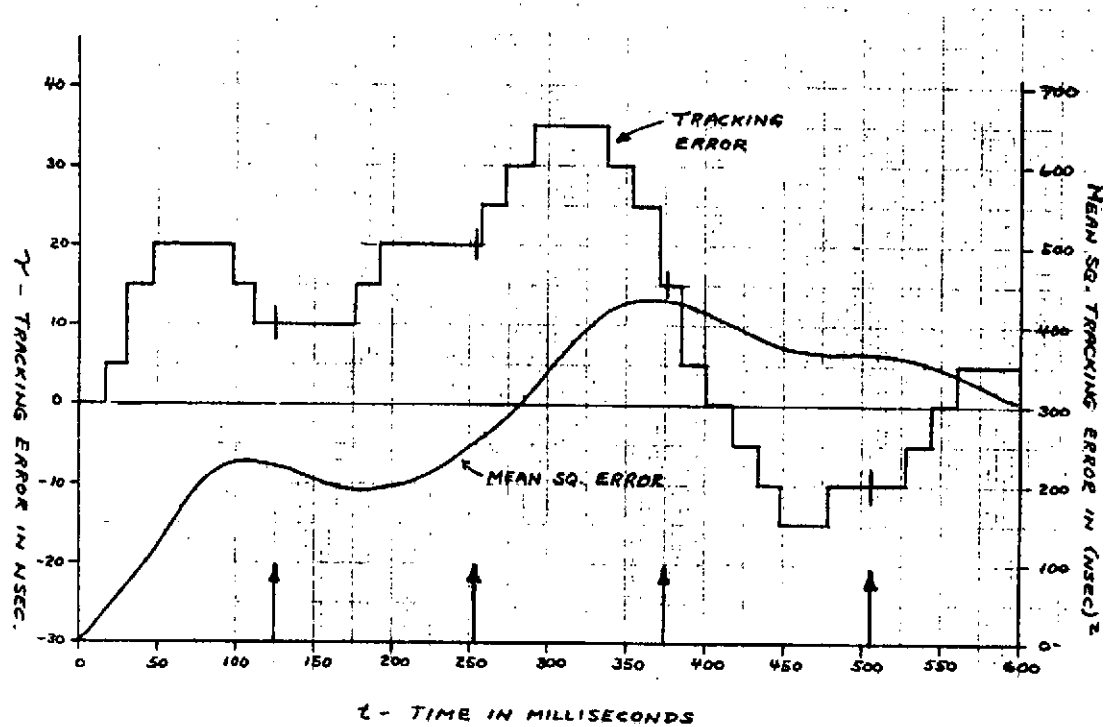
Sample result for simulation of the 100 ns case, tracking error from [2].

Typical sampling events are shown as arrows on the abcissa.

(1.3 Hz loop crossover frequency).

Figure 6. Examples of S-193 Altitude Tracking Error

$$H_A(\omega) = \frac{\sin (\omega\tau/2)}{\omega\tau/2}$$

where $\tau = 128$ ms. Figure 7 shows magnitude graphs of these transfer functions and fold-over effects resulting from the sampling operation. Note that whereas it is desired to reconstruct the behavior of the altitude tracker, only the filtered replica is available. Also, the ~8Hz sampling rate is seen to be of questionable adequacy for the tracking filter bandwidth present. As discussed in Ref. [4], an upper bound on the aliasing error may be taken to be twice the spectral area above the Nyquist frequency of the sampler. On this basis we calculate the aliasing errors to be >50 percent.

In summary, engineering considerations indicate that sample-and-hold position data may not be derivable between sampling events from post flight data in the 100 ns case. That is, the ~15 ns rms position jitter may not be reducible by post flight methods. For the 10 ns case, the system is strongly nonlinear and analytical methods of nonlinear control systems [3] appear most unpromising. We intuitively feel that the 10 ns data can be reconstructed to significantly better precision than the 100 ns data. However, this topic is largely an open problem and the most fruitful approach to its resolution is considered to be measurement of actual system statistics. The system measurements recommended comprise Monte Carlo simulations (using the S-193 engineering breadboard) of the variance of the difference between the altitude data output and the sample-and-hold positional information.
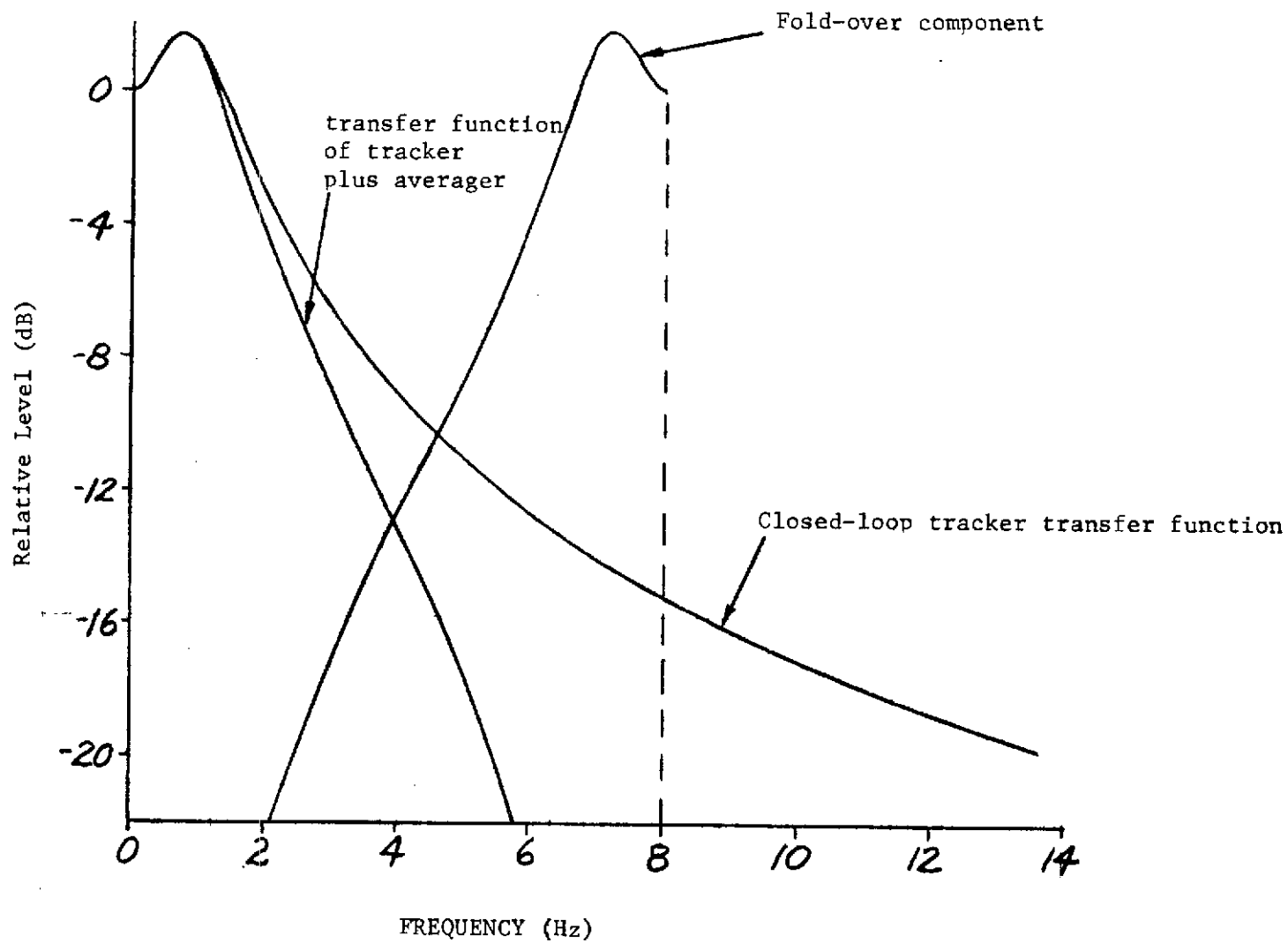
Figure 7.   Bandpass Characteristics of Altitude Data
(for B_1 = 2Hz)

2.2 WAVEFORM RECONSTRUCTION

The factors to be considered in this section are:

(1) characteristics of the zero sea-state system response up to
and including the sample-and-hold operation,

(2) waveform reconstruction considerations and detail contained
in the reconstructed waveforms, and

(3) sensitivity and limitations of reconstructed waveforms in
regard to sea-state measurement considerations.

Figure 8 is a block diagram of the altimeter characteristics to be
initially investigated in this section. The immediate discussion will be
concerned with power spectral density (PSD) characteristics of the altimeter
signal and the sampling operations in order to permit specification of re-
construction filter requirements. The PSD computations are based on a time-
invariant power spectrum, such as approximately exists in the plateau region
of the 10 ns altimeter waveforms. Referring to Figure 8, the spectrum of the
zero sea-state altimeter signal is taken to be the transmitted pulse spectrum;
and it is assumed that the linear scattering process will randomize phase of
the returned signal but will not alter the transmitted spectral shape (this
is discussed in detail in section 2.3). The power spectral density function
of the back-scattered signal $\Phi_s(\omega)$ is assummed to be of the form

$$\Phi_s(\omega) = \frac{\sin^2\left[\frac{T}{2}(\omega-\omega_o)\right]}{\left[\frac{T}{2}(\omega-\omega_o)\right]^2}$$

where ω_o is center frequency and T is pulse length. This power spectral
density function will then be shaped by the transfer function of the IF
amplifier which will be described as a three-pole maximally-flat filter
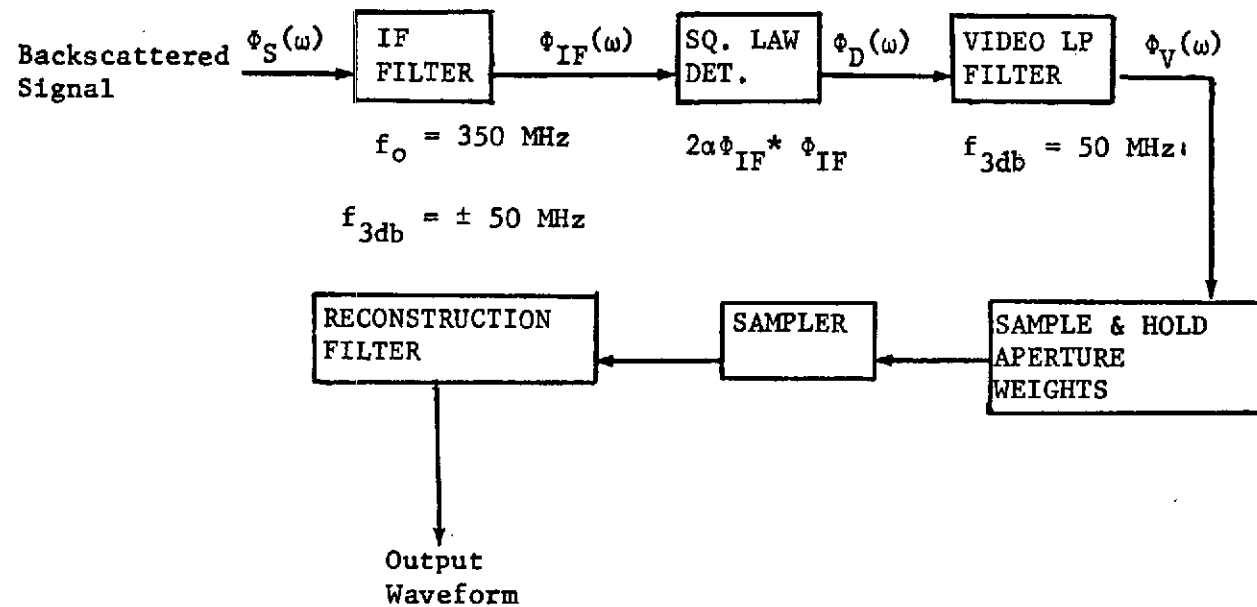whose magnitude function is

Figure 8. System components pertaining to the reconstruction problem.

$$|H_{IF}(\omega)|^2 = \frac{1}{1 + \left(\dfrac{\omega - \omega_o}{\omega_3}\right)^6}$$

where ω_3 is the 3 dB radian bandwidth. The spectral density at the output of the detector $\Phi_D(\omega)$ may be found from the convolution [5]

$$\Phi_D(\omega) = 2\alpha \left\{ \Phi_{IF}(\omega) * \Phi_{IF}(\omega) \right\} \; ; \quad \Phi_{IF}(\omega) = \Phi_S(\omega)|H_{IF}(\omega)|^2$$

which for purposes of numerical evaluation is expressed as

$$\Phi_D(\omega) = 2\alpha^2 \int_{-\infty}^{\infty} \left\{ \frac{\sin^2(\frac{T}{2}n)}{(\frac{T}{2}n)^2} \right\} \left\{ \frac{\sin^2 \frac{T}{2}(\omega - n)}{\left[\frac{T}{2}(\omega - n)\right]^2} \right\} \left\{ \frac{1}{1 + (\frac{n}{\omega_3})^6} \right\}$$

$$\cdot \left\{ \frac{1}{1 + \left(\dfrac{\omega - n}{\omega_3}\right)^6} \right\} \, dn + \alpha^2 \sigma^4 \delta(\omega) \; .$$

And finally, effects of the video filter are taken into account through use of a 2-pole maximally-flat expression

$$\Phi_V(\omega) = 2\alpha|H_V(\omega)|^2 \left\{ \Phi_{IF}(\omega) * \Phi_{IF}(\omega) \right\}$$

where

$$|H_V(\omega)|^2 = \frac{1}{1 + (\dfrac{\omega}{\omega_3'})^4}$$

in which ω_3' is 3 dB radian bandwidth of the video filter.

The results of these computations, given in Figure 9, show that the detection operation considerably broadens the one-sided IF spectrum. However, the video filter operation results in a composite spectrum that is similar to the shape of the IF spectrum. This analysis will next be extended to include averaging properties of the sample-and-hold operation.
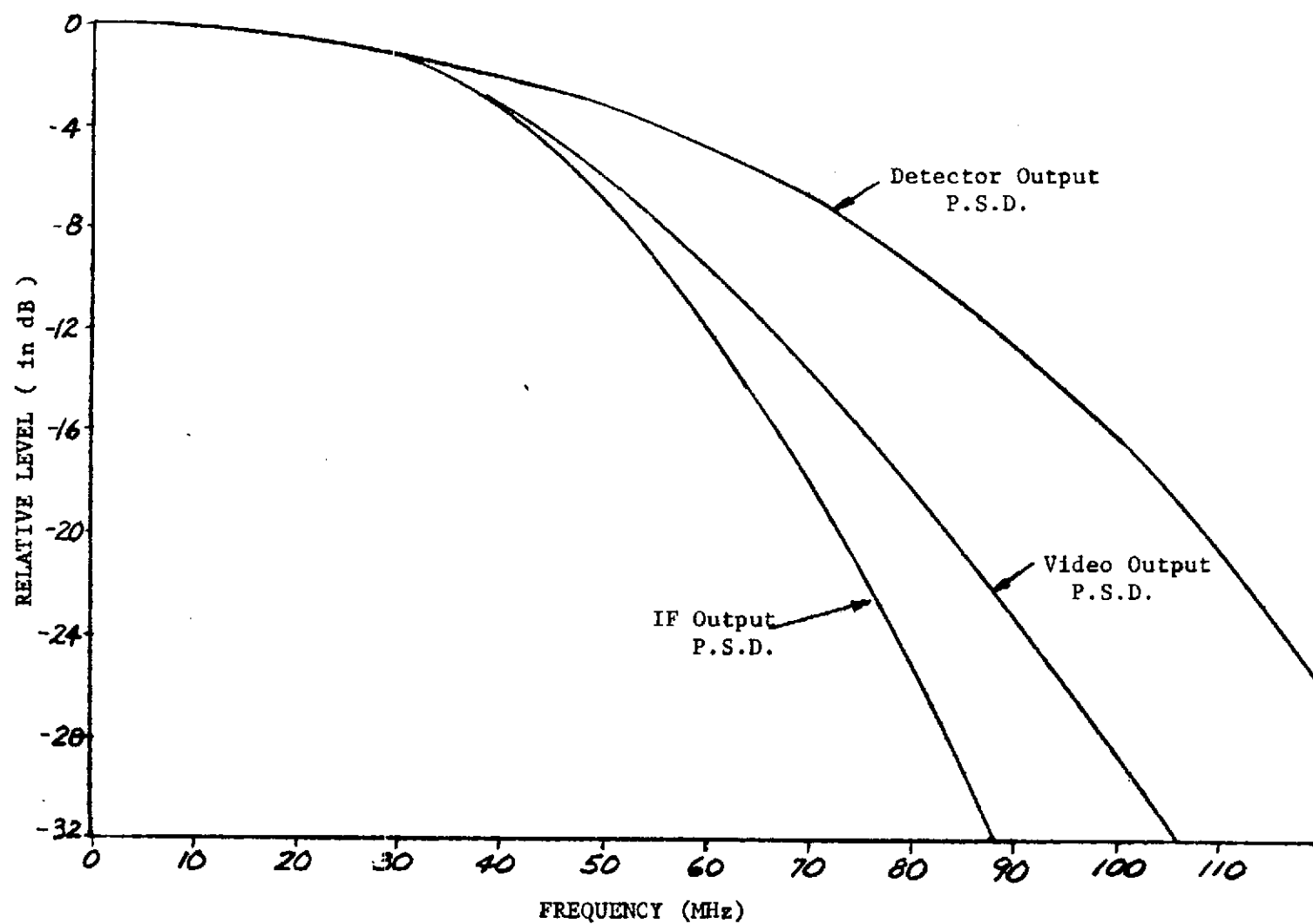
Figure 9. Computed spectral characteristics of the IF amplifier, detector and video functions

The averaging properties of the sample-and-hold operation derive from the five nanosecond RC time constant and the 10 ns gate period contained in the sampling operations [2]. As shown in Appendix A, this effect is representable as a single pole filter with a corner frequency of 50 MHz.

Figure 10 shows the composite spectrum which results from passing the video signal through the sample-and-hold averaging operation and then through a sampler function. The effect of the sampling operation is to cause the spectrum to be repetitive at 100 MHz intervals. Figure 10 also shows the extent to which the video signal is aliased. Variance of the aliased (or folded-over) component can be obtained as in the previous section by integrating the sampler power spectral density (Figure 10) over the bandpass of the reconstruction filter, for both the fundamental and aliasing component. Variance of the aliasing component has been found to be approximately four percent of the signal variance. A surprising result in this figure is that the 3 dB bandwidth of the composite system function occurs at approximately 30 MHz. The averaging operation contained in the sample-and-hold circuit is therefore seen to be an important factor in overall system response. As shown in Appendix A, the composite response of the IF, video, and sampler weights is represented to good approximation by the equation

$$|H(\omega)|^2 \doteq \frac{1}{\left[1 + \left(\dfrac{\omega}{\omega_{50}}\right)\right]^2 \left[1 + \left(\dfrac{\omega}{\omega_{50}}\right)^4\right]}$$

where ω_{50} refers to breakpoints at 50 MHz. This result will be useful in a later section.

The analysis has now reached the stage of waveform reconstruction. Previous paragraphs have shown that standard deviation of the sample-and-hold positions will be fixed by the split tracker error signal. Position granularity
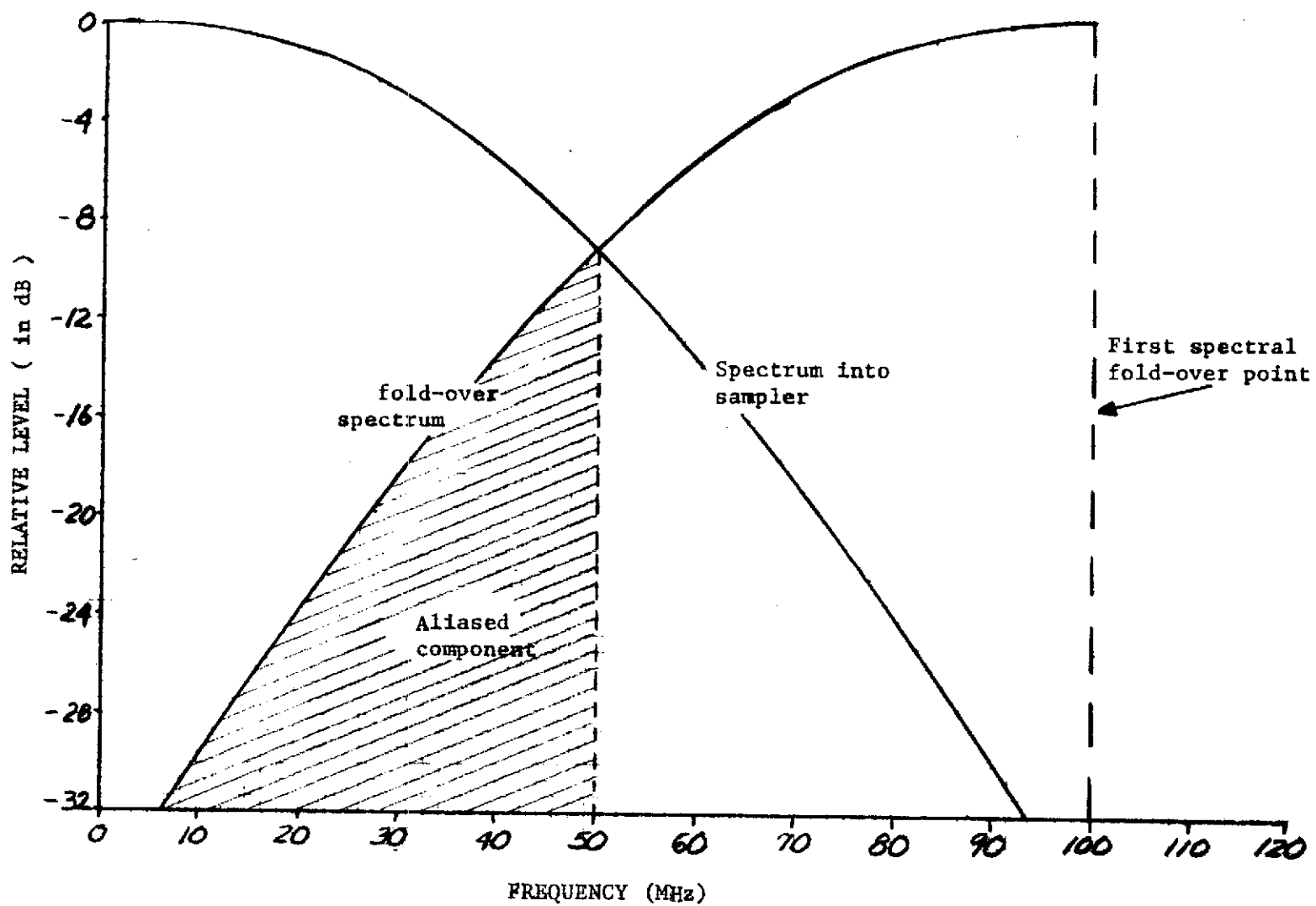
Figure 10.   Spectral characteristics of the sampled waveforms

is known to be 5 ns. Thus a single waveform will be sampled at spacings of 10 ns and position jitter will result in composite waveform samples occurring at 5 ns increments. Without specific data on the position jitter distribution, it is assumed that the 0 and 5 ns displacements will be equiprobable. Therefore the central portion of the waveform being sampled will be subjected to 100 sample-and-hold array operations per second or approximately 50 samples/ second spaced 5 ns apart.

For purposes of this analysis, a digital reconstruction filter has been implemented which consists of a (sin x)/x impulse response over the time expanse of the sample operations. The reconstruction filter and related considerations are given in section 2.3.

In reconstruction simulation, the individual random waveforms are first sampled by an array of 8 sample-and-hold operations. Each sample consists of an exponentially weighted value over a 10 ns window, as does the S-193 sampler. Figure 11 is an oscilloscope photograph of the digitally generated sample pattern; this presentation was obtained by sampling the deterministic waveform shown as the solid trace. In the reconstructed waveforms to be shown subsequently, the samples were obtained using the sample positions shown in Figure 11 with alternate sample locations displaced the scaled equivalent of $\pm$ 5 ns, to simulate positioning jitter in the S-193 system. Figure 12 shows the rise-time characteristics of the truncated exponential filter as the locus of the maxima of the sampling events. The solid trace is the input to the sampler. Sample rate in Figure 12 is much higher than the hardware rate to show waveform detail.

Figure 13 shows a rather interesting effect of the (sin x)/x reconstruction process. Referring to this figure, photograph (A) shows the reconstructed waveform based on 16 samples spaced by 5 ns, or for a ramp waveform defined over 80 ns (including gate time) and, in effect, assumed to be zero outside the data region. The (sin x)/x filter exactly reconstructs the waveform at the sample points (every 5 ns), but the artificial truncation caused by the finite sample values causes a distortion akin to the Gibbs phenomenon of Fourier transform theory. In photograph (B) the data span has
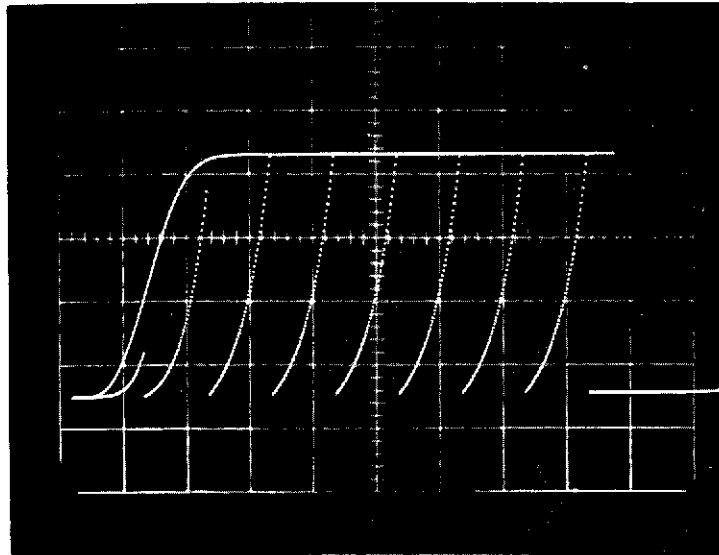
Figure 11. Photograph of exponentially weighted sample pattern
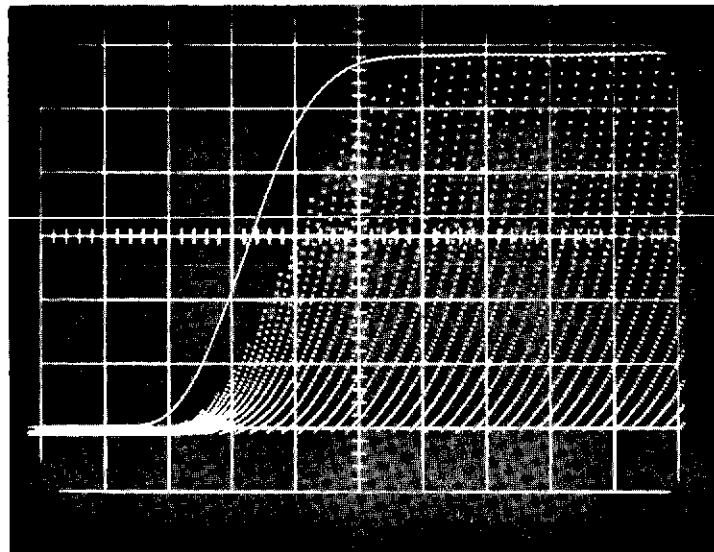(simulated sweep-rate 10 ns/cm)

Figure 12. Rise-time characteristics of the exponentially weighted
sampler

A

C

B

D
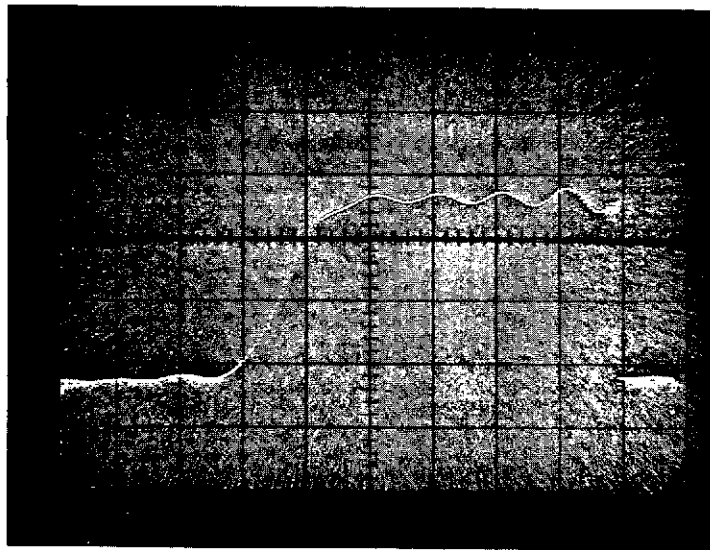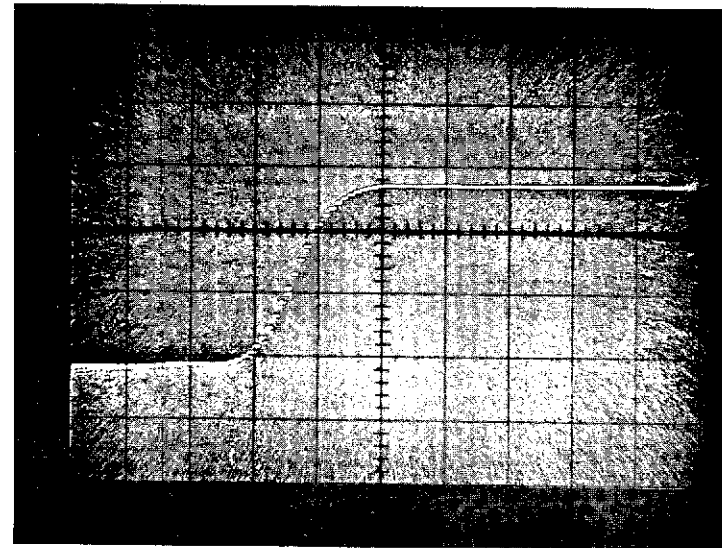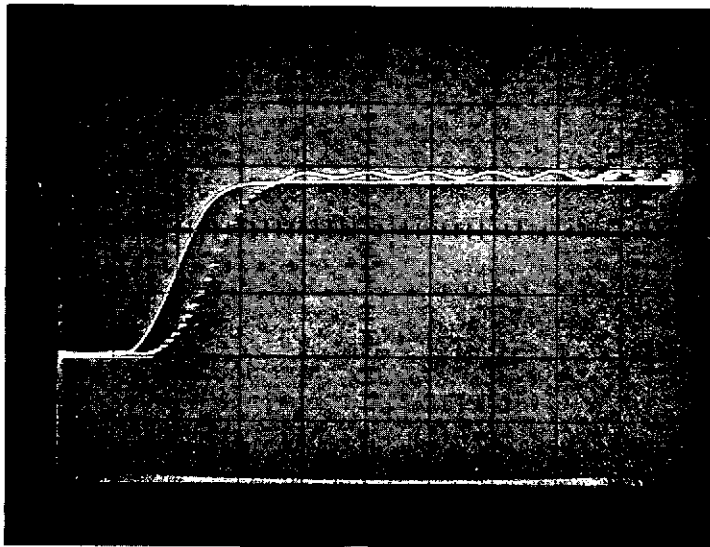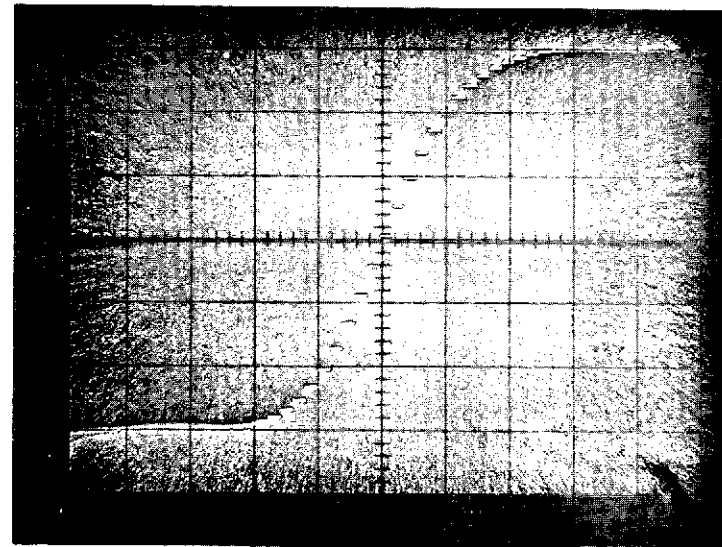
Figure 13. Reconstruction filter characteristics

been extended by extrapolating the plateau values out an additional 12 sample values.* In other words, 32 samples (over 160 ns) were used with the first and last two or three samples taken as zero. Photograph (B) shows the reconstructed waveform (the discontinuous trace) to still contain ripples due to the waveform truncation discontinuity. In photograph (C) a reconstruction algorithm is used which does not contain a waveform discontinuity; two values before the arrival of the waveform are taken, the waveform is sampled for 60 ns, and these same values are then reflected over the next 80 ns. This results in a symmetrically extrapolated waveform as an input to the reconstruction filter, which is free of discontinuities. This technique is found to be a considerable improvement over the first two results. Photograph (D) is a reproduction of the data shown in (C) using a higher sweep rate (5 ns/cm).

Sea-state resolution achievable with the Skylab altimeter has been studied using the computation techniques shown in Figure 14. Two classes of computations are used: Monte Carlo simulations of the waveform fluctuation statistics for different SNR values, and deterministic computation of the waveform effects due to ocean surface roughness. These two will be described in turn, and their results used to estimate the number of waveform samples needed for a given sea-state resolution.

The fluctuation statistics were studied by using a 100-bin histogramming program to examine the waveform at a single point in the plateau region; the histograms obtained are of the video waveform and since the reconstruction process reproduces exactly the sampled values, the histograms consequently include all system behavior up to and including the reconstruction. Results for a series of 5000-sample, 100-bin histograms are given in Table III below, for specified simulated bandwidths.

---

*Photograph (B) also shows the ramp signal prior to sampling (solid trace).

SEA-STATE SIMULATION PROCEDURE

MONTE CARLO

Analog $\longleftarrow$————Digital————————————$\longrightarrow$

```
┌──────────┐        ┌─────────┐      ┌──────────────┐
│Flat-Sea  │        │weight   │      │    Sin x     │      Population
│Waveforms │   ↑    │   &     │      │  ─────────   │  →   Histograms
│5K sample │───┘    │sample   │  →   │     x        │──┘
│cases     │        └─────────┘      │Reconstruction│
└──────────┘                         └──────────────┘
```

└————Noise; 10, 20, ∞ SNR

DETERMINISTIC

Analog   Digital   Analog

```
┌──────────┐        ┌───────────┐      ┌────────────┐
│"Mean" flat│       │   A/D     │      │  Gaussian  │
│sea video │        │  Digital  │      │ sea-state  │
│waveform  │   →    │  Storage  │  →   │convolution │───→TAPE
│          │        │    &      │      │            │
└──────────┘        │ slow time │      └────────────┘
                    │   D/A     │
                    └───────────┘
                                                            │
                                                            ↓
                                              ┌────────────────┐
                                              │      D/A       │
                                              │ Reconstruction │
                                              │  and display   │
                                              └────────────────┘

                                                  Digital
```
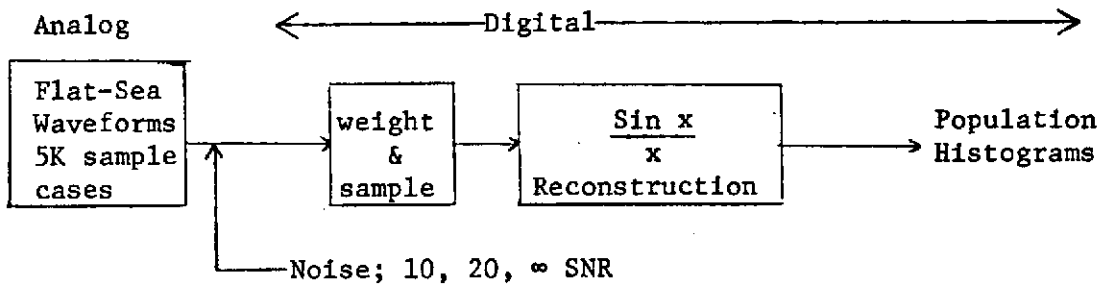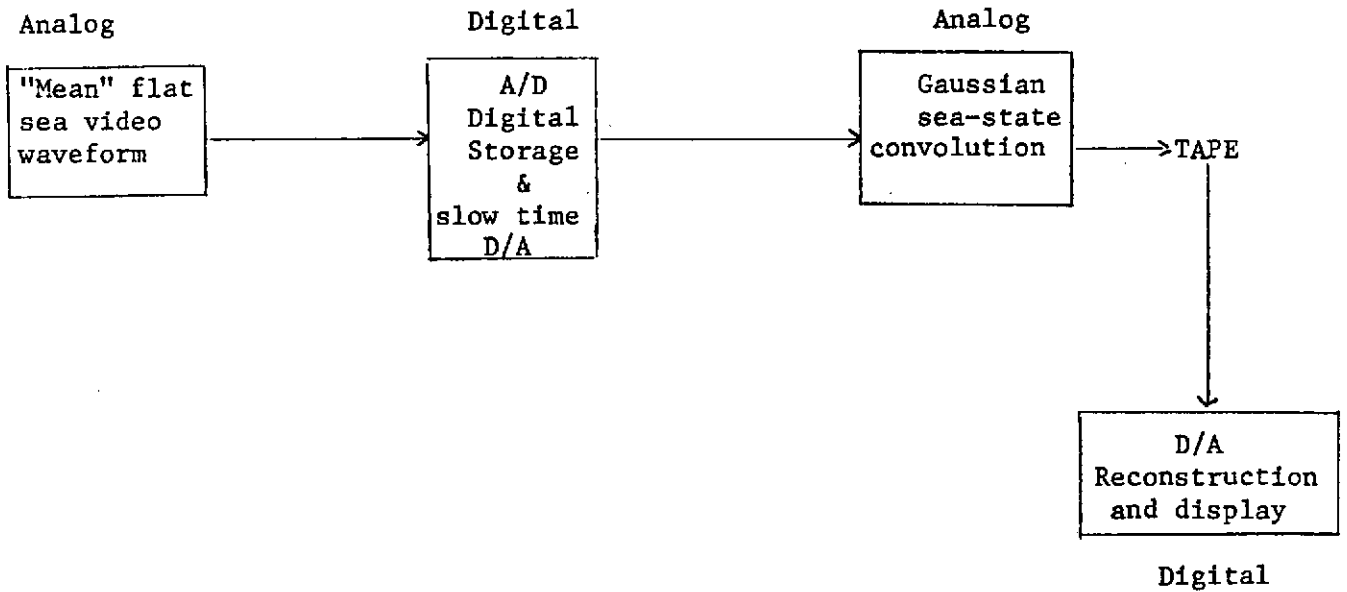
Figure 14. Sea-State Simulation Procedure.

Table III. 5000-sample histogram results for sampled data in the plateau region of simulated radar return waveforms for 10 ns pulse.

IF bandwidth	Video bandwidth	SNR	Sample type	Population standard deviation ÷ mean signal
±50 MHz	50 MHz	10db	10 nansec. sample-and-hold, 5 nanosec. RC time constant	.469
±50	50	20	10 nanosec. sample-and-hold, 5 nanosec. RC time constant	.439
±50	50	∞	10 nanosec. sample-and-hold, 5 nanosec. RC time constant	.433
±50	50	∞	single point sample	.549
±100	50	∞	single point sample	.479
±50	12.5	∞	single point sample	.497

Plotting histogram results vs. the midpoint of each bin produces an estimate of the unnormalized probability density function for the parent population. By appropriately scaling the horizontal (sampled voltage level) axis we set the mean value to unity; then adjusting the vertical axis (frequency of occurrence) so that the area under the curve is unity, we obtain the normalized probability density function. Cumulative area under the curve then gives the probability distribution function, and Figure 15 displays both the density and distribution functions so obtained for the third and fourth entries in Table III.

Obviously, the processes are non-Gaussian. However, the quantity of direct interest is the mean of a number n, of independent waveform samples and the central limit theorem guarantees that the distribution of these

A) Single-point sample, noise-free case

B) 10 nanosecond simulated sample-and-hold, noise-free case
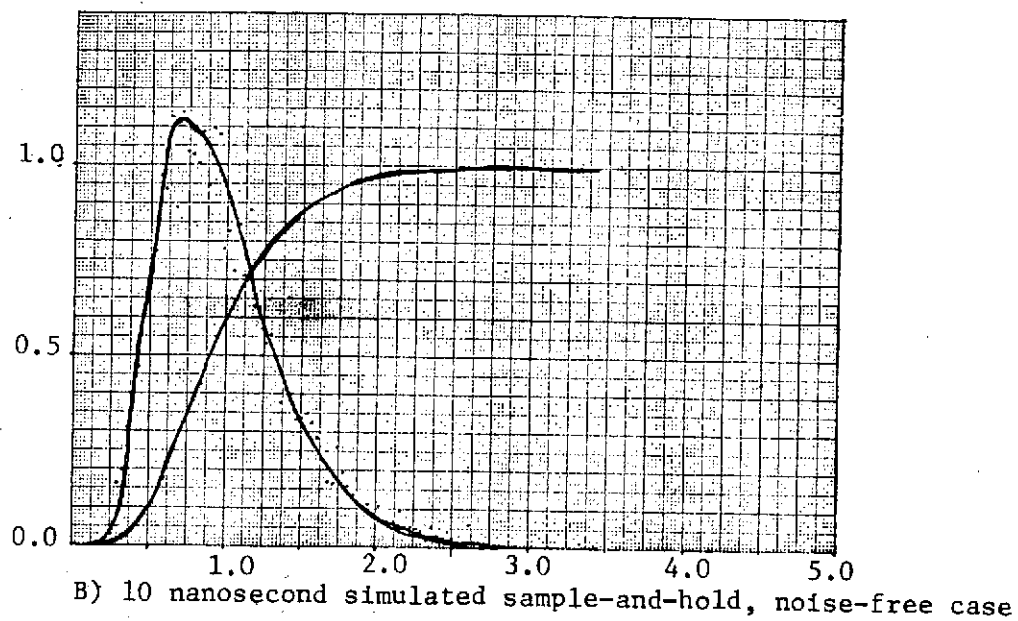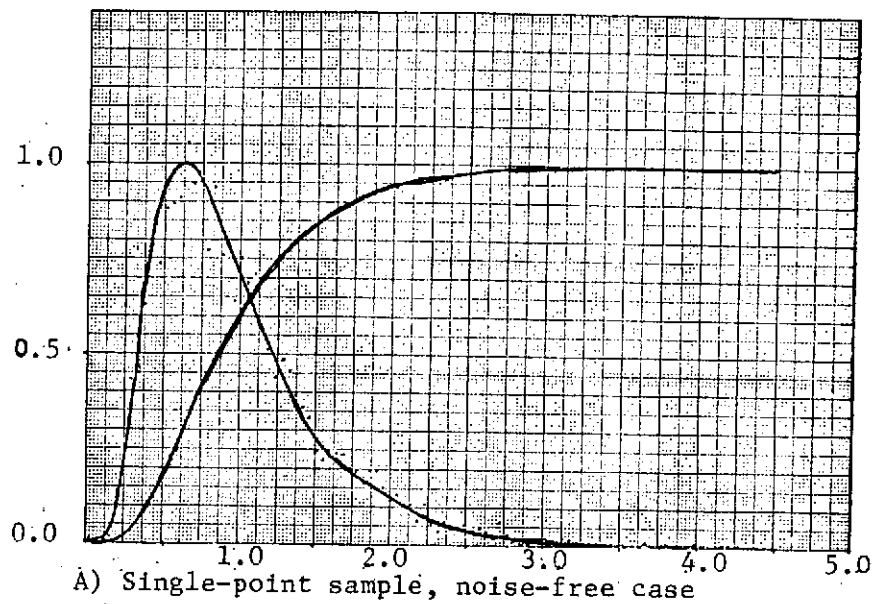
Figure 15. Probability density and distribution functions
as derived from 100-bin histograms of 5000 waveforms
sampled in the plateau. The results have been
rescaled so that the mean is 1.00.

means will be very closely Gaussian, with a standard deviation obtained by dividing the last column in Table III by $\sqrt{n}$. For the resolution example to be presented below, the 10 db SNR, 10 nanosecond gate result will be used, for which the ratio [(standard deviation of mean) ÷ mean] is $0.469\sqrt{n}$.

For the deterministic computation of sea-state effects on waveforms, the effective radar-sensed surface height distribution $p(z)$ is assumed to be Gaussian. The mean flat-sea video waveform is sampled at equivalent 5 nanosecond intervals by 10 nanosecond wide sample-and-hold gates having a 5 nanosecond RC time constant, and these sample values are processed through the reconstruction filter. The filter output (a series of steps from the D/A converter on the digital computer) is convolved with the Gaussian (at the analog computer) to obtain an estimated reconstructed rough-sea waveform for comparison with the flat-sea case. This has been done for four different rms roughnesses and the results are displayed in Figure 16. The discontinuous curves in Figure 16 are the flat-sea waveforms, identical in the four photographs and appearing different only because different arbitrary horizontal (time) scales were used in the 'scope photographs. Note that the process here described has the reconstruction and convolution operations interchanged relative to the scheme shown in Figure 14; the errors are expected to be small in this interchange and this should provide at least reasonable estimates for the assumed Gaussian $p(z)$.

Sea-state measurability is related to the vertical distances between the curves for flat-sea and rough-sea, and these distances were measured on the photographs in Figure 16 by defining a standard time T_m at a point where the vertical differences are close to maximum, T_m is defined as the point at which a straight line drawn tangent to this flat-sea curve at its half-height point reaches the maximum or plateau value. This definition requires that the flat-sea and rough-sea curves are adjusted to the same amplitude and that their half-height points coincide, as is the case in Figure 16. From vertical distance measurements on the photographs at T_m, Table IV is derived.
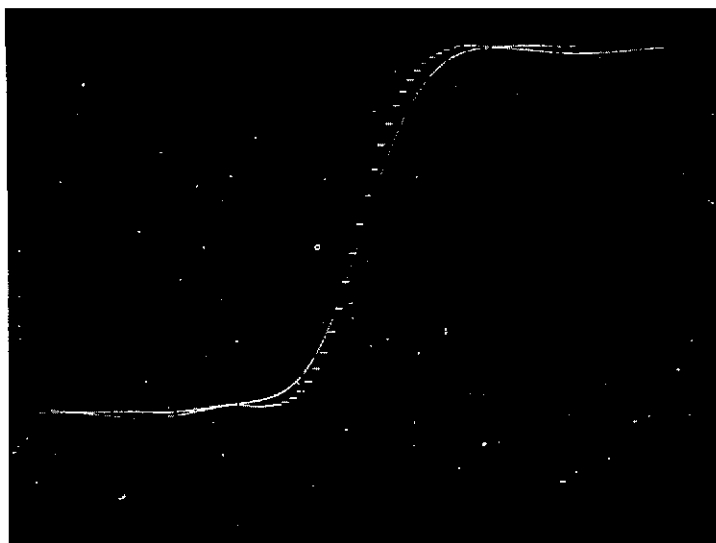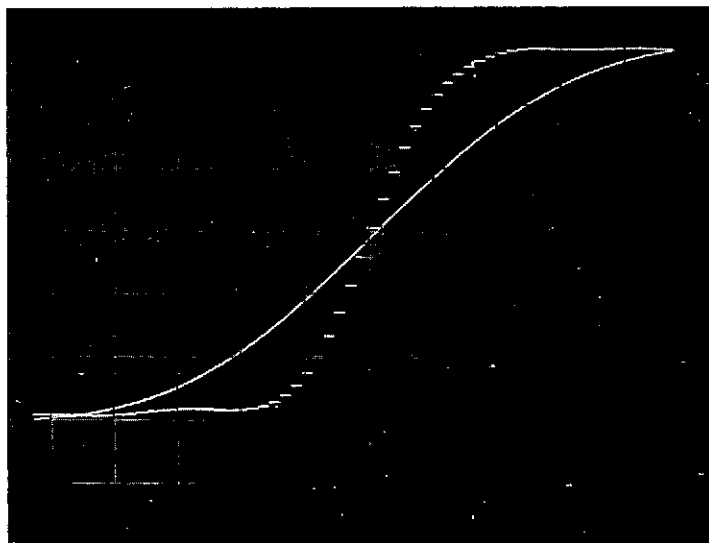
σ = 1/2 meter
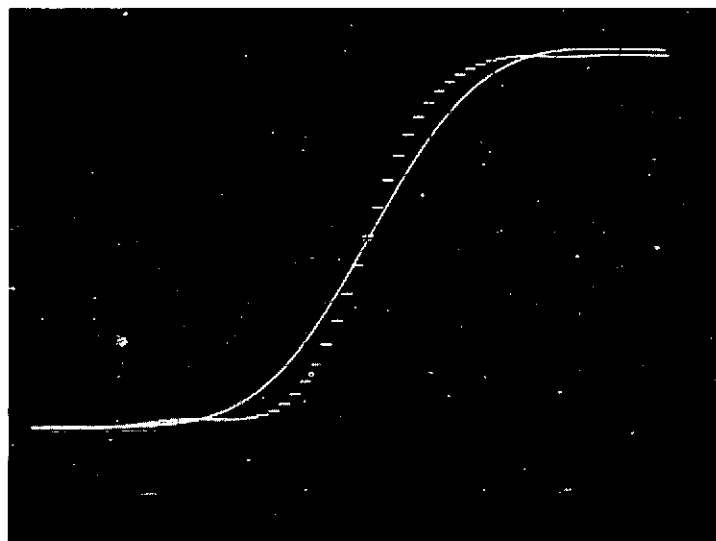
σ = 2 meters

σ = 1 meter
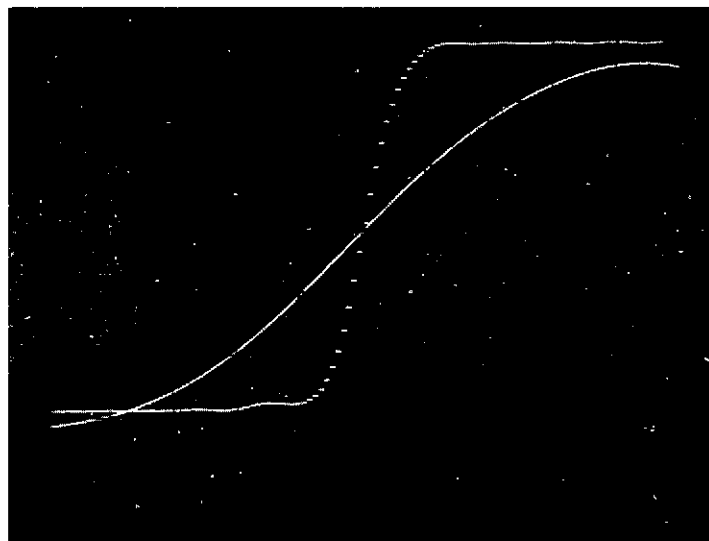
σ = 3 meters

Figure 16.   Mean Waveforms versus rms ocean roughness (σ)

Table IV. Sea-state effects on deterministic waveforms

Ocean surface roughness $H_{1/3}$ ft rms meters	$\left[\dfrac{\text{(flat sea)}-\text{(rough sea)}}{\text{(flat sea)}}\right]$; measured at T_m	Differences in second column
6.6 ft 1/2 meter	.075	
		.034
13.2 1	.109	
		.141
26.5 2	.350	
		.096
39.8 3	.346	

The third column in the table is obtained from differences in the second column entries and indicates resolution necessary to separate one sea-state range from another. For example, to distinguish between sea-state $\geq$ 2 meters and sea-state $\leq$ 1 meter, the table indicates that resolution of the reconstructed sampled wave at T_m be at least 0.141. It would be necessary that this be $2\sigma_x$; thus σ_x is about 0.07 and can be compared to the 10 db SNR result from Table III $(0.469/\sqrt{n})$ to find n, the number of independent waveform samples required. The result is that a minimum of 45 independent waveforms are required to determine whether the sea-state is $\geq$ 2 meters or is $\leq$ 1 meter. A similar exercise predicts that a minimum of $\sim$760 waveforms is required to distinguish sea-state $\leq$ 1/2 meters from sea-state $\geq$ 1 meter. An extension of this procedure will produce estimates of the number of waveforms required for any given sea-state resolution in the Skylab case, and a similar procedure should be used in specifying GEOS parameters.

2.2.1 Computational Aspects of Post-Flight Sea-State Measurement

As shown in Reference [1], ocean roughness effects on the ensemble mean detected waveform $\overline{e_o(t)}$ are representable by the equation

$$\overline{e_o(t)} = \int_{\infty}^{t} p(z) \, \overline{f}(t - z) \, dz \qquad (2)$$

where $p(z)$ is the radar waveheight distribution and $\overline{f}(\cdot)$ is the smooth-sea
mean waveform which is known from pre-launch measurements, analytical estimates
and/or orbital measurements. In the smooth-sea case $p(z) = \delta(t)$ and the system
description $f(\cdot)$ is obtained directly since $\overline{e_o}(t) = f(t)$. The system response
analysis given in section 2.2 will be used in this section to define $\overline{f}(t)$. The
system response up to the sampling operation was seen to be representable as a
linear transfer function $H(s)$ of the type

$$H(s) = \left[\left(1 + \frac{2 \, s}{\omega_{50}} + \frac{s^2}{\omega_{50}^2} \right) \left(1 + \frac{s}{\omega_{50}} \right) \right]^{-1} \qquad (3)$$

and the reconstructed "flat-sea" response was shown to be closely approximated
by the above function and a ramp excitation. Therefore the convolution equation

$$\underbrace{\overline{e_o(t)}}_{\substack{\text{observed} \\ \text{quantity}}} = \int_{-\infty}^{t} \underbrace{p(z)}_{\substack{\text{waveheight} \\ \text{distribution} \\ \text{to be determined}}} \overbrace{\overline{f(t - z)}}^{\text{known } \underline{a \ priori}} \, dz \qquad (4)$$

is recognized to be a first-order integral equation for the unknown quantity
$p(z)$. Its solvability by classical (and numerical) means is dependent on the
form of kernel $f(\cdot)$ chosen. In the case of continuous functions, it is a
Volterra equation of the first kind which may be converted to the more tractable
second kind by differentiation [6]. It can then be solved by the classical
method of successive approximation, which for an exponential kernel (which arises
from the finite-pole system description) should lead to a summable, closed-form
result. Also for an exponential kernel, it cannot be converted into a finite

order differential equation problem. In any case, the available S-193 data will be in sampled form and we expect to utilize digital computer methods; both of these factors strongly suggest the use of z-transform methods. In the remainder of this discussion, we will outline such a solution.

For computational convenience we will assume that the measured parameter $\overline{e}_o(t)$ has been normalized by pre-processing to remove the noise base line (to be discussed in Section 2.3.2). To begin, previous discussions have shown that $\overline{f}(t)$ may be approximated by a ramp input to the cascade combination of a 2-stage RC filter with a 3 dB bandwidth of 50 MHz, followed by a single stage filter (to represent the exponential sampler weights) also with a 50 MHz, 3 dB bandwidth. As such, the transform of $\overline{f}(t)$ is taken to be

$$F(s) = \left\{ \frac{1}{s_2} - \frac{e^{-Ts}}{s^2} \right\} \frac{1}{(s+a)(s+b)^2} \qquad (5)$$

in which the first term on the right in parentheses represents the ramp (of expanse T) and the remaining terms the transfer function H(s). By partial fraction methods, F(s) can be rewritten as

$$F(s) = (1 - e^{-Ts}) \left\{ \frac{A}{s} + \frac{B}{s^2} + \frac{C}{s+a} + \frac{D}{s+b} + \frac{E}{(s+b)^2} \right\}, \qquad (6)$$

in which

$$A = -\frac{(2a+b)}{a^2 b^3},$$

$$B = +\frac{1}{ab^2},$$

$$C = +\frac{1}{a^2(a-b)^2},$$

$$D = +\frac{(2a-3b)}{b^3(a-b)^2},$$

and

$$E = -\frac{1}{b^2(a-b)}.$$

This can be inverted to yield a time domain form $\overline{f}(t)$,

$$\overline{f}(t) = U(t) \ [A + Bt + C \ e^{-at} + De^{-bt} + Ete^{-bt}]$$

$$\tag{7}$$

$$- U(t-T)[A + B(t-T) + Ce^{-a(t-T)} + De^{-b(t-T)} + E(t-T)e^{-b(t-T)}]$$

where $U(\cdot)$ is the unit step.

Note that thus far we have tacitly assumed that all quantities of the integral equation are Laplace transformable. If $p(z)$ is taken as non-zero for both positive as well as negative z, we will be forced to use a much more complicated bilateral transform. Recognizing that the sampled data is accurate to about 1% (due to bit size and other factors) suggests that the time basis can be shifted to avoid bilateral transforms. To show this first write the previous equation in abbreviated form as

$$\overline{f}(t) = f_1(t) \ U(t) - f_1(t-T) \ U(t-T)$$

for which

$$\overline{e}_o(t) = \int_{-\infty}^{\infty} p(z) \ [f_1(t-z) \ U(t-z) - f_1(t-T-z) \ U(t-T-z)] \ dz \tag{8}$$

which is equivalent to

$$e_o(t) = \int_{-\infty}^{t} p(z) \ f_1(t-z) \ dz - \int_{-\infty}^{t-T} p(z) \ f_1(t-T-z) \ dz \ .$$

Therefore if $p(z)$ can be represented by a function which is truncated at some negative z, then a shifted variable z' can be used such that $p(z') = 0$ for $z' < 0$ and the integral equation written as

$$\overline{e}_o(t') = \int_{o}^{t} p(z') \ f_1(t-z') \ dz' - \int_{o}^{t'-T} p(z') \ f_1(t-T-z') \ dz' \ . \tag{9}$$

As an example, if p(z) has approximately a Gaussian shape, which for some reason cannot be characterized to better than 1 percent, then p(z) can be truncated at 3-sigma and then shifted by 3-sigma to yield a non-anticipatory impulse response form. In this sense, the mathematics can provide accuracy to an arbitrary degree by increasing the shift parameter – the accuracy constraints in our problem are inherent in the available data. In the remainder of this section we will utilize only one-sided transform theory.

Returning to Equation 8 and taking the upper and lower integration limits to be t and zero respectively, and using the transform convolution theorem and the transform pair,

$$f_1(t-\alpha) \ U(t-\alpha) \longleftrightarrow e^{-\alpha s} \ F_1(s); \ \alpha \geq 0$$

yields the result

$$E(s) = P(s) \ F_1(s) - e^{-Ts} \ P(s) \ F_1(s).$$

The solution for P(s) therefore is,

$$P(s) = \frac{E(s)}{F_1(s)(1 - e^{-Ts})} \quad .$$

This may be converted into a Z-transform equation by noting that [7],

$$Z \left\{ e^{-kT_1 s} \ F_1(s) \right\} = z^{-k} \ F_1(z)$$

thus

$$P(z) = \frac{E(z)}{F_1(z) - z^{-k} \ F_1(z)}$$

where the sampling period is T_1 and $F_1(z)$ is the Z-transform of $f_1(t)$, i.e.,

$$f_1(t) = A + Bt + C\,e^{-at} + D\,e^{-bt} + Et\,e^{-bt} \qquad \text{in the time domain}$$

$$F_1(s) = \frac{A}{s} + \frac{B}{s^2} + \frac{C}{s+a} + \frac{D}{s+b} + \frac{E}{(s+b)^2} \qquad \text{as a Laplace transform}$$

$$F_1(z) = \frac{Az}{z-1} + BT_1\,\frac{z}{(z-1)^2} + C\,\frac{z}{z-e^{-aT_1}} + D\,\frac{z}{z-e^{-bT_1}} + ET_1\,\frac{e^{-bT_1}}{(z-e^{-bT_1})^2}$$

$$\text{as a Z-transform.}$$

The solution form to be utilized in digital programming can now be seen. For a sequence of input data which describes $\overline{e}_o(t)$ with values $E_0, E_2, \ldots E_i$; the z-transform equation is

$$P(z) = \frac{E_0 + E_1 z^{-1} + E_2 z^{-2} + \ldots}{(1-z^{-k})\left[\dfrac{Az}{z-1} + \dfrac{BT_1 z}{(z-1)^2} + \dfrac{Cz}{z-e^{-aT_1}} + \dfrac{Dz}{z-e^{-bT_1}} + \dfrac{ET_1 e^{-bT_1}}{(z-e^{-bT_1})^2}\right]} \qquad (11)$$

where $k = T/T_1$ is the system pulse length or "ramp length" in multiples of the sampling interval; for computational convenience, k should be an integer. Equation 11 may be manipulated into the form

$$P(z) = \frac{\left[E_0 + E_1 z^{-1} + E_2 z^{-2} + \ldots\right]\left[1 + Jz^{-1} + Kz^{-2} + Lz^{-3} + Mz^{-4} + Nz^{-5}\right]}{\left[1-z^{-k}\right]\left[P + Qz^{-1} + Rz^{-2} + Sz^{-3} + Tz^{-4} + Vz^{-5}\right]}$$

where J, K, L, etc., are constant terms such as

$$J = -\,(2 + e^{-aT_1} + 2\,e^{bT_1}) \; .$$

Further manipulation yields

$$P(z) = \frac{E_0 + z^{-1}(JE_0+E_1) + z^{-2}(KE_0+JE_1+E_2) + z^{-3}(LE_0+KE_1+JE_2+E_3) + \ldots}{P + Qz^{-1} + Rz^{-2} + Sz^{-3} + Tz^{-4} + Vz^{-5} - Pz^{-k} - Qz^{-(KH)} - Rz^{-(K+2)} - \ldots} \cdot (12)$$

If, for example, S-193 data were reconstructed with 2.5 ns increments, a 10 ns pulse length would correspond to k = 4 in the above equation. This last equation may be used to directly obtain time domain samples by performing long division inversion since division of denominator into mumerator gives

$$F(z) = \sum_{j=o}^{m} f(j)z^{-j}$$

in which f(j) are values of the desired time domain sequence. There are, however, existing numerical methods for z-transform inversion in the literature which are very useful in digital programming (see Appendix A of Freeman [7]). Before undertaking such programming, the actual S-193 waveform data should be analyzed to determine whether or not modification of the above-used system description $\overline{f}(t)$ is in order.

2.3 Computer Simulation Description

The various Monte Carlo and deterministic computations cited herein were performed on an EAI 380 Analog/Hybrid computer and a PDP-8/e digital computer. An overall diagram of the computations is given in Figure 17.

In this system the analog computations use pulse lengths of 10 or 100 ms at a repetition rate of 3 to 4/sec., depending on the digital computation cycle time. The digital computer is capable of A/D rates of ~80 KHz; however, averaging and other internal operations limit mean waveform accumulation to about 400 sample values/sec. For the programs now in operation all altimeter computations through the post-detection filtering process are analog computations and the digital computer performs the weighting, sample-and-hold, waveform averaging, split-gate tracker and statistical computations. This

ANALOG COMPUTER   DIGITAL COMPUTER

```
┌─────────────────────────┐                    ┌─────────────────────────────┐
│ Simulation of:          │                    │ Sea-state computations      │
│                         │                    │                             │
│  1) Transmitted and     │                    │  1) Waveform averaging      │
│     sea-scattered       │                    │     & statistical compilations│
│     signal properties   │                    │  2)  Sample-and-hold        │
│  2) Altimeter IF        │                    │     operations              │
│     amplifier and       │        ┌─────┐     │  3) Waveform reconstruction │
│     detector            │    ────│ A/D │──→  │                             │
│  3) Post detector       │        └─────┘     │ Altimeter Computations      │
│     convolutions        │          ↑         │                             │
│  4) Gaussian and        │          │         │  1) Split-gate tracker      │
│     bimodal wave        │          │         │     simulation              │
│     height distri-      │   ←─────────→       │  2) Variance and histograms │
│     bution              │     ┌────────┐      │                             │
└───────↑─────────↑───────┘     │ CLOCK  │      └──────────↑──────────────────┘
        │         │             └────────┘                 │              │
```

Random Noise   Parameters –   Parameters   D/A
Generators   pulse length,   sample weighting   ↓
              receiver char.   and density,   x-y plotter,
                              reconstruction   tape recorder,
                              algorithm,   etc.
                              tracker gate
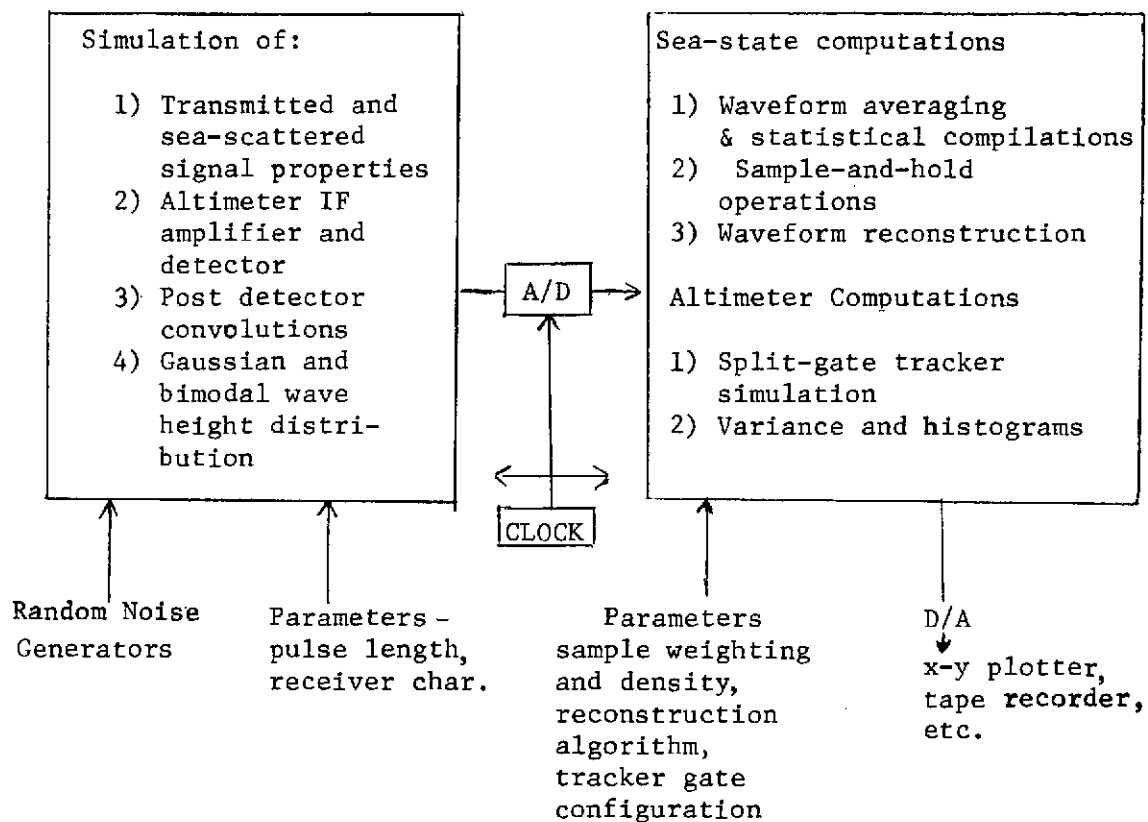   configuration

Figure 17.   Summary of Computer Functions.

type of problem breakdown appears to best utilize the salient features of both machines; it is difficult to see how a totally digital system* could compete with this hybrid arrangement, either on a computation speed, convenience of system variation, or cost basis. Details of the computer altimeter implementation are given separately for the analog and digital computers in the following two subsections.

2.3.1 Description of Analog Computation

The analog system is diagrammed in Figure 18. The major functions shown are (1) the backscattered (smooth-sea) and thermal noise simulation, and (2) the altimeter receiver simulation consisting of the IF amplifier, detector, video amplifier, and sea-state convolution. Each of these functions is detailed in the following paragraphs. The noise sources consist of General Radio type 1390-B random noise generators. Typical waveforms at different points in the system are shown in Figure 19. As would be expected, it is impossible to identify mean waveform structure in the individual ensemble members. As a point of reference, deterministically generated wave-forms are shown in Figure 20. These were obtained by replacing the random noise generator shown in Figure 18 with a CW signal at the center frequency of the IF amplifier.

2.3.2 Backscattered Signal Modeling

Simulation and/or mathematical modeling of the ocean scattered signal is the cornerstone of any altimeter system study. In the work reported herein, the scattered signal is assumed to be describable by the so-called Rayleigh scattering model which is based on a large number of individual scatterers of uniformly distributed phase and either equal or random amplitudes (see p. 265 of [8]). The Rayleigh model is equivalent to two quadrature (independent, equal-variance, zero-mean) Gaussian variables, which for a linear detector yields a Ralyeigh envelope distribution. Much has been written on the subject in past altimetry reports; very good general references are Van Trees [9], Skolnik [10], and Burdic [8]. It will suffice here to state a few results from

---

*An abbreviated digital simulation was used in the RTI altimeter study in 1970 [14].

Simulation of
"smooth-sea"
backscattered
autocorrelation

(+)

thermal
noise

Random Noise
Generator

Altimeter
Pre-detection
Simulation
(IF = 2 pole pairs)

Detector
Square-law,
Linear, etc.

Video
Filter,
2 pole

Computation
Cycle
Clock

Delay

"Sea State"
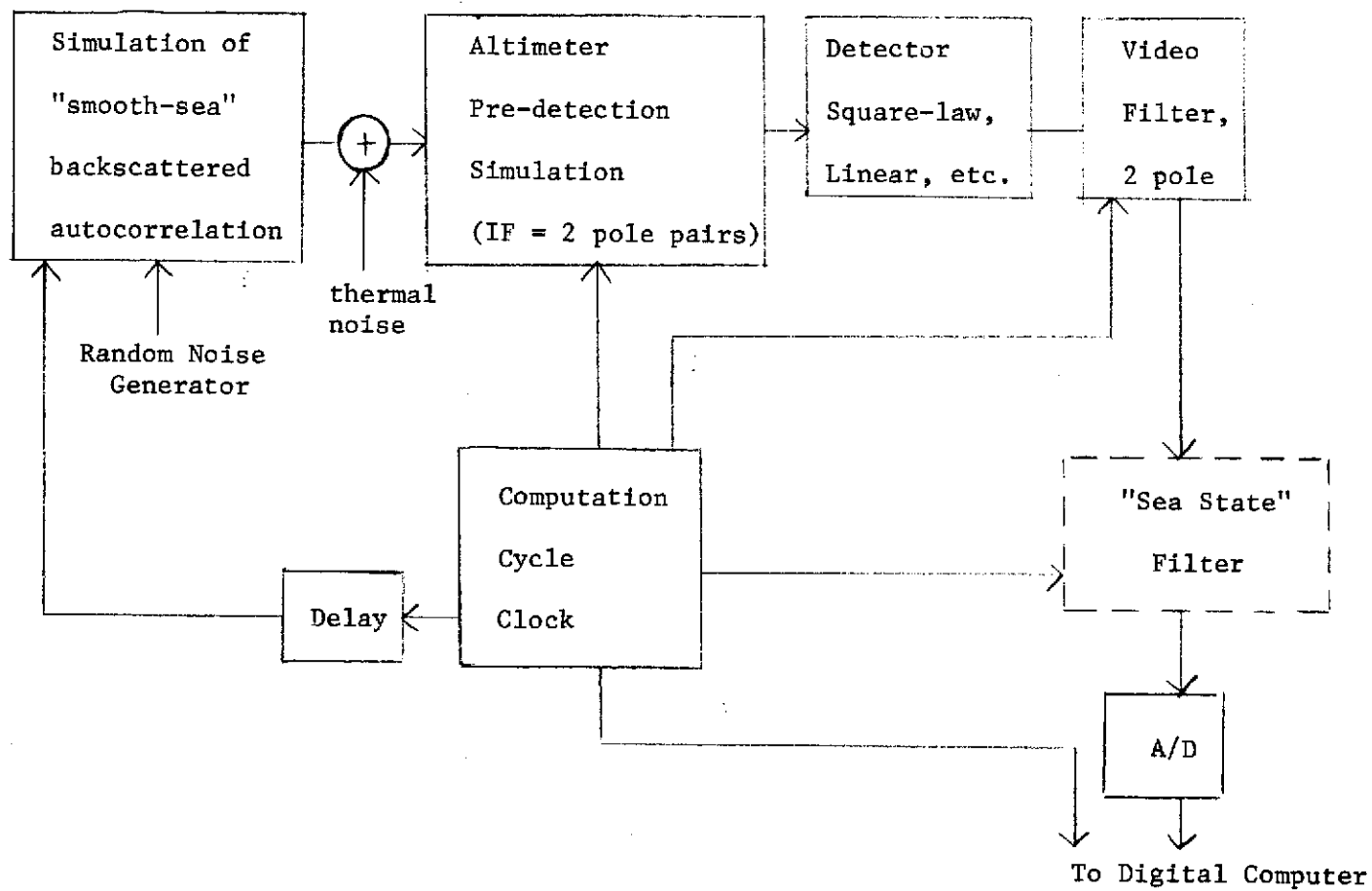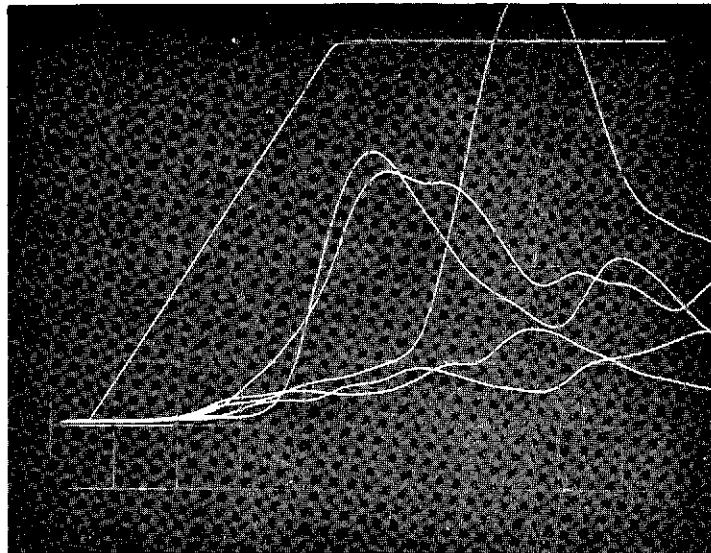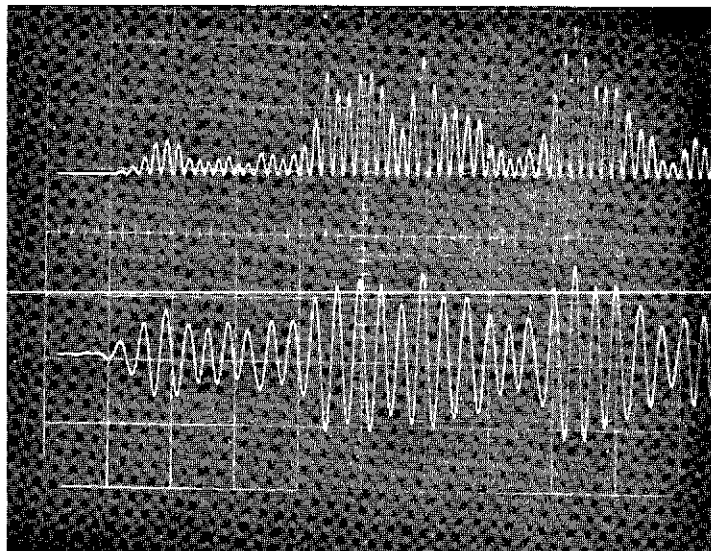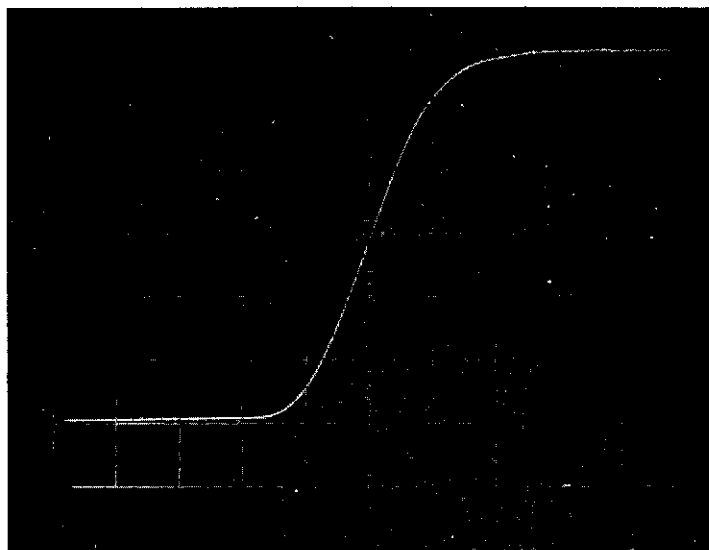Filter

A/D

To Digital Computer

Figure 18.   Functional diagram of Analog System.

upper trace = deterministic 10 ns ramp for time reference
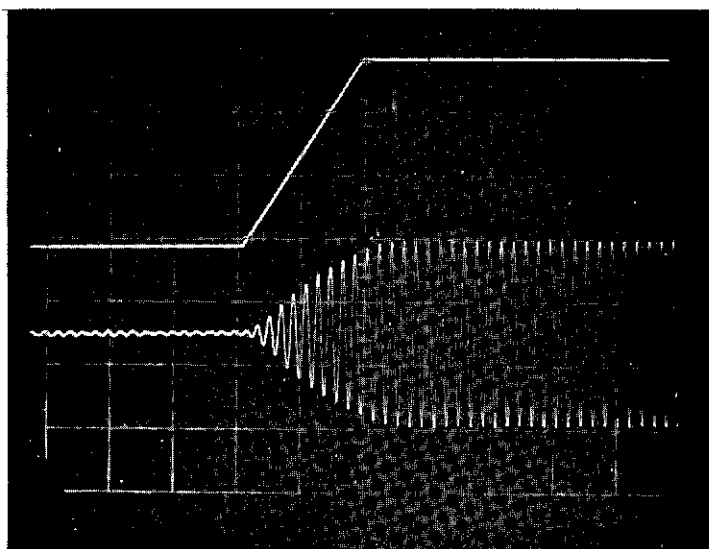lower trace = five independent video waveforms

upper trace = typical detector waveform
lower trace = typical IF waveform

Figure 19. Typical waveforms at different points in the S-193 analog simulation

video signal

upper trace = simulated 10 nanosecond ramp
lower trace = detector waveform

Figure 20.   S-193 analog simulation waveforms for the deterministic
case

Ref. [9]. The main assumptions in the theory are those of linear, nondispersive (with r-f frequency) scattering. With very wideband signals (e.g.,large pulse compression ratios) these assumptions should be carefully considered.

The received signal may be shown to be given by

$$\tilde{s}(t) = \int_{\ell_o}^{\ell_1} \tilde{f}(t - \alpha)\tilde{b}_r(\alpha) \, d\alpha$$

where the tildes are complex signal notation and

$\tilde{b}_r(\cdot)$ = random impulse response of reflection process of spatial variable α over (ℓ_o, ℓ_1)

$\tilde{f}(\cdot)$ = transmitted waveform which for a linear theory may include receiver effects.

If $\tilde{b}_r(\alpha)$ is complex Gaussian, the output is also Gaussian and the covariance completely describes the process and it is

$$\tilde{K}_{\tilde{s}}(t,u) = \int_{-\infty}^{\infty} \tilde{f}(t - \alpha) \, E[|\tilde{b}_r(\alpha)|^2] \, \tilde{f}^*(u - \alpha) \, d\alpha \tag{14}$$

where E is expectation. If the scattering process is taken to be only area dependent,

$$E[|\tilde{b}_r(\alpha)|^2] = \text{a constant for } \alpha > \ell_o$$

$$= U(\alpha - \ell_o)$$

where U is the unit step. Therefore

$$\tilde{K}_{\tilde{s}}(t,u) = \int_{-\infty}^{\infty} \tilde{f}(t - \alpha) U(\alpha - \ell_o) \tilde{f}^*(u - \alpha)\ d\alpha, \quad t \geq u \tag{15}$$

and the variance expression is (t = u)

$$\tilde{K}_{\tilde{s}}(t = u) = \int_{\ell_o}^{\infty} \tilde{f}(t - \alpha)\ \tilde{f}^*(t - \alpha)\ d\alpha \quad . \tag{16}$$

Using this form of $\tilde{b}_r$, and a transmitted signal comprising a rectangular pulse which begins at $t = 0$ and terminates at t_1, the convolution of these quantities leads to a time-varying process with linearly increasing variance over $0 \leq t \leq t_1$, and constant variance for $t > t_1$.

In the simulation, the above effects are modeled as follows: the non-stationary (ramp) behavior of the process variance is modeled by the product operation shown in Figure 21. Correlation properties of the signal are approximated by the filter $H(s)$ which for a transmitted rectangular pulse $H(s)$ would comprise a $[(\sin x)/x]^2$ spectrum or a triangular* autocorrelation function. An analog method of generating the sin x/x property is shown in Figure 22. It consists of implementing the transfer function

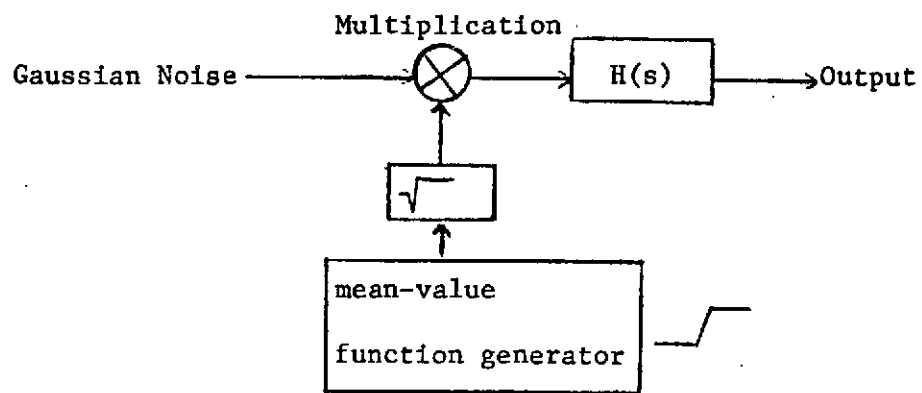$$H(s) = \frac{1 - e^{-Ts}}{s}$$

---

*As baseband equivalents
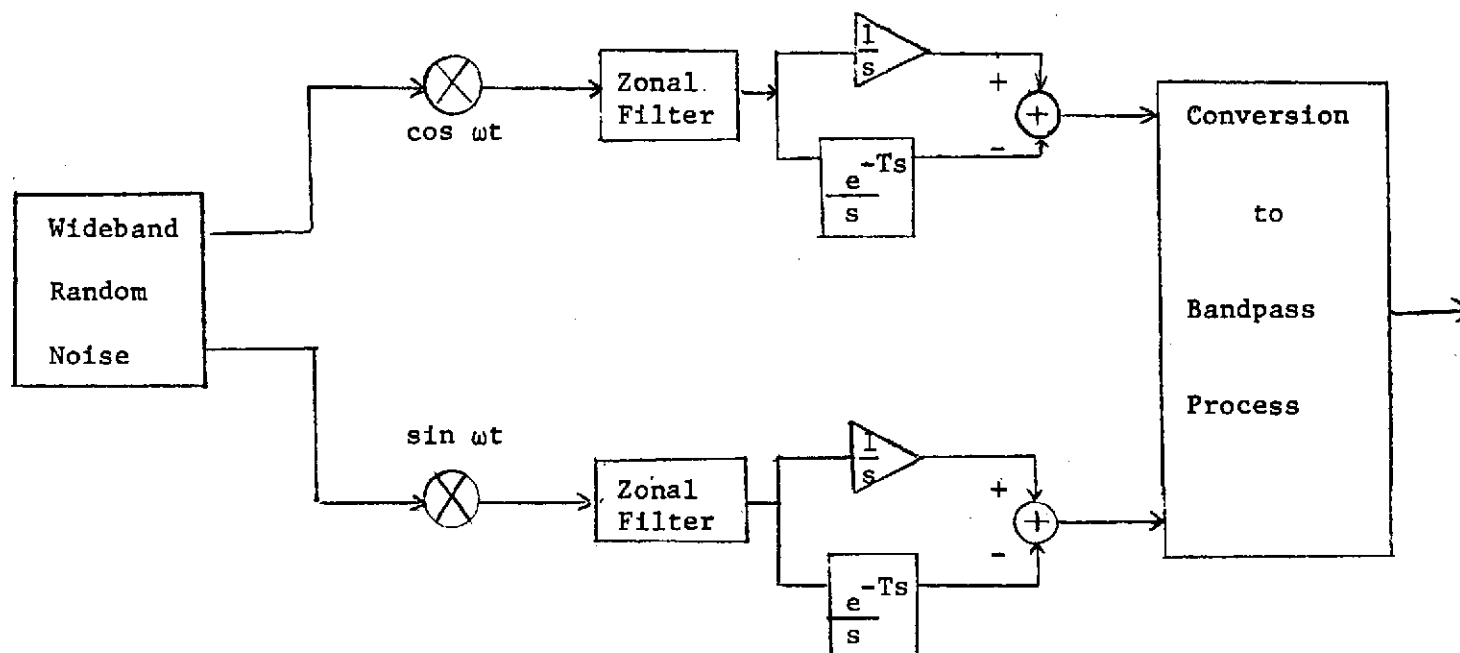
Figure 21. Simulation of time-varying signal.

Figure 22. Generation of (sin x)/x correlation

as a baseband process. A program for direct generation of the bandpass process has been designed; however, it is much less convenient to use. The delay operation e^{-Ts} will be discussed later.

It can be argued that transmitter bandpass functions will cause an actual spectrum to depart from a $(\sin x/x)^2$ envelope and much simpler filter operations could be used. This is partially true; however, in the writers' experience microwave radar transmitters have been found to radiate signals containing pronounced spectral sidelobes. It is thus felt that the simulation should provide for some lobular structure. In the sea-state simulations this factor is less critical and a simpler $H(s)$ function was used. However, modeling of the received signal properties is of critical importance in studies intended to optimize IF bandwidth, detector type, video filtering, and tracker functions versus altimeter accuracy. This last task has not as yet been initiated.

IF and Video Filter Operations

The IF amplifier and video amplifier are programmed using maximally flat transfer functions consisting of two-pole pairs and two-poles, respectively. Design bandwidth of multiples of 0.5, 1.0, 2.0, and 10.0 of matched conditions are utilized where "matched" is defined as two times the reciprocal pulse length for the IF and the reciprocal pulse length for the video. In order to fit the overall programs on the analog facilities available, the IF amplifier simulation has been constructed as a separate entity using commercially available operational amplifiers.

Sea-State Simulation

In the hybrid simulation the effect of ocean surface roughness is modeled through use of a post-video filter which is designed to model expected radar observed wave height distributions. Previous analyses have shown that this effect may be mathematically represented as a convolution of the radar video signal with the ocean impulse response $p(z)$ [1]. For purposes of this analysis, a series of Gaussian impulse response functions were used to investigate sensitivity of the S-193 experiment to sea-state conditions.

Analog computer programming of the p(z) functions used in the simulation was first attempted using the method of Kastelein [11] in which the desired p(z) function is first expressed as a repetitive form and even and odd parts of the transfer function are used to approximate the nonrepetitive p(z) network function. This method was found to produce highly sensitive, marginally stable transfer functions, and the following method was developed instead.

To describe the method used to generate an analog program approximating a Gaussian impulse response, consider the Laplace transform H(s) of an impulse response h(t) comprising one cycle of a cosine function over $-\pi$ to π and a dc level

$$h(t) = \frac{1}{2} [1 - \cos(2\pi kt - \pi)] \quad 0 \le t \le \frac{1}{k}$$

$$= 0 \qquad \text{otherwise .} \tag{17}$$

The transform is readily found to be

$$H(s) = \frac{1}{2} [\frac{1}{s} - \frac{s}{s^2 + (2k\pi)^2} - e^{-\frac{s}{k}} (\frac{1}{s} - \frac{s}{s^2 + (2k\pi)^2})] \tag{18}$$

which shows that a truncated time function can be constructed by delaying and differencing the repetitive waveform. The delay function can be implemented using a number of well-known techniques. The one to be used in the sequel is a fourth order Padé approximation [12].

Next consider the use of other functions. The Gaussian function was programmed by finding the Fourier series representation of a Gaussian curve truncated at $\pm$ three sigma and starting at t = 0, i. e.,

$$h(t) = e^{-\frac{1}{2}(t - 3)^2} \qquad 0 < t \le 3 \tag{19}$$

$$= 0 \qquad \text{otherwise}$$

which has the series representation for $\omega = \frac{2\pi}{3}$

$$h(t) = .416 - .486\cos\omega t + .088\cos 2\omega t - .01\cos 3\omega t - .003\cos 4\omega t + .006\cos 5\omega t + \ldots \ .$$

Then H(s), the Laplace transform of this series representative of h(t) is given by

$$H(s) = \frac{.416}{s} - \frac{.486s}{s^2 + \omega^2} + \frac{.088s}{s^2 + 4\omega^2} - \ldots \ . \tag{20}$$

A three term approximation to the Gaussian function was found to be an adequate representation, with the greatest error arising from the fourth order Padé approximation. This program is shown in Figure 23. The fit to a true Gaussian is within about ± 5%. For greater accuracy, a sixth or eighth order Padé network would be needed.

2.3.3 Digital Computer Simulation

The digital computer functions are divided into two major areas: studies of (1) ocean surface roughness and sampling aspects and (2) effects of system variations on overall altimeter precision.

Discussing category one first; the digital functions consist of simulation of the S & H operations, reconstruction of the sampled waveforms, and statistical computations. The weighting and sampling characteristics of the S-193 system are taken to be representable in the 10 ns case as final value samples of exponentially weighted values extending backward in time by two time constants. Oscilloscope photos of the sample weighting functions were shown in Figure 11.

For purposes of this study, a (sin x)/x interpolation type of reconstruction filter is used. In processing actual S-193 data, it may be advisable to use the technique developed by Slepian and Pollak [13] or to use a minimum variance Wiener Filter [7]. Also note that satellite data may be reconstructed using separate batches of S & H data spaced by 10 ns or the two batches interleaved 5 ns apart. If waveform data from the various S & H array locations are mixed prior to reconstruction, a non-uniform density of sample values spaced 5 rather than 10 ns results.
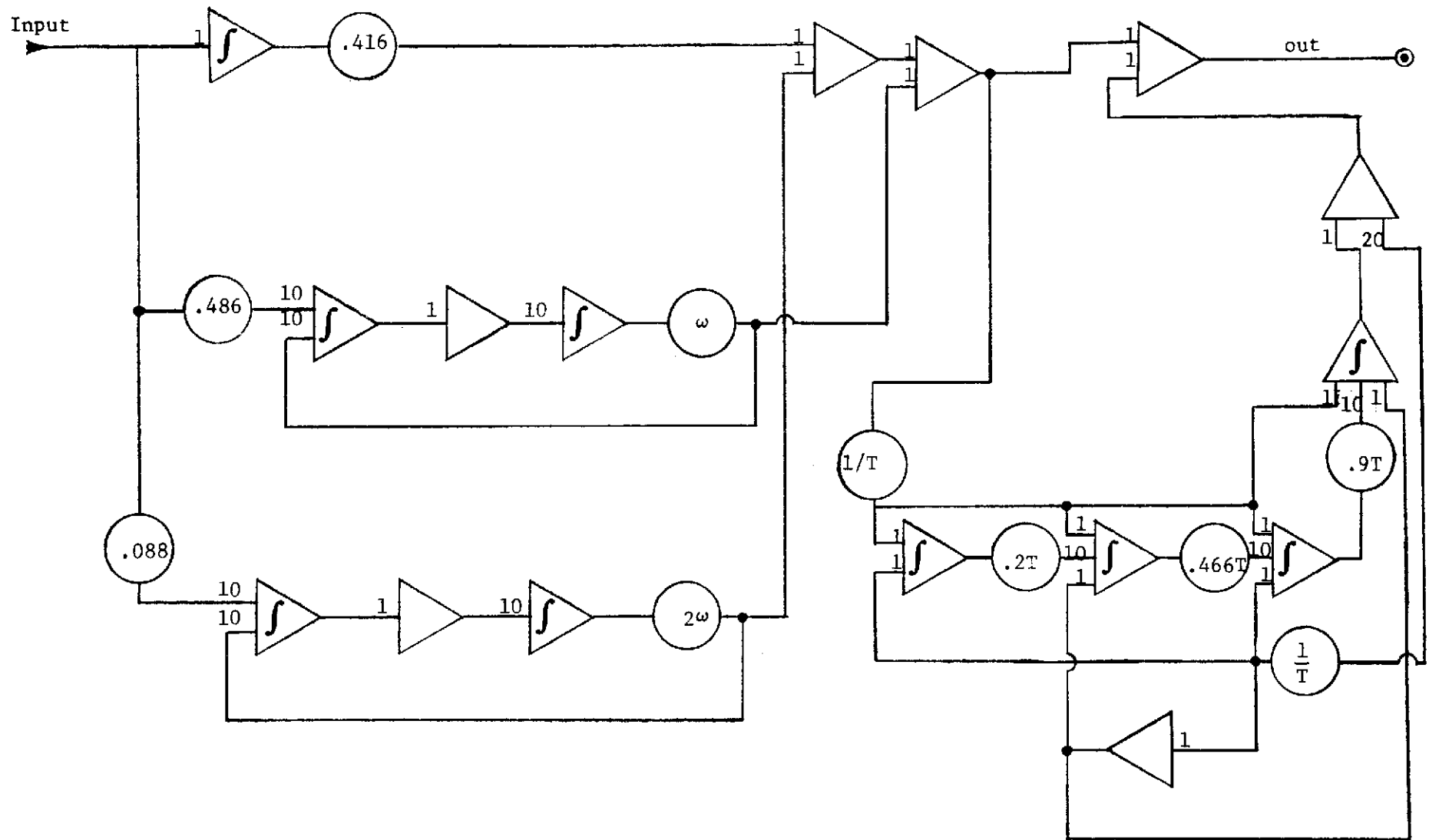
Figure 23. Analog program for the Gaussian function generator

Statistical processing consists of (1) densely sampling (around 100 values) each waveform and (2) averaging the values to obtain mean waveforms, histograms, and variance values.

Digital simulation of the altitude tracker is based on an equivalent closed-loop method suggested by E. L. Hofmeister of G. E., Utica, New York. In it, open-loop measurements with a split-gate tracker are analytically converted into closed-loop values. Digital implementation of the split-gate tracker consists of uniformly weighting the two gate regions with selectable spacing. These two values for each waveform are then weighted to effect a time-discrimination characteristic. Details of the closed-loop transformation are discussed in Appendix B. Mean waveforms for the noise-free and ∿6 dB SNR case are shown in Figure 24.
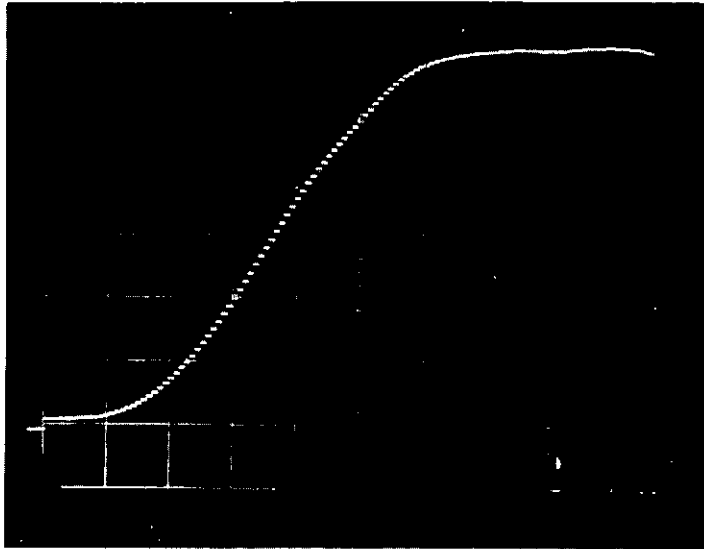
signal only present
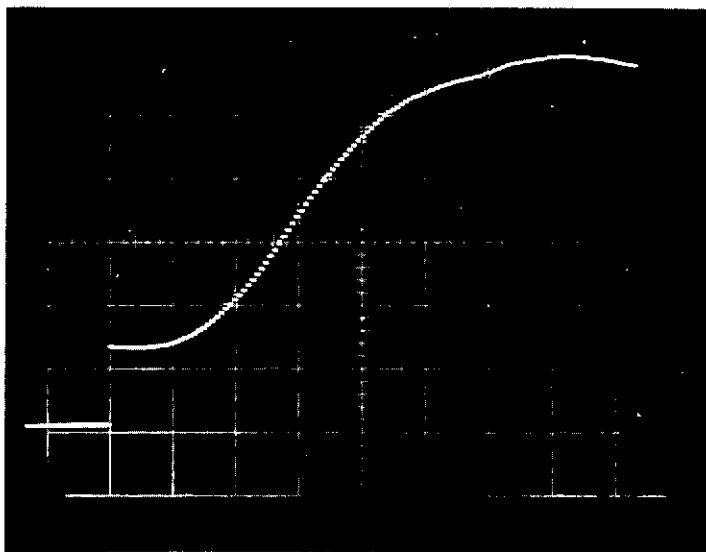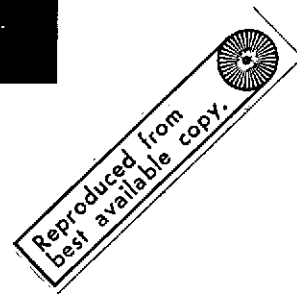
signal plus receiver noise (SNR∿6db)

Figure 24.   Simulated mean waveforms obtained by averaging 1000
individual waveforms (simulated sweep-rate 2.5ns/cm)

APPENDIX A

VIDEO FILTER AND SAMPLER SIMULATION RESULTS

The objectives of this Appendix are to present data relevant to the problems of:

1. determining filter characteristics of the weighting function or aperture effect of the S-193 sampling function;

2. comparing the system responses for various types of video amplifier response in light of the importance of the exponential sampler in establishing overall response; and

3. describing the S-193 system response adequately for the formulation of the sea-state integral solution.

These effects have been investigated by simulation of the S-193 parameters for the above delineated conditions. Figures A-1 and A-2 display the mean waveform response for four types of video filters shown in the upper trace (RC, Butterworth, Bessel, and Chebyshev), and the resultant sampler response for each filter shown in the dotted trace. The sampler response in these figures was obtained by digitally sampling the simulated waveforms with exponential/truncated weights as described in paragraph 2.2 in an overdense sample pattern to display transient characteristics of the finite-aperature sampling process. Examination of the four filter cases given in Figures A-1 and A-2 indicates the expected behavior. Overshoot characteristics of these 2-pole filters may be described by the equivalent damping factor ζ as given below in the normalized form $H(s) = \left[1 + 2\zeta \frac{s}{\omega_o} + \left(\frac{s}{\omega_o}\right)^2 \right]^{-1}$

RC $\qquad\qquad \frac{1}{s^2 + 2s + 1}$; $\zeta = 1$

Bessel $\qquad\quad \frac{1}{s^2 + 1.72 s + 1}$; $\zeta = .86$

Butterworth $\qquad \frac{1}{s^2 + \sqrt{2} s + 1}$; $\zeta = .707$

Chebyshev $\qquad \frac{1}{s^2 + s + 1}$; $\zeta = .5$.
$\epsilon = .58$

As would be expected for these ζ factors, the filters display the appropriate degree of overshoot and rise-time. Either the second or the third case is considered to be acceptable. The Bessel filter is considered to represent a good compromise between rise-time and overshoot; it also has better symmetry about the 50% point than do the other cases, and is generally recommended for waveform studies. The lower trace, whose maxima represent the response of the 10 ns gate length used in S-193, demonstrates the comparative ramp response of each of these filters as viewed at the output of the sample function. These results show the S-193 system to be only slightly affected by the exact type of video response present. Indeed, it is necessary to simulate rather extreme overshoot, such as the Chebyshev case given, for overshoot characteristics to be easily discernable in the sampled waveform. For this reason we wish to further examine response characteristics of the S-193 sampler.

Based on the 10 ns (at e^{-2} point) gate length and exponential response of the S-193 sampling function, one might expect the sampler response could be modeled as an RC filter with time constant (e^{-1}) of 5 ns. This case is shown in Figure A-3-A. Comparing this behavior with the results of the previous figures clearly indicates that such a filter does not match the S-193 system response. Figure A-3-B shows an RC filter with a shorter time constant (corresponding to a corner frequency of 50 MHz) which provides a much better comparison. On this basis, we conclude that the behavior of the S-193 (finite aperture) sampler is representable to good approximation as a continuous-time equivalent 50 MHz RC filter. It is also concluded that the sea-state estimation process is reasonably insensitive to video amplifier characteristics.

For purposes of documentation, Figure A-4 shows the simulated ramp responses (10 ns) of the 2-pole video filter only, for the Bessel and Butterworth cases.
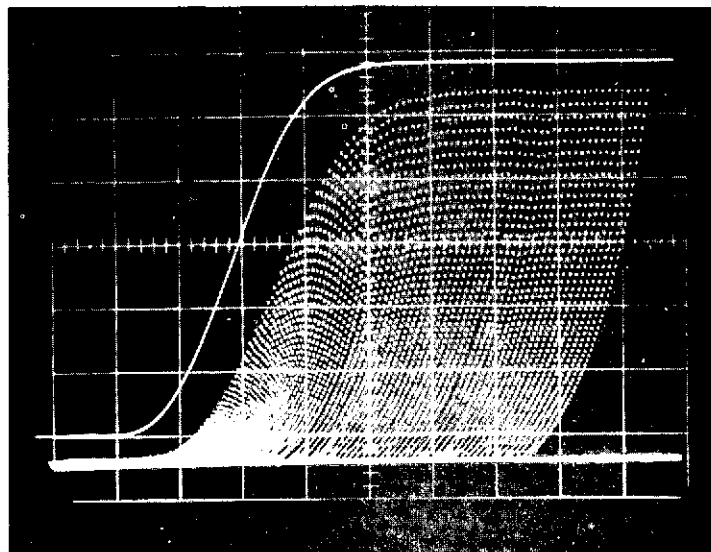
Video Filter - 2-pole RC
$$f_{3db} = 50 \text{ MHz}$$
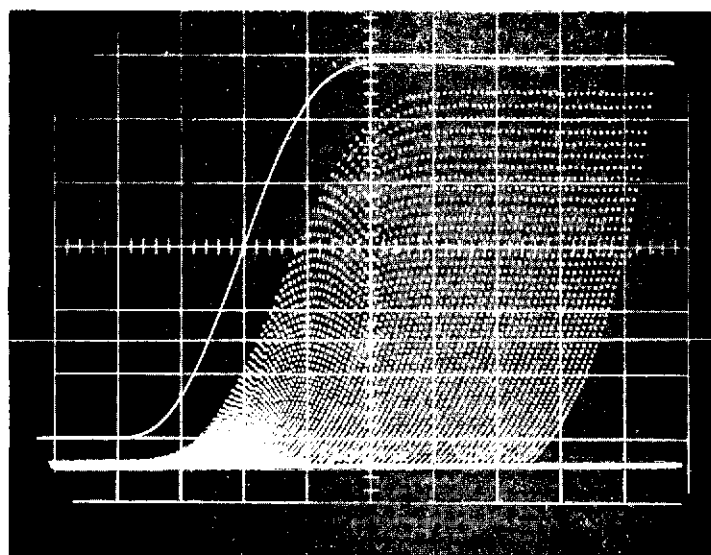
Video Filter - 2-pole Bessel
$$f_{3db} = 50 \text{ MHz}$$

Figure A-1 Comparison of Video (solid trace) and Sampler Waveforms
            (simulated sweep-rate = 5ns/cm)

2-54
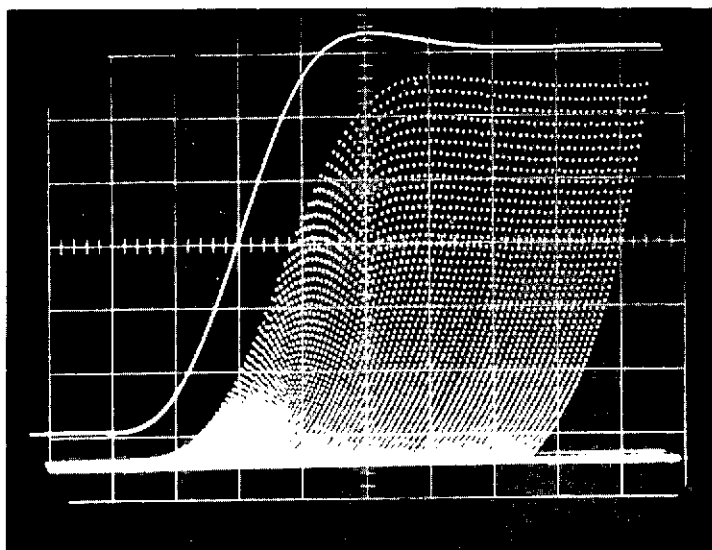
Video Filter = 2-pole Butterworth
$$f_{3db} = 50 \text{ MHz}$$
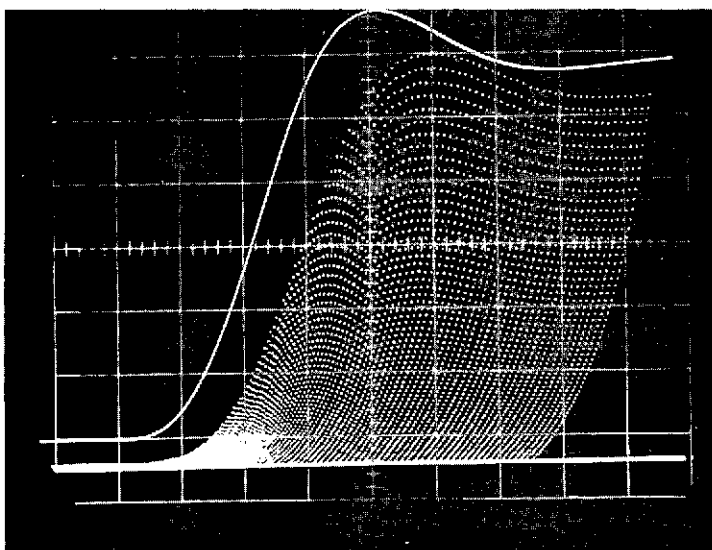
Video Filter = 2-pole Chebychev
$$\varepsilon \sim .58$$
$$f_{3db} = 50 \text{ MHz}$$

Figure A-2. Comparison of Video (solid trace) and Sampler Waveforms
(simulated sweep-rate 5ns/cm)

A.   RC 3db Bandwidth = 31.4 MHz
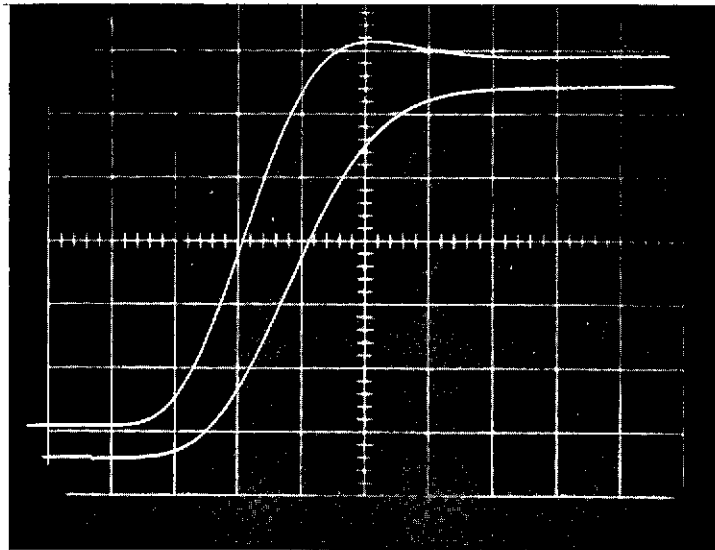
(T = 5ns)

A. RC 3db Bandwidth = 31.4 MHz

(T = 5ns)
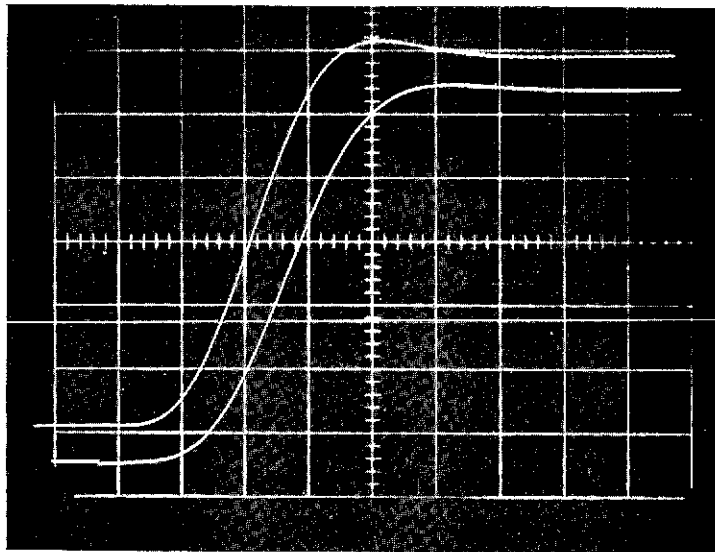
B. RC 3db Bandwidth = 50 MHz

Figure A-3   System Response with a 2-pole Butterworth video filter and
1-pole RC (to simulate sampling weights)
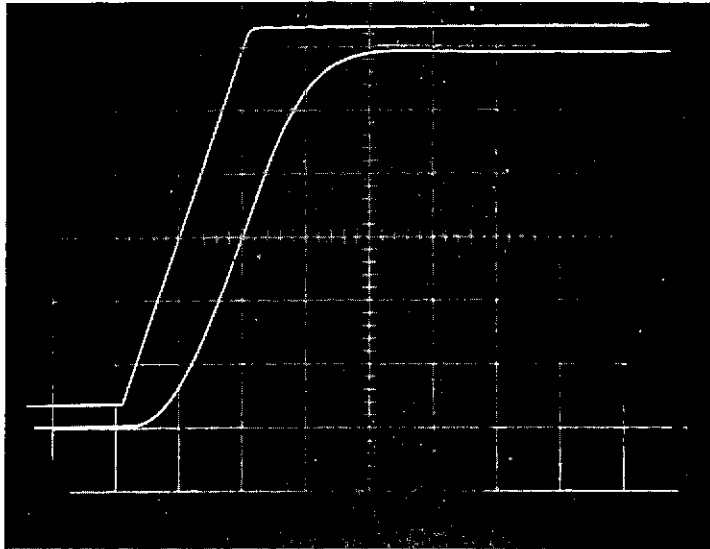
BESSEL
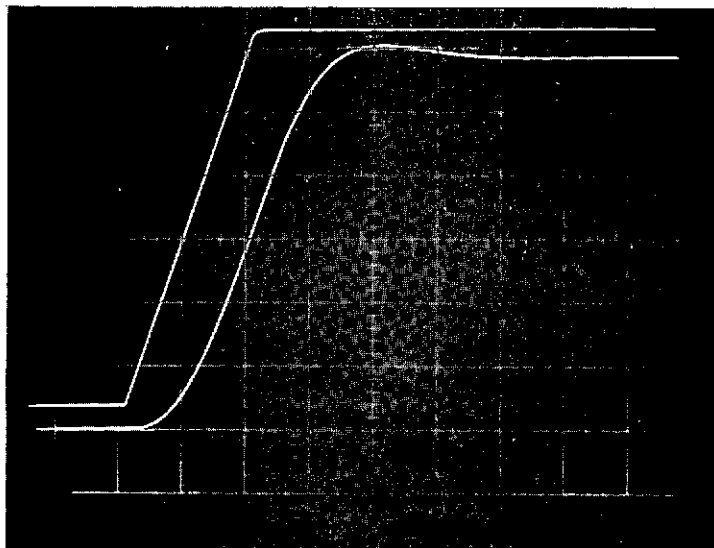
BUTTERWORTH

Figure A-4   Ramp response of Video Filter only
             (simulated sweep-rate = 50 ns/cm)

The purpose of this appendix is to describe the method developed by Hofmeister [2] for computing closed-loop altitude tracker characteristics. It consists of the conversion of ensemble-member video waveforms $y_i(t)$ into equivalent tracking loop noise $e_o(i)$, and subsequently into tracking loop error variance. This is shown below.
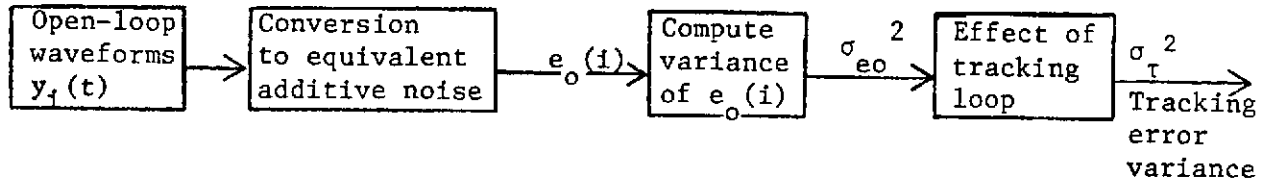
Computation of $e_o(i)$ is based on the equation

$$e_o(i) = \int_{\infty}^{\infty} \left[y_i(\alpha) - \overline{y_i(\alpha)} \right] r(\alpha) d\alpha \qquad (B-1)$$

in which $\overline{y_i(\alpha)}$ is the mean value of $y_i(\alpha)$ and $r(\alpha)$ is the tracker gate function shown below.
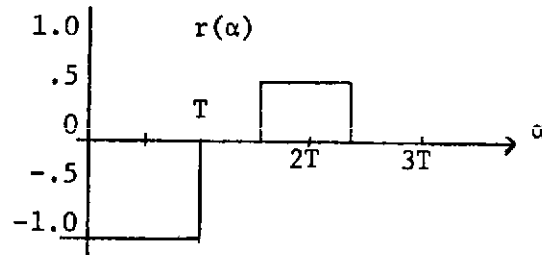
In the digital implementation, the two terms in the integrand are computed as separate integrations, and the variance of $e_o(i)$ is then formed. The final result, σ_τ^2, is obtained via equation A-22 of [2] i.e.,

$$\sigma_\tau^2 = \sigma_{eo}^2 \frac{1}{2\pi j} \int_\Gamma z^{-1} B(z) B(z^{-1}) dz \qquad (B-2)$$

$$\Gamma = \text{unit circle}$$

which is a tabulated integral; $B(z)$ is a discrete-time transfer function
which describes the feedback loop (see A-14 of [2]). On this basis σ_τ^2
can be written as

$$\sigma_\tau^2 = \frac{\sigma_{e\delta}^2}{R^2}$$

where R^2 is a variance reduction factor which is given to good approximation
by [2]

$$R^2 = \frac{PRF}{\pi B_1} \quad .$$

These symbols were defined in section 2.1. A computer program for determination
of R^2 is available from E. Hofmeister; its inputs are

K_v = velocity gain

f_c = crossover frequency

T_o = sampling interval (1/PRF)

and the program calculates R^2 for a specific loop design.

REFERENCES

1. Miller, L. S. and G. S. Hayne, "System Study of the Geodetic Altimeter Concept," NASA Contract No. NAS6-1829, Final Report, Research Triangle Inst. Research Triangle Pk. N. C., March 1971.

2. Hofmeister, E. L. and B. N. Keeney, "Radar Altimeter Return Waveform Sampling Study," NASA Contract No. NAS6-1823, Final Report, The General Electric Company, Utica, New York, October 1971.

3. Gibson, J. E., Nonlinear Automatic Control, McGraw-Hill, New York, 1963.

4. Papoulis, A., "Error Analysis in Sampling Theory," Proc. IEEE, Vol. 54, No. 7, July 1966.

5. Harmon, W. J., Principles of Statistical Theory of Communications, McGraw Hill Book Company, New York, 1963.

6. Hildebrand, F. B., Methods of Applied Mathematics, Prentice Hall, Englewood Cliffs, New Jersey, 1965.

7. Freeman, H., Discrete Time Systems, John Wiley & Sons, New York, 1965.

8. Burdic, W. S., Radar Signal Analysis, Prentice Hall, Englewood Cliffs, New Jersey, 1968.

9. Van Trees, H. L., Detection, Estimation and Modulation Theory, Part III, John Wiley and Sons, New York, 1971.

10. Skolnik, M. I., "A Review of Radar Sea Echo," Naval Research Laboratory Report No. 2025, Washington, D. C., 1969.

11. Kastelein, Arend, "A New Sine-Squared Pulse and Bar Shaping Network," IEEE. Transactions on Broadcasting, Vol. BC-16, Number 4, pp. 84-89, December, 1970.

12. Jackson, A. S., Analog Computation, McGraw Hill Book Co., N. Y., 1960.

13. Slepian, D. and H. Pollak, "Prolate Spheroidal Wave Functions, Fourier Analysis and Uncertainty - I," Bell System Tech. Journal, Vol. 40, Jan. 1961.

14. Research Triangle Institute, "A Study of the Capabilities of the Geodetic Satellite Altimeter to Measure Ocean Surface Characteristics," NASA CR 110085, April, 1970.

CHAPTER 3

RADAR CROSS SECTION CHARACTERISTICS FOR NEAR-NORMAL INCIDENCE
BACKSCATTER GEOMETRY

3.0 INTRODUCTION

This chapter examines the relationship between the ocean surface
wavenumber spectrum $S(k)$ and the microwave backscatter cross-section per
unit area, σ^o, as calculated by a physical optics integral for the near-
normal incidence case. Specifically, it is necessary to know that range
of wavenumbers, k, which provides the major contribution to σ^o, because
ground-truth activities to support the Skylab microwave backscatter ex-
periment must be designed to obtain maximum information in that k-range.
The link between the surface spectrum $S(k)$ and σ^o is the autocorrelation
function $\rho(r)$ which is the Fourier transform of $S(k)$, and which appears
in the physical optics integral for σ^o.

The transformation from $S(k)$ to $\rho(r)$ may not be accomplished in closed
form for most currently accepted spectral descriptions of the ocean's surface
even if the spectrum is assumed to be non-directional. It is possible to
evaluate σ^o numerically by performing the $S(k) \rightarrow \rho(r)$ transformation numeri-
cally and this has been done by Chia [19], but insight tends to disappear
within the details of the computer programming. It is possible, however,
to chose a form for $S(k)$ which has the k^{-4} Phillips behavior for large k,
is reasonably good at representing experimental data even at low k, and
yet does lead to a closed form result for $\rho(r)$ under the isotropic assumption.
This spectral form, $S_a(k)$, is discussed in Section 3.1. By requiring that $S_a(k)$
have the same mean-square waveheight as the Pierson-Moskowitz spectral form [2],
it is possible to bring a wind speed dependence into $S_a(k)$.

This spectrum is then used in Section 3.2 to find σ^o for a range of wind
speeds and angles of incidence, and the results obtained are compared with
Guinard's experimental results [14]. The inapplicability of function expansion
techniques in this problem is also discussed as is the error in approximate
integration techniques.

Section 3.3 examines the effects on σ^o of truncating the spectrum $S_a(k)$
as a means of determining relative importance of different spectral regions.
To carry this out, approximate expressions are developed for the auto-
correlation function from the truncated $S_a(k)$ and the validity of the
approximation is checked by comparison with the results of Section II.

The results of Section 3.3 show that σ^o depends strongly on the ocean spectral characteristics for surface wavelengths in the range .06 to 60 meters but that backscattering is insensitive to all wavelengths shorter than 6 centimeters, the capillary range.

Section 3.4 examines the possible changes in the σ^o result as the isotropic assumption is removed. The directional spectra of Cote et al.[15] and Longuet-Higgins et al.[17] are used and it is shown that the isotropic part of $\rho(r,\phi)$ dominates the σ^o result with negligible contributions from the anisotropic components. This is a significant result as it would considerably simplify the task of ground truth data acquisition.

3.1 THE ASSUMED OCEAN SURFACE SPECTRAL FORM AND THE SCATTERING FORMULATION

In order to utilize the physical optics theoretical foundation it is first necessary to adopt an analytical expression for the spectrum of wind-generated ocean waves. Oceanographers have for many years attempted to define empirical or theoretical models of the wave-height spectrum. The model to be used herein is based on the works of Phillips [1], Pierson and Moskowitz [2], and the experimental results given in Hess, Hidy, and Plate [3]. The starting point will be the Phillips equilibrium spectrum which assumes that surface conditions have existed for a sufficient time period that fully developed or steady state surface statistics exist. This model also assumes that an upper limit on the growth of waves exists beyond which wave breaking occurs, and that swell from distant storms is negligible. Because of its equilibrium nature, this spectrum is in some sense an upper bound. The Phillips asymptotic behavior of k^{-4} (in wavenumber space) will be used to describe the high wavenumber form of the spectral model. The model's low wavenumber asymptote is based on the data shown in Figure 1. This figure suggests that a rational polynomial approximation may be useful in describing the spectrum. A function which is amenable to integration and will subsequently be shown to be a good approximation to experimental data is

$$S_a(k) = \frac{\beta k^4}{(k^2 + a^2)^4} \qquad k \leq k_c \qquad (1)$$

where $S_a(k)$ is the isotropic wavenumber spectrum, and a and β are constants to be determined. It should be noted that the same dimensional arguments that predict k^{-4} behavior also lead to ω^{-5} (ω = radian frequency) asymptote, quite independent of the particular form of the dispersion relationship. For convenience in selecting constant values, the mean-square height resulting from $S_a(k)$ will be equated to the mean-square height resulting from the Pierson-Moskowitz spectrum [2] $S_b(k)$ where*

---

*Both $S_a(k)$ and $S_b(k)$ may be considered to be a specialized form of the more general two-dimensional spectrum $\Psi(k,\psi)$; without loss of generality, one can write $\Psi_a(k,\psi) = S_a(k)F(k,\psi)$ and similarly for $S_b(k)$. Then the isotropic assumption simply implies $F(k,\psi)=1$.
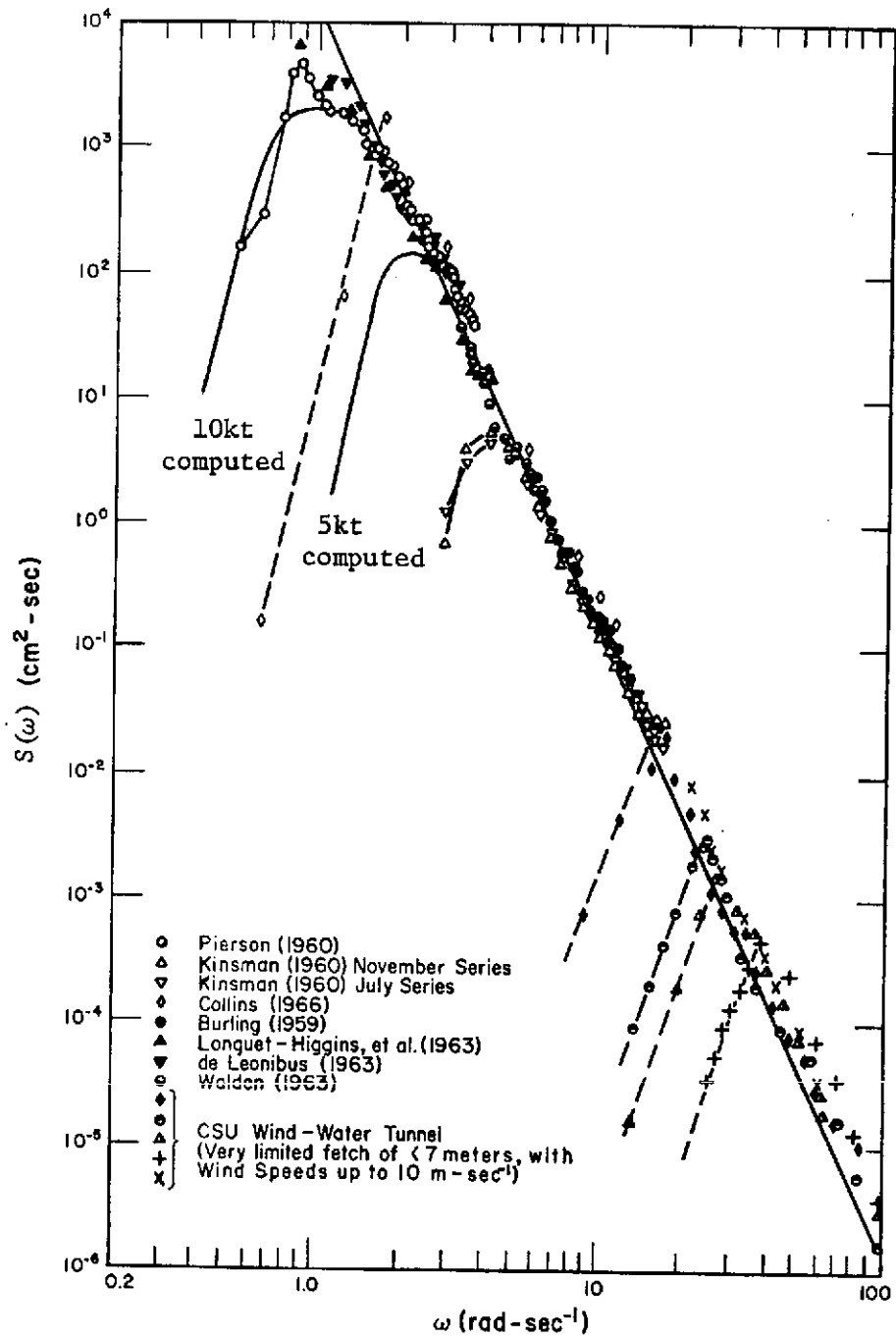
Figure 1. Data Summary from Hess, Hidy, and Plate [3], with $S_a(k)$ plotted for 5 and 10 knots wind speed.

$$S_b(k) = \frac{\beta'}{k^4} \exp\left[- [9.5k^2v^4]^{-1}\right] \qquad k < k_\nu \qquad (2)$$

and $\beta' = 4.05 \times 10^{-3}$ and k and v have dimensions of (centimeters)$^{-1}$ and knots. The upper bound of k_ν in (2) indicates a lack of knowledge of the spectrum in regions beyond the gravity wave range, and the k^{-4} Phillips behavior is obviously contained in (2). Other exponent values of k in the numerator of (2) have been given in the literature ranging from 3.721 to 4.5 [see Bass [4] and Valenzuela [5]]. Imposing the requirement that $S_a(k)$ and $S_b(k)$ yield the same mean square height, i.e.,

$$\int_o^\infty S_a(k)kdk = \int_o^\infty S_b(k)kdk,$$

results* in the constant a^2 having the value $(28.5v^4)^{-1}$ and $\beta = \beta'$. Normalized plots of $kS_b(k)$ and $kS_a(k)$ are shown in Figure 2 to illustrate the effect of requiring mean-square height equality.

In order to compare the above spectrum model with experimental data, it is necessary to re-express it in the frequency domain. Using the gravity range dispersion relationship the radian frequency (ω) spectrum can be shown to be

$$S_a(\omega) = \frac{2\beta g^2 \omega^{11}}{(\omega^4 + a^2 g^2)^4} \qquad .$$

Graphs of the above are given in Figure 1 for two values of wind speed and for the relationship $a^2 = (28.5v^4)^{-1}$. This figure also contains experimental data from a number of sources. The data from Collins was recorded in the proximity of Hurricane Dora and the data from Kinsman corresponds to limited fetch conditions. Only the data from Pierson and Longuet-Higgins appears to correspond to near-equilibrium conditions for the lower frequency range components. Figure 1, therefore graphically depicts the paucity of data available in the high energy spectral range. The comparison of this model with the Pierson data is reasonably good; to match the reported wind speed condition (18 knots) would require slight modifications of the parameter $a^2 = (28.5v^4)^{-1}$.

---

*Note that a must have the same dimensions as k; in this report k is in (cm)$^{-1}$ and v is in knots. For any other units of k or v, the factor 28.5 will change.

$$S_b(k) = \frac{\beta}{k^4} e^{-3a^2/k^2}$$

$$S_a(k) = \frac{\beta k^4}{(k^2 + a^2)^4}$$

$$a^2 = \frac{1}{28.5v^4} ; \quad k \text{ in } cm^{-1}$$

and v in knots.
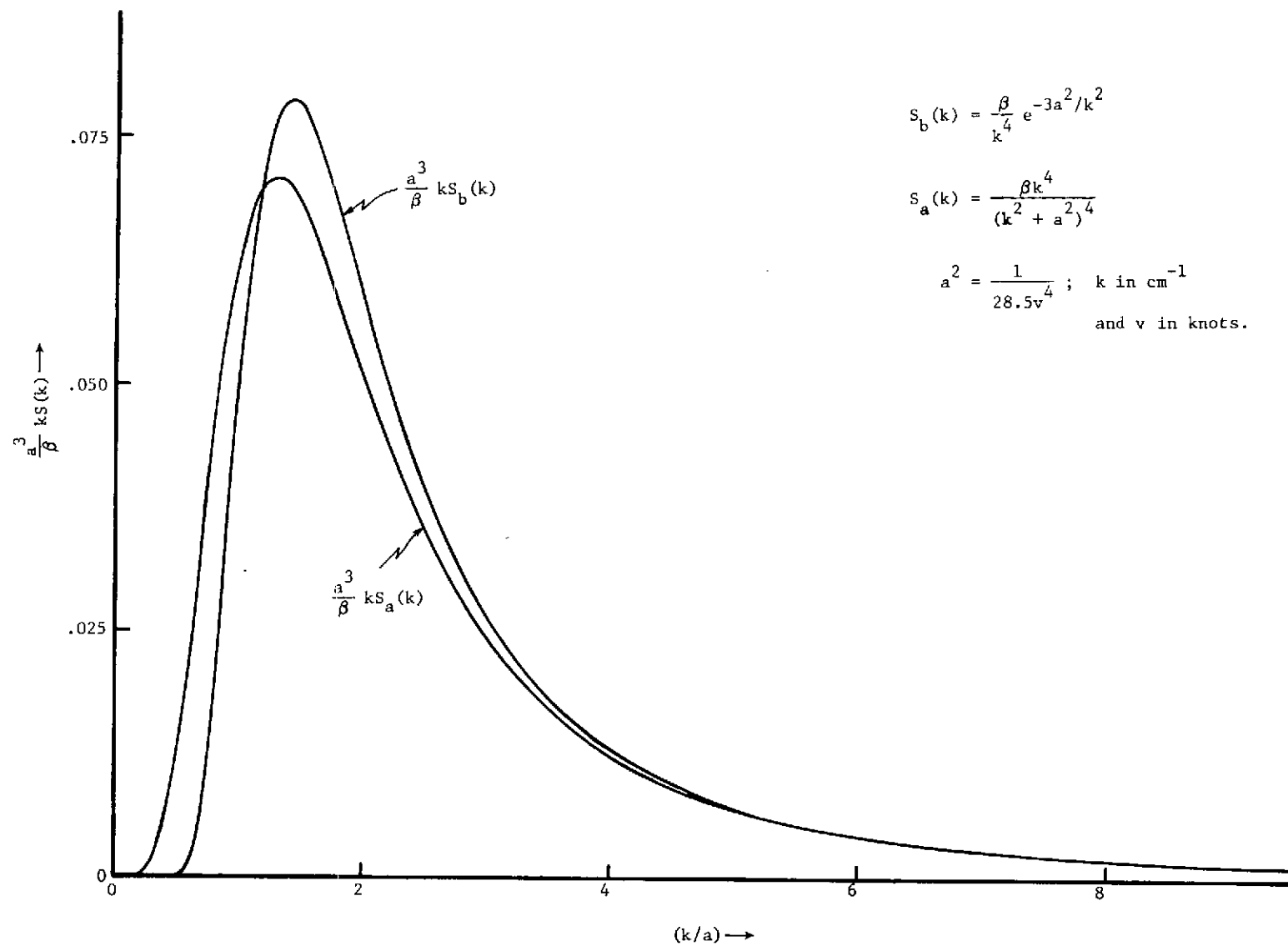
Figure 2. Comparison of the Pierson-Moskowitz spectrum S(k) with the approximate spectrum.

The two-dimensional surface height correlation function $\rho(r,\phi)$ and the surface height wavenumber spectrum $S(k,\Psi)$ are a Fourier-Bessel transform pair:

$$\rho(r,\phi) = \frac{1}{2\pi} \int_0^\infty \int_0^{2\pi} \Psi(k,\psi) e^{jkr\cos(\psi-\phi)} k\,dk\,d\psi$$

$$\Psi(k,\psi) = \frac{1}{2\pi} \int_0^\infty \int_0^{2\pi} \rho(r,\phi) e^{-jkr\cos(\psi-\phi)} r\,dr\,d\phi \quad .$$

(3)

The mean-square wave height is given by $\rho(o,\phi)$ and the normalized surface height correlation function $\rho_n(r,\phi)$ is $\rho(r,\phi)/\rho(o,\phi)$.

For near-normal incidence, the electric currents giving rise to the scattered fields are assumed to be the zero order physical optics currents induced on the scattering surface. Under this assumption and that of a Gaussian surface height distribution, the average monostatic cross section per unit area of scattering surface (σ^o) is given by [7].

$$\sigma^o(\theta) \approx \frac{\kappa^2 |Q_o|^2}{2\pi^2 \cos^2\theta} \int_0^{R_o} \int_0^{2\pi} e^{j2\kappa r\cos\phi\sin\theta - 4\kappa^2 h_m^2 \cos^2\theta[1-\rho_n(r,\phi)]} r\,dr\,d\phi \quad (4)$$

In (4), Q_o is the normal incidence reflection coefficient, R_o is much greater than the surface height correlation length, θ is the angle of incidence measured from the normal to the mean surface, $\kappa = \frac{2\pi}{\lambda_{rf}}$ is the rf wavenumber and h_m^2 is the mean-square surface height $\rho(o,\phi)$. It should be noted that the application of physical optics is valid only when the local radius of curvature of the scattering surface and the mean-square surface height are <u>both</u> much larger than the incident rf wavelength.

One of the intents of this effort is to evaluate (4) for the ocean surface whose spectral form is assumed to be approximated by (1). However, because of the presence of high frequency components in the surface's height spectrum, can the physical optics approach be valid? It would certainly

appear that the scattering surface does not everywhere obey the criterion of large local radius of curvature (relative to the rf-wavelength). It is obvious that the physical optics method may not be totally valid here. In fact, this same point was the center of a recent controversy between Fung and Barrick [8] over Fung's use of the physical optics approach to describe composite surface scattering.

It will be shown in this note that for near-normal incidence and the spectral form given by (1) the physical optics approach yields an answer for σ^o which is insensitive to the high frequency part of the surface height spectrum. This fact will be demonstrated by first letting the spectrum in (1) extend to infinity and then truncating the spectrum at some point $k_c < \kappa$; the values of σ^o computed from both of these spectra will be shown to be the same.

3.2 ISOTROPIC INFINITE SPECTRUM RESULTS

For the first case in point, (1) will be assumed to represent the ocean height spectrum throughout the entire wavenumber plane; that is, the spectrum will only be a function of radial wavenumber k and $k_c \to \infty$. The reasons behind the isotropic assumption are the lack of directional spectra data on the ocean's surface and a great simplification in the mathematics. Also, letting (1) hold for $k \in (0, \infty)$ should cause no error if the physical optics formulation is truly insensitive to the small-scale surface structure. Of course, a proof of the last statement is one of the purposes of this study.

Substituting (1) into the transform relation between the spectrum and correlation functions yields

$$\rho(r) = \beta \int_o^\infty J_o(kr) \, \frac{k^5}{(k^2 + a^2)^4} \, dk \tag{5}$$

where $J_o(kr)$ is the Bessel function of the first kind and order zero. When r=0, (5) may be easily integrated to give the mean-square height

$$\rho(o) = h_m^2 = \frac{\beta}{6a^2} \quad .$$

Thus, the normalized height correlation function is

$$\rho_n(r) = 6a^2 \int_o^\infty J_o(kr) \, \frac{k^5}{(k^2 + a^2)^4} \, dk \quad . \tag{6}$$

Using the recurrence relations for Bessel functions to obtain the proper combination of Bessel order and power of k in the numerator of (6) yields three integrals of the Hankel-Nicholson type [9]. The exact evaluation of (6) is;

$$\rho_n(r) = [1 + 1/8(ar)^2](ar)K_1(ar) - (ar)^2 K_o(ar) \tag{7}$$

where K_1 and K_0 are Bessel functions of the second kind of order 1 and 0, respectively. A plot of $\rho_n(ar)$ is shown in Figure 3. It should be noted that $\rho_n(r)$ has no power series expansion about r=o since its second derivation has a logarithmic singularity at r=o. For ar<<1, $\rho_n(r)$ has the following approximate form*

$$\rho_n(r) \approx 1 + 1.5 \ (ar)^2 \log(ar) \quad . \tag{8}$$

Figure 4 illustrates that the approximate and exact forms are in very close agreement even for ar as large as 0.1.

Before discussing the possibility of further simplification of (8), it is desirable to know the required range of the variable r in the σ^o integration. Under the isotropic assumption, the expression for σ^o reduces to the following form

$$\sigma^o(\theta) = \frac{\kappa^2 |Q_o|^2}{\pi \cos^2 \theta} \int_0^{R_o} J_o(2\kappa r \sin\theta) e^{-4\kappa^2 h_m^2 \cos^2\theta [1-\rho_n(r)]} r dr \quad . \tag{9}$$

A plot of the integrand in (9) is shown in Figure 5 for $\theta = 0^o$ and Figure 6 for $\theta = 30^o$. For $v \geq 3.6$ knots, these figures show that the integrand is essentially zero for $r \geq 20$ centimeters. Using $\rho_n(r)$ from equation (7) and accomplishing the integration in (9) by numerical means results in the solid-line curves of $\sigma^o(\theta)$ versus wind speed as shown in Figure 7. These plots clearly illustrate the insensitivity of σ^o to changes in wind speed.

Previous analytical efforts [10, 8, 11, 12] have provided approximate expressions for σ^o based on certain assumptions about the correlation function. The one assumption common to many of these investigations was that the correlation function could be represented by a power series in a neighborhood of the origin [13]. Unfortunately, such a series does not exist for the correlation function in equation (7) because the function is not analytic at r = o, and, therefore, the approximate expressions for σ^o have no meaning for this particular example. However, some simplification of the correlation

---

*All logarithms in this chapter will be to the base e unless otherwise noted.
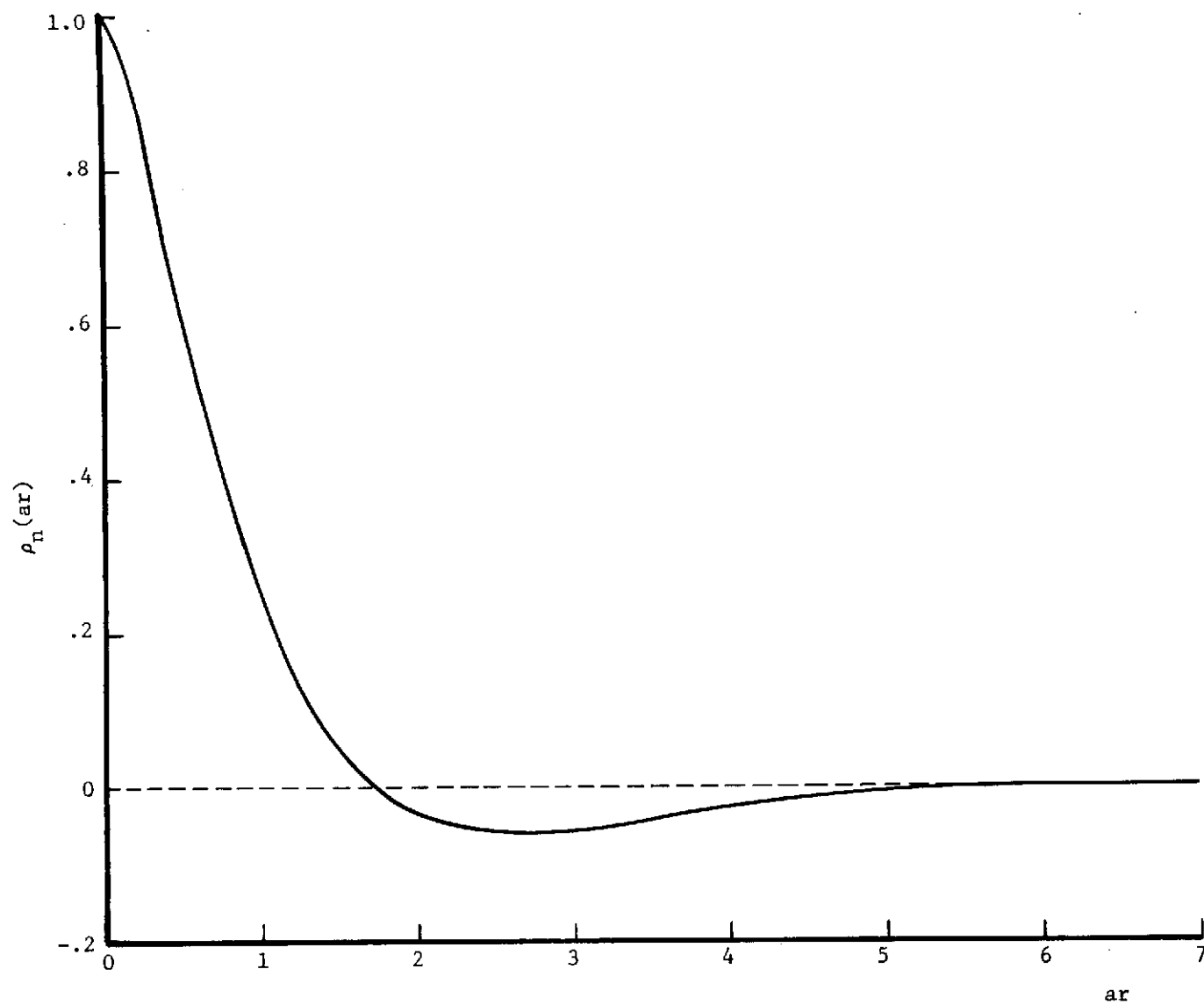
Figure 3. The normalized autocorrelation function for the assumed isotropic spectrum $S_a(k)$, $(a^2 = 1/28.5v^4)$.
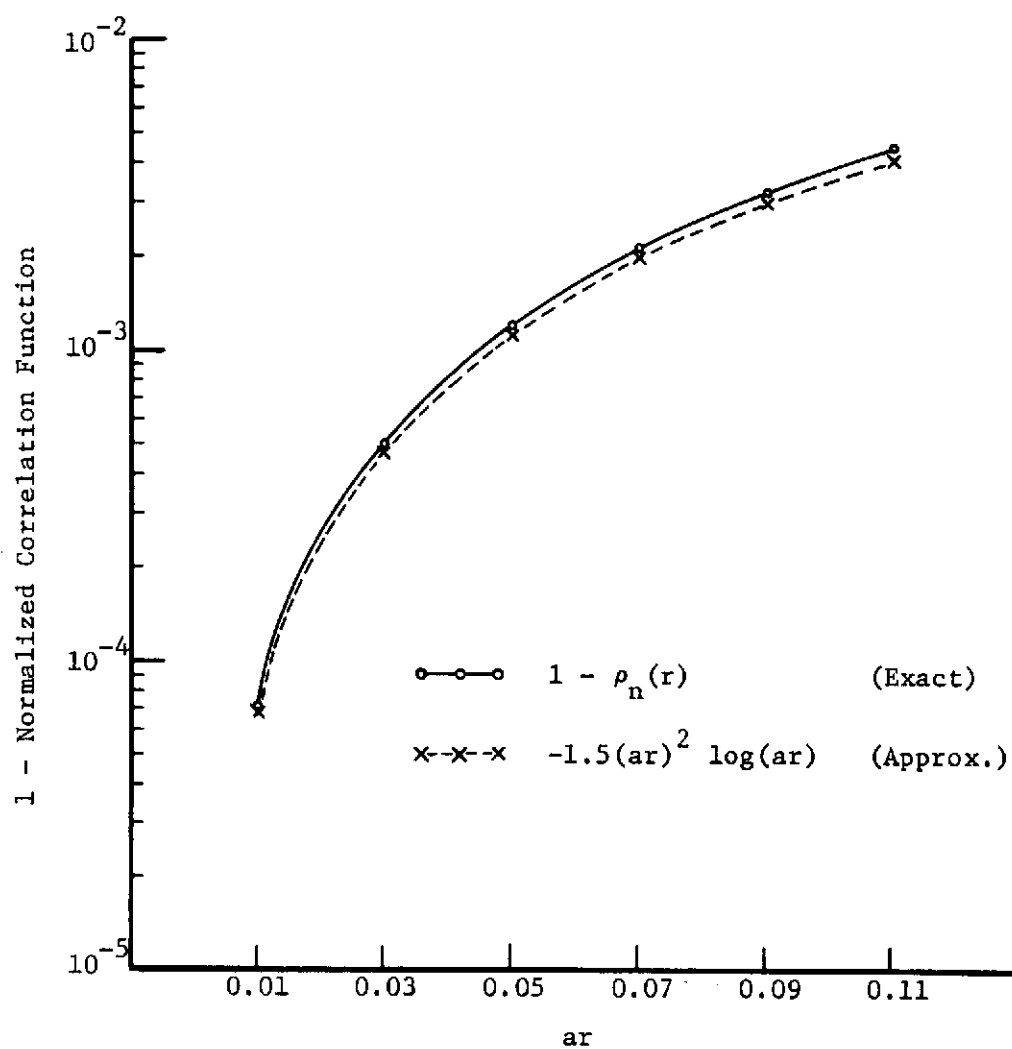
Figure 4. A comparison of the exact and approximate formulas for the isotropic normalized correlation function $(a^2 = 1/28.5v^4)$.
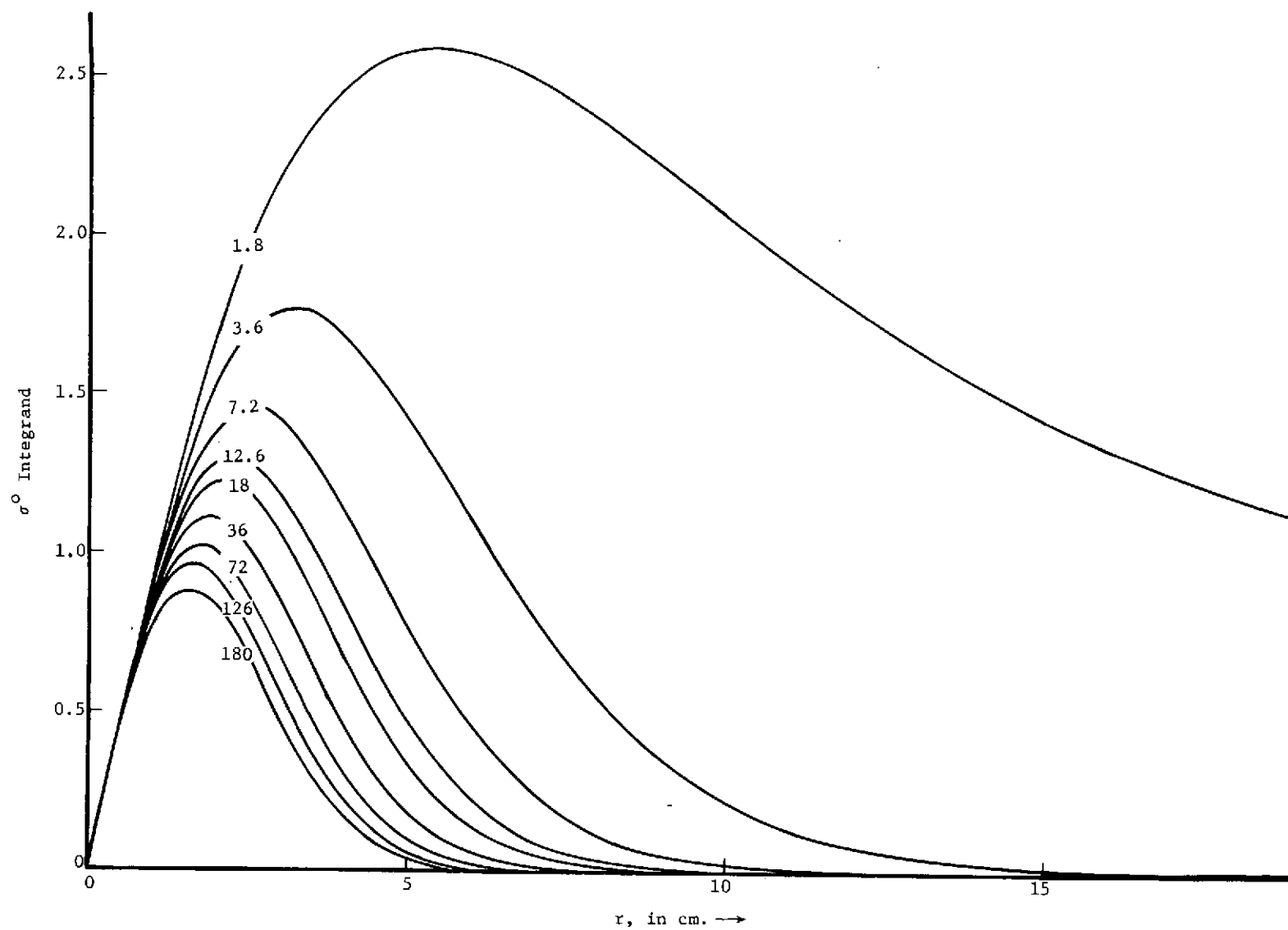
Figure 5. σ^0 integrand for $\theta = 0^\circ$; isotropic spectrum and v ranging from 1.8 to 180 knots with λ_{rf} = 3 cm.
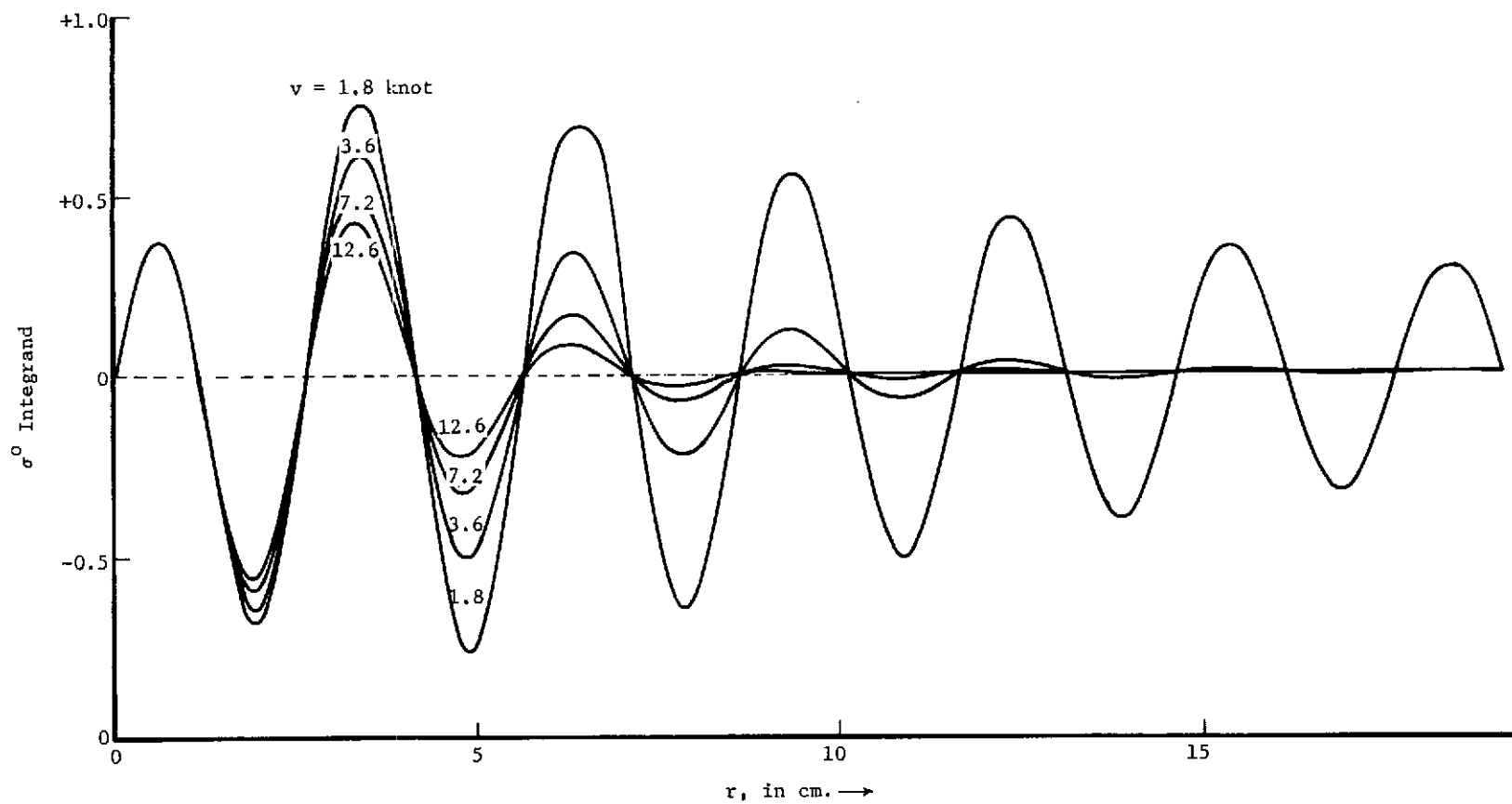
Figure 6. σ° integrand for $\theta = 30^{\circ}$; isotropic spectrum and v ranging from 1.8 to 12.6 knots with $\lambda_{rf} = 3$ cm.

function (due to the small numerical value of the parameter a) can be accomplished. In particular, $(ar)^2 \log(ar)$ in (8) can be reduced to $(ar)^2 \log(a)$ for v greater than about 3 knots and then

$$\rho_n(r) \approx 1 + 1.5 \ (ar)^2 \ \log(a) \quad . \tag{10}$$

The reasoning behind the simplification from (8) to (10) is as follows. The difference between (8) and (10) is significant only when r is on the order of or less than the parameter a. However, since $a = 1/(5.3v^2)$ is very small, the difference betwen (8) and (10) is only appreciable for r<<1. When r<<1, the integrand in (9) is dominated by the linear r term and hence the resulting effect on the σ^o integral in (9) is negligible. The approximate expression for $\rho_n(r)$ in (10) may also be justified by noting that as r → o

$$(ar^2)\log(ar) \rightarrow -\ 1/2(ar)^2 + (ar)^2\log(a) \approx (ar)^2\log(a),$$

where L'Hospital's rule has been applied to $(ar)^2\log(r)$ to determine its limiting form as r → o.

When (10) was used in (9) and the integration accomplished numerically, the resulting values of σ^o differed by only 0.1 to 0.2 dB from σ^o computed using the exact expression for $\rho_n(r)$. Following the reasoning of [7], if R_o is taken to be infinite, then (9) may be integrated in closed form when (10) is taken to be the correlation function. The resultant expression for $\sigma^o(\theta)$ is

$$\sigma^o(\theta) = \frac{|Q_o|^2}{2\pi\cos^4\theta} \ \frac{\exp\left[-\ \frac{\tan^2\theta}{\beta\log(1/a)}\right]}{\beta\log(1/a)} \quad . \tag{10a}$$

The closed form results are shown as dashed lines in Figure 7. A comparison of the closed form curves with the numerical integration results, both using (10) for the correlation function, shows that the closed form approximation
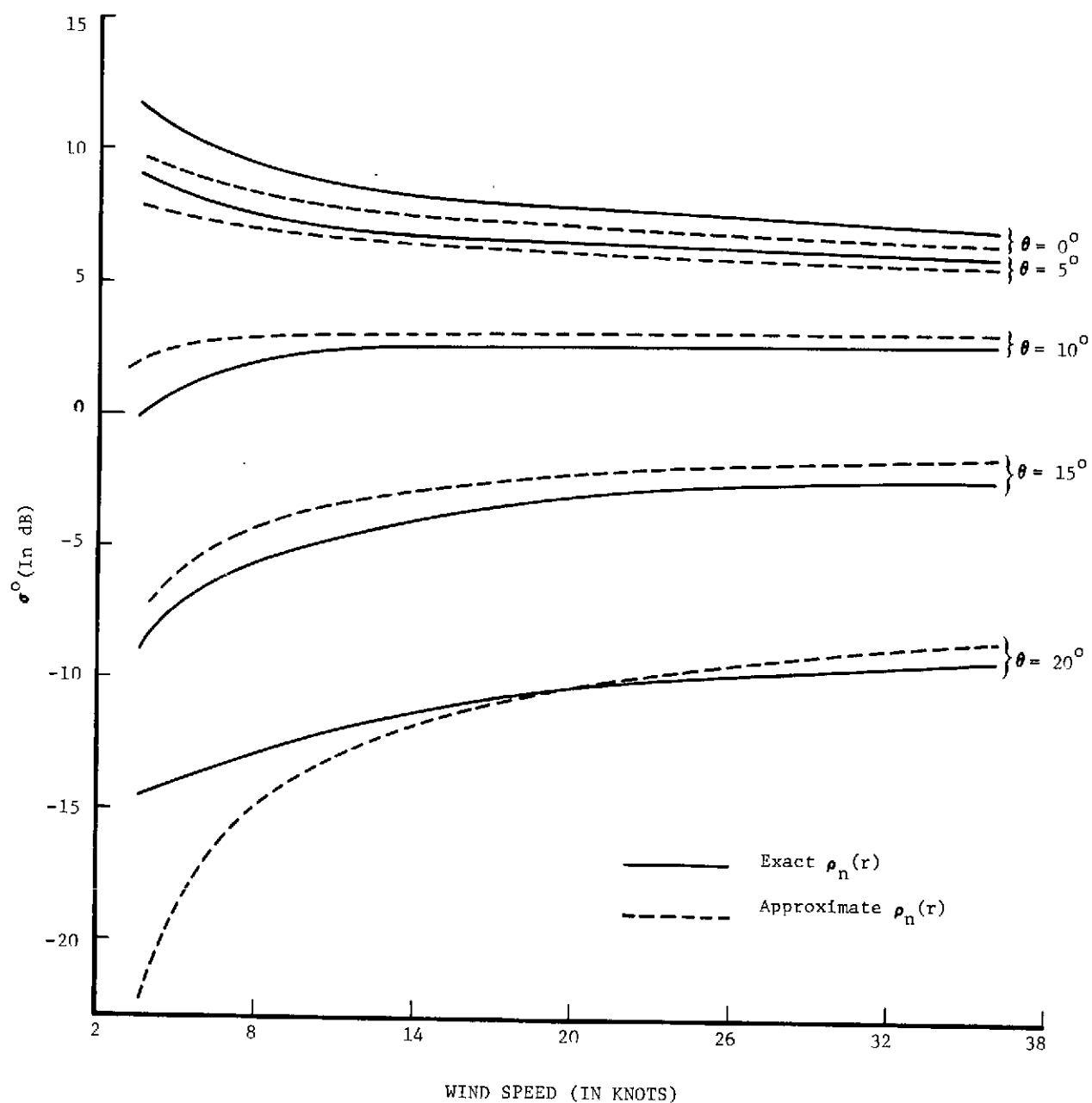
Figure 7. A comparison of the scattering cross-sections resulting from approximate
and exact correlation functions. (λ = 3 cm, $|Q_0|^2$ = 1)

is significantly in error only for small wind speeds.

Figure 8a is a graph of σ^o versus angle and Figure 8b shows σ^o versus wind speed. One of the objectives of this section is to determine if the physical optics theory, when used in conjunction with a physically plausible autocorrelation function rather than one chosen on grounds of mathematical tractability, demonstrates any drastic changes in σ^o for small angular displacements near normal incidence. Such behavior which has been speculated on numerous occasions [20], would be of considerable theoretical and engineering interest to the GEOS-C and related programs. Note that measurements to investigate σ^o very close to normal incidence also pose one of the more difficult experimental geometries for an aircraft test program since high altitudes and narrow antenna beam widths would both be required to satisfy angular resolution and illuminated area considerations. According to Figure 8a, drastic changes in σ^o near $\theta = 0^o$ are not in evidence in this theoretical result – experimental confirmation from Skylab will be awaited with considerable interest. The second factor to be discussed in connection with Figure 8a is the angular dependence encountered. Note that this dependence is minimized at a particular angle (~9 degrees); a result that is in accord with the scatterometer concept of comparing returns at a particular angle with returns at large angles rather than requiring the scatterometer to measure absolute value. That is, it is much easier to compare σ^o values at, say, 10 and 40 degrees than to require absolute σ^o measurements. The results shown in Figure 8a offer further evidence that such a scheme is feasible. The third factor to be noted in Figure 8a is the degree to which σ^o decreases with increasing angles off of normal. We show σ^o decreasing more rapidly with angle than does the only comparable study [19]. In this reference, the numerical nature of the work makes any identification of the physical reasons for the disparity with our results extremely difficult. Lastly, Figure 8a indicates that the approach of relating normal incidence σ^o to surface winds (as suggested on GEOS-C satellite) will be of limited value – the figure shows that a variation in wind conditions of 5 to 38 knots produces a maximum variation of 6dB in σ^o. Thus the results indicate that only gross changes in wind conditions could be resolved, even under equilibrium conditions.
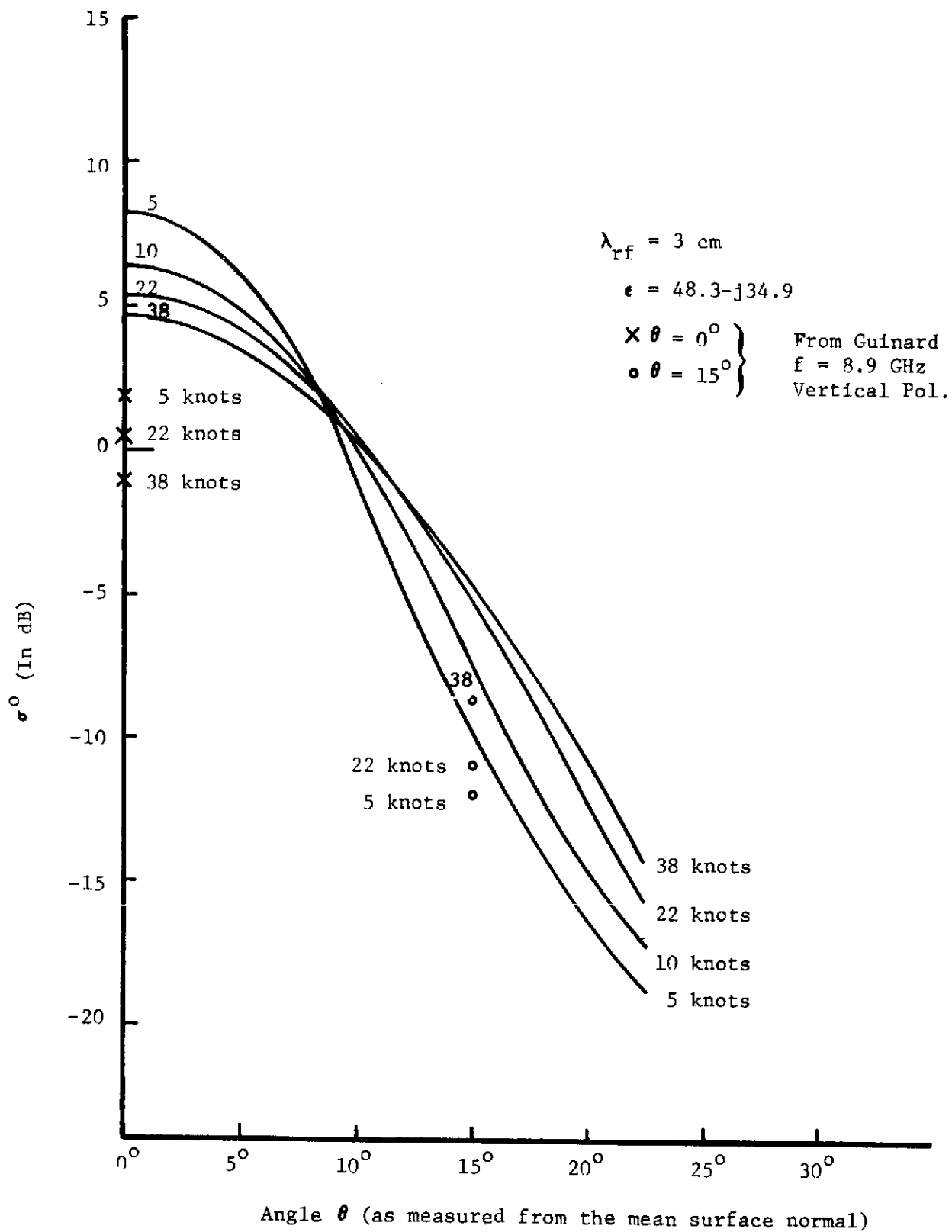
Figure 8a. Scattering cross-section as a function of angle and wind speed.

Figure 8b shows the saturation effect discussed by Guinard [14] to be strongly in evidence in these near-normal incidence results. For an angle-of-incidence of 15 degrees, over a wind speed range of 15 to 35 knots, σ^o is shown to vary by only 1.5 db. The curves shown in Figure 8b contain an obvious level shift between the computed and experimental values. We attach more significance to the relative than to the absolute values given because of the uncertainty and reported variability of the numerical constants involved in the absolute computation (i.e.,dielectric constant, spectral factor β, atmospheric attenuation, and so forth). Both comparisons are subject to the caveat that Guinard's ocean conditions are assumed to be representable as swell-free, non-fetch-limited, equilibrium conditions.

The above discussion points up the need for rather extensive ground truth data in any attempt to correlate measured and computed σ^o data. So far, we are unable to place bounds on the ocean spectral description needed - this is investigated in the next section. It is recognized that the long wavelength end of the spectrum is only poorly known. Schule [21] gives data which shows that the effect of limited fetch results in non unimodal behavior in the long wavelength range. It is conceivable that fetch restrictions or swell components could cause the σ^o versus wind speed relationship to inherently lead to sizable data spread if these effects are neglected. With appropriately measured spectra and other ground truths parameters, perhaps the long standing σ^o controversy can be resolved. Ocean surface wavenumber spectral measurements are extremely difficult and costly to obtain over any sizable wavenumber range. The objective of the remainder of this study is to derive theoretical guidelines relative to the k-number range and the angular variation one should attempt to obtain in spectral measurements.

The primary reason for considering the infinite spectrum case is to provide a basis for studying the effects of spectral truncation. The infinite spectrum has, however, led to a very interesting correlation function having the following properties:

a) $\rho_n(r)$ is asymptotically parabolic as $r \rightarrow o$, but not over a sufficient range to allow accurate asymptotic integration of the σ^o integral,

b) $\rho_n(r)$ is not of Gaussian or any of the forms prevalent in the literature, and
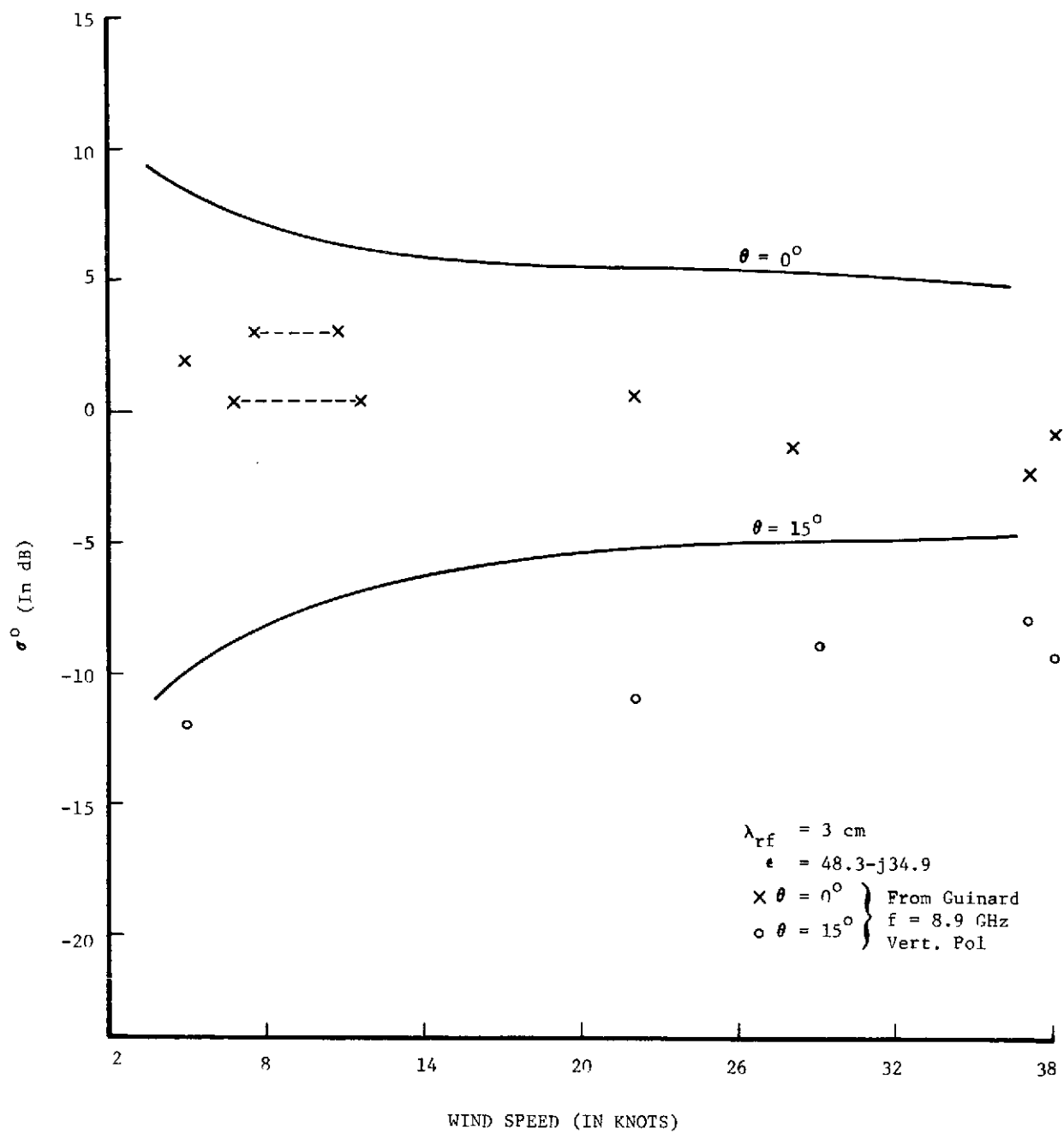
Figure 8b. Comparison of theoretical and measured scattering cross-sections as a function of wind speed for θ = 0 and 15 degrees.

c) $\rho_n(r)$ does not have a power series representation as $r \to o$, i.e., it
    is not analytic at $r = o$*.

For this correlation function, it is quite easy to verify that conventional [8, 10, 11, 12] approximate or asymptotic technique for evaluating the scattering integral in (9) fail. While $\rho_n(r)$ is derived from a particular surface height spectrum, the important point to note is that approximations to (9) do have distinct limitations and interpretation of backscattering results in terms of ad hoc forms for $\rho_n(r)$ should be accomplished with great care.

---

*We have avoided discussion of the fact that the mean-square surface slope is infinite for the correlation function in (7) since this is "a symptom of deeper problems inherent in the model" [13]. An effective slope (which remains finite as $r \to o$) may be deduced from (10), but it is somewhat different from that originally discussed by Hagfors [11]. That is, the mean-square slope deriving from (10) is not equivalent to the mean-square slope resulting from a truncated spectrum, as will be shown in the next section.

3.3 SPECTRAL TRUNCATION EFFECTS

In order to show that near-normal incidence scattering is insensitive to the high wavenumber portion of the ocean height spectrum, it will be necessary to investigate the effects of <u>truncating</u> the ocean height spectrum. The truncation results will indicate where sea-truth data can be neglected with no appreciable effect upon the correlation of σ^o measurements and theory. If the isotropic spectrum in (1) is truncated at some point $k=k_c$, i.e.,

$$S(k) = \begin{cases} \dfrac{\beta k^4}{(k^2 + a^2)^4} & k \leq k_c \\[4mm] 0 & k > k_c \end{cases}$$

the correlation function becomes $\tilde{\rho}(r)$, where

$$\tilde{\rho}(r) = \int_0^{k_c} \frac{\beta k^5}{(k^2 + a^2)^4} \, J_0(kr) \, dk \quad . \tag{11}$$

Expanding the Bessel function in a power series about $r=0$, integrating the first three terms and rearranging yields

$$\tilde{\rho}(r) = \frac{\beta}{2} \sum_{m=0}^{2} \frac{(-1/4r^2)^m}{m! \, \Gamma(m+1)} b_m + \frac{\beta}{2} \sum_{m=2}^{\infty} \frac{(-1/4r^2)^m}{m! \Gamma(m+1)} \int_0^{k_c^2} \frac{\tau^{m+2}}{(\tau + a^2)^4} \, d\tau \tag{12}$$

where,

$$b_o = \frac{1}{3a^2} - \frac{1}{\delta} + \frac{a^2}{\delta^2} - \frac{a^4}{3\delta^3}$$

$$b_1 = -\frac{11}{6} - 2\log(a) + \frac{3a^2}{\delta} - \frac{3a^4}{2\delta^2} + \frac{a^6}{3\delta^3} + \log(\delta)$$

$$b_2 = \frac{10}{3}a^2 + 8a^2 \log(a) - 4a^2 \log(\delta) - \frac{6a^4}{\delta} + \frac{2a^6}{\delta^2} - \frac{a^8}{3\delta^3}$$

and $\delta = (k_c^2 + a^2)$. When $k_c r \ll 1$, the finite series in (12) is sufficient for numerical purposes. The integration in (12) results in the following.

$$\int_0^{k_c^2} \frac{\tau^{m+2}}{(\tau+a^2)^4} \, d\tau = \begin{cases} k_c^2 + 0(a^2) & m = 2 \\ \dfrac{k_c^{2m-2}}{(m-1)} + 0(4a^2 \dfrac{k_c^{2m-4}}{m-2}) & m > 2 \end{cases}$$

Thus, for $k_c^2/a^2 \gg 9$,

$$\int_0^{k_c^2} \frac{\tau^{m+2}}{(\tau+a^2)^4} \, d\tau \approx \begin{cases} k_c^2 & m = 2 \\ \dfrac{k_c^{2m-2}}{(m-1)} & m > 2 \end{cases}$$

and the correlation function becomes

$$\tilde{\rho}(r) \approx \frac{\beta}{2} \sum_{m=0}^{2} \frac{(-1/4r^2)b_m}{m!\,\Gamma(m+1)} + \beta \sum_{m=2}^{\infty} \frac{(-1/4r^2)^m k_c^{2m-2}}{m!\,\Gamma(m+1)(2m-2)} \qquad . \quad (13)$$

When $k_c r$ is much larger than five, the infinite series in (13) is difficult to numerically sum because of the magnitude and oscillatory behavior of the individual terms. To overcome this difficulty, the infinite sum may be replaced by its equivalent, i.e.,

$$\sum_{m=2}^{\infty} \frac{(-1/4r^2)^m k_c^{2m-2}}{m!\,\Gamma(m+1)(2m-2)} = r^2 \int_0^{k_c r} \left\{ \frac{J_0(\tau)-1+1/4\tau^2}{\tau^3} \right\} d\tau \qquad . \quad (14)$$

3-23

Integration by parts leads to

$$\sum_{m=2}^{\infty} \frac{(-1/4r^2)k_c^{2m-2}}{m!\,\Gamma(m+1)(2m-2)} = \frac{r^2}{2}\left\{ \frac{1-J_o(k_c r) + \left[\frac{k_c r}{2}\right] J_1(k_c r)}{(k_c r)^2} - 1/2 \right\}$$

$$+ \frac{r^2}{4}\left\{ \gamma + \log\left[\frac{k_c r}{2}\right] + \int_{k_c r}^{\infty} \frac{J_o(\tau)}{\tau}\, d\tau \right\}$$

where γ is Euler's constant, and for $k_c r \geq 5$

$$\int_{k_c r}^{\infty} \frac{J_o(\tau)}{\tau}\, d\tau \approx \frac{2g_1(k_c r)J_o(k_c r)}{(k_c r)^2} - \frac{g_o(k_c r)J_1(k_c r)}{(k_c r)} \quad .$$

The g-functions are a series in inverse powers of $k_c r$ and are explicitly given by Reference [9], Page 482. Combining all of the preceding results leads to the following equation for the correlation function:

$$\tilde{\rho}(r) = \frac{\beta}{2} \sum_{m=0}^{2} \frac{(-1/4r^2)^m b_m}{(m!)^2} + \beta \Phi(k_c r) \tag{15}$$

where for $k_c r \ll 1$

$$\Phi(k_c r) \approx 0$$

and for $k_c r < 5$ and $k_c^2 \gg 9a^2$,

$$\Phi(k_c r) \approx \frac{1}{k_c^2} \sum_{m=2}^{\infty} \frac{(-1/4r^2 k_c^2)^m}{(m!)^2(2m-2)}$$

and finally for $k_c r \geq 5$ and $k_c^2 >> 9a^2$,

$$\Phi(k_c r) \approx \frac{r^2}{2} \left[\frac{1 - J_o(k_c r) - \left[\frac{k_c r}{2}\right] J_1(k_c r)}{(k_c r)^2} + \left(\frac{\gamma-1}{2}\right) + \frac{1}{2} \log\left[\frac{k_c r}{2}\right] \right]$$

$$+ \frac{r^2}{4} \left[\frac{2 g_1(k_c r) J_o(k_c r)}{(k_c r)^2} - \frac{g_o(k_c r) J_1(k_c r)}{(k_c r)} \right] \quad .$$

The mean-square wave height for the truncated spectrum is $1/2 \, \beta b_o$, which is approximately equal to $\beta/6a^2$. Therefore, the normalized height correlation function is

$$\tilde{\rho}_n(r) = \frac{1}{b_o} \sum_{m=o}^{2} \frac{(-1/4r^2)^m b_m}{(m!)^2} + \frac{2}{b_o} \quad \Phi(k_c r) \quad . \tag{16}$$

For this case, it is obvious that the correlation function is parabolic in the neighborhood of the origin, and, in fact, for $ar << 1$ and k_c fixed

$$\tilde{\rho}_n(r) \approx 1 + 1.5 \, (ar)^2 \log(a) \quad . \tag{17}$$

Comparing equations (17) and (10), it is easily seen that the finite and infinite spectrum correlation functions are very similar in the region of significance to the σ^o problem.

Equation (16) is useful because it permits an assessment of the effect of high or low wavenumber spectral truncation. From a practical standpoint, if the instrument measuring the ocean height spectrum only responds to wavenumbers in the range from k_ℓ to k_c (Figure 9), it is desirable to know how the resulting computed value of σ^o will behave as a function of wind speed. In this study, both low and high wavenumber truncation effects were investigated and the results are shown in Figure 10 for normal incidence. It was

Wave Height
Spectrum
S(k)

ACTUAL SPECTRUM

WAVENUMBER k

Wave Height
Spectrum
S(k)
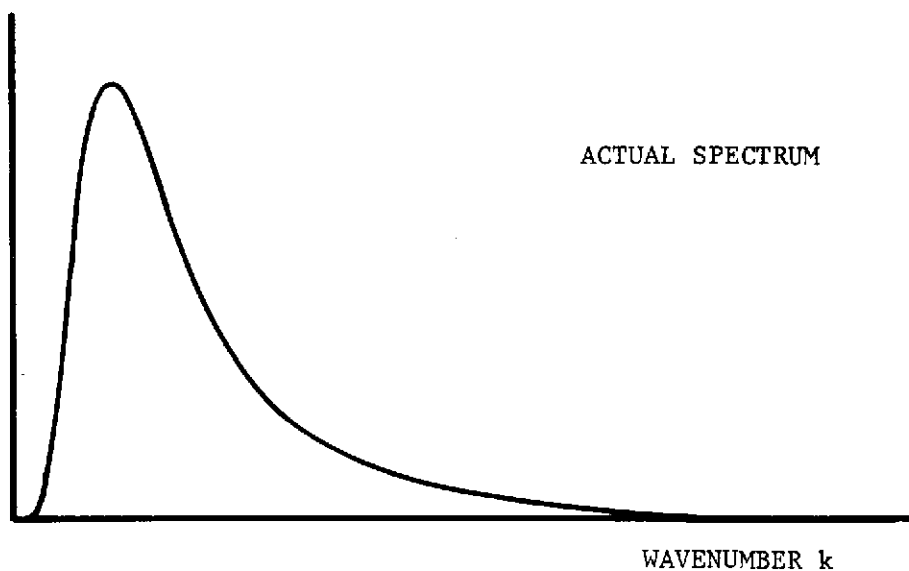
TRUNCATED SPECTRUM

k_ℓ k_c WAVENUMBER k
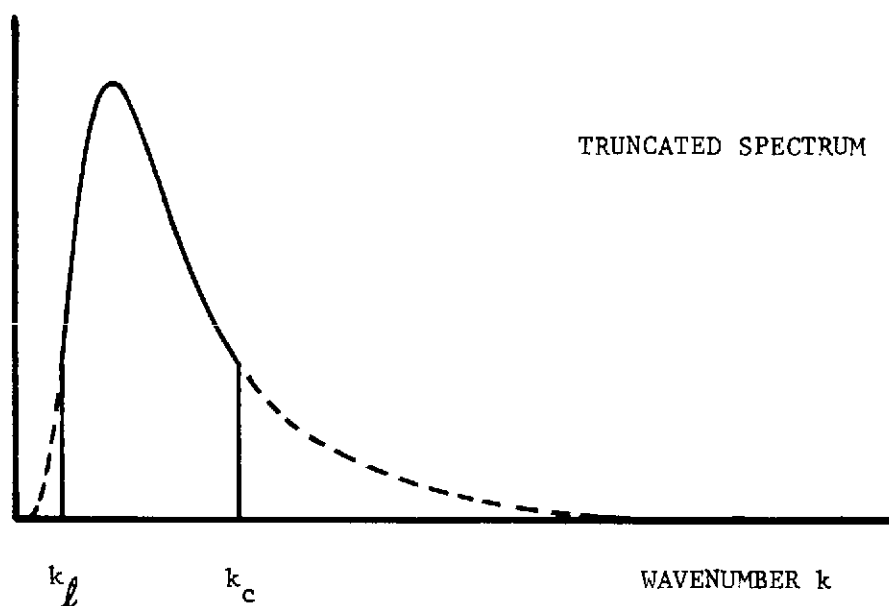
Figure 9. True spectrum and a spectrum with low and high wavenumber truncation ($k_\ell = 0$, $k_c = \infty$ is the true spectrum).
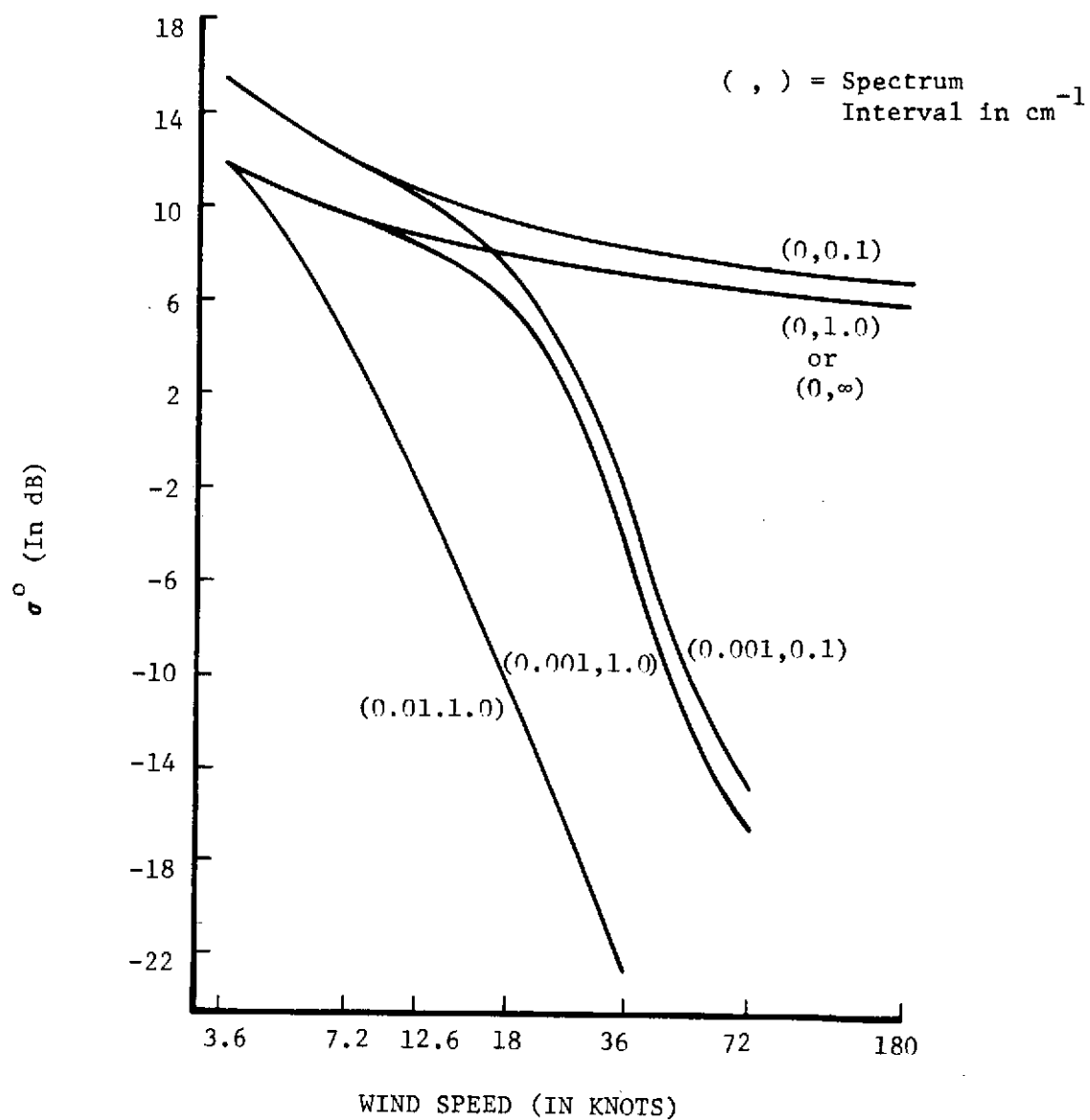
Figure 10. Behavior of σ^o for various upper and lower spectral truncation points; $\lambda_{rf} = 3$ cm, $\theta = 0°$ and $|Q_o|^2 = 1$.

found that the spectrum could be truncated at $k_c = 1.0$ (cm)$^{-1}$ ($\lambda_c = 6.28$ cm) and the resultant values of σ^o were only about 0.1 to 0.2dB different from the infinite spectrum case. Since this value of ocean wavelength is still within the so-called gravity wave range, the original contention of high frequency insensitivity is proven for the Phillip's behavior. If the spectrum is cut off at $k_c = 0.1$ (cm)$^{-1}$ ($\lambda_c = 62.8$ cm), the net effect is an increase in absolute value of σ^o and also a very slight increase in slope for low wind speeds.

In contrast to the relatively small effects of truncation at the high wavenumbers, truncation at the low wavenumber end of the spectrum completely changes the character of the σ^o vs. wind speed curve if the true* mean-square height is used in the integral for σ^o. That is, the spectral truncation is assumed to alter the correlation function but not h_m^2. Such a situation could arise when separate instruments are used to measure spectral characteristics and mean-square height. To understand how the scattering integral behaves as a function of the spectral truncation point, it is necessary to examine $1 - \tilde{\rho}_n(r)$ as a function of r. Figure 11 is such a plot with $k_c = 1$ (cm)$^{-1}$ and as a function of r and wind speed. All of the curves have exactly the same shape with a downward translation being the only effect of increasing the velocity. The other important point to note from Figure 11 is that $[1 - \tilde{\rho}_n(r)]$ decreases almost uniformly with increasing velocity. In Figure 12, the spectrum interval from $10^{-3} - 1$ (cm)$^{-1}$ was taken to represent $\tilde{\rho}_n(r)$. Here it should be noted that $[1 - \tilde{\rho}_n(r)]$ becomes independent of velocity for $v \geq 36$ knots. Since the mean-squared height⊕ continues to increase with velocity, this would imply that the scattering integral for σ^o will exhibit a very rapid roll-off as a function of velocity for greater than 36 knots. Figure 10 clearly shows the mean-square height dominance for lower spectral truncation points of 0.01 (cm)$^{-1}$ and 0.001 (cm)$^{-1}$.

Rather extensive computations were performed to isolate that portion of the spectrum which contributed most to σ^o integration. In these computations,

---

*The true mean-square height as used here is the height which would be obtained by a perfect recording instrument, i.e., no distortion or frequency limitations and no effect on the surface being measured.

⊕The mean-square height employed in these computations was that derived from the spectral range of (0,1) since this would most likely be the actual measured height.
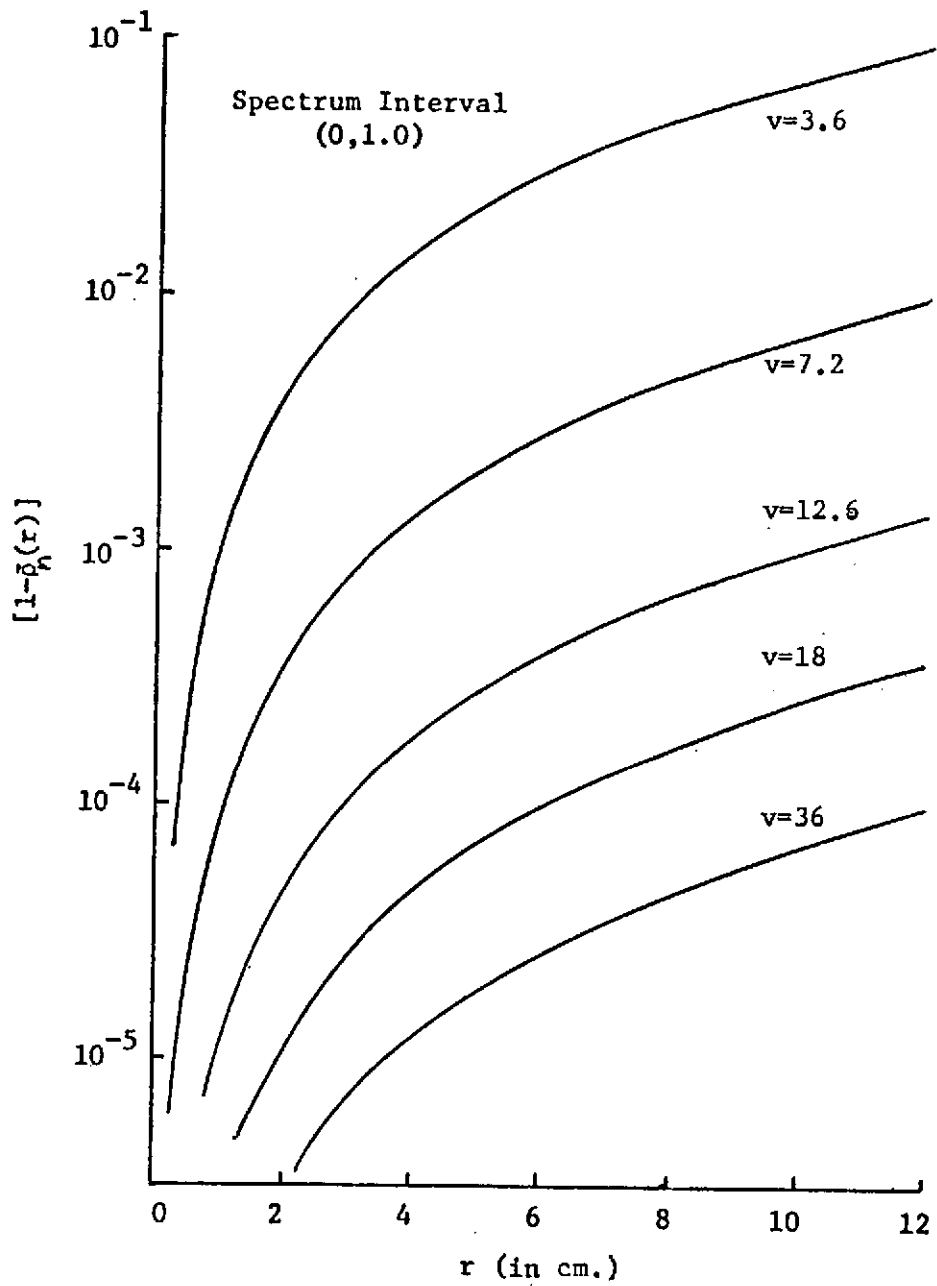
Figure 11. $1-\tilde{\rho}_n(r)$ as a function of r and v when the spectrum interval is $(0,1.0)$, i.e., essentially the same as $(0,\infty)$.
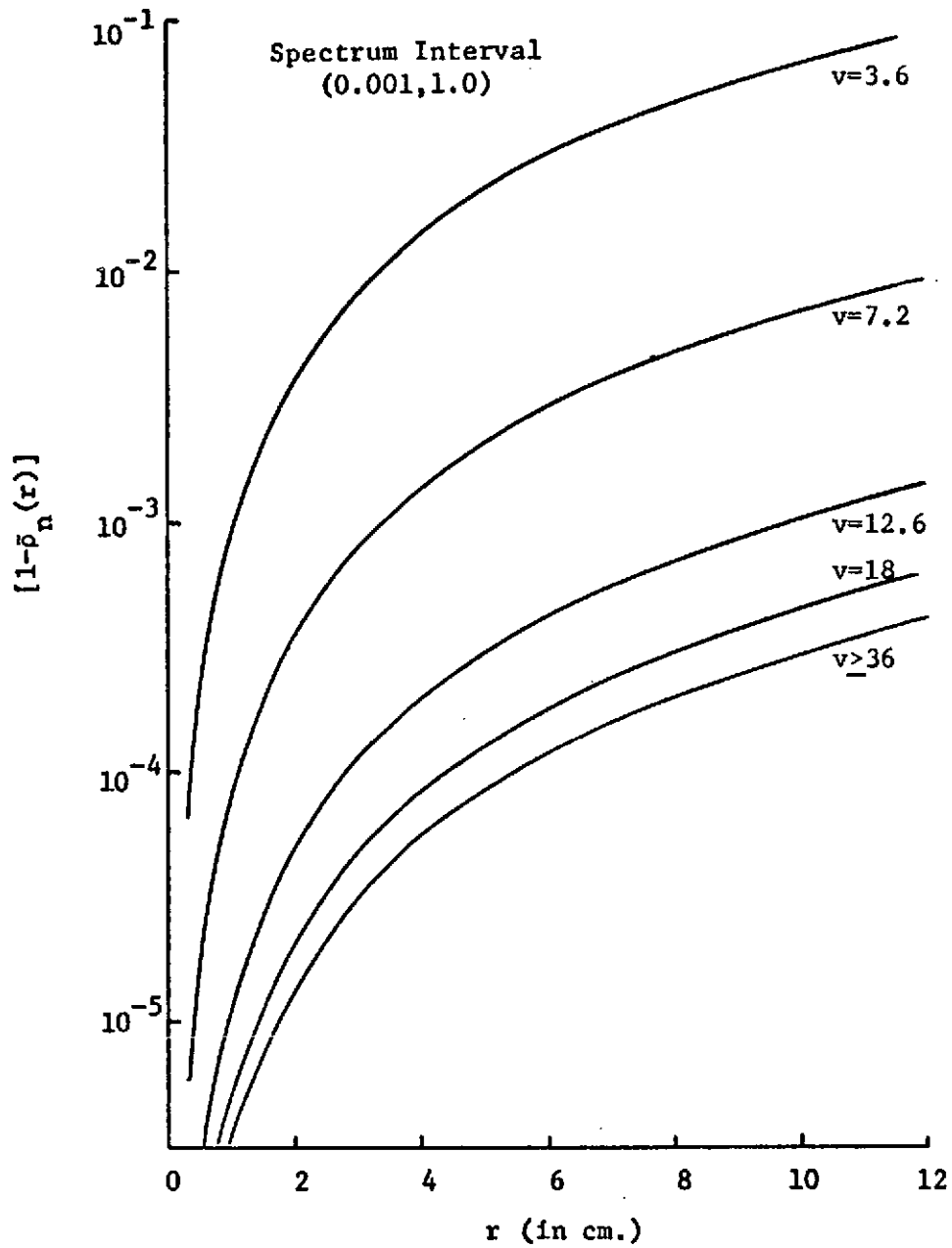
Figure 12. $1-\tilde{\rho}_n(r)$ as a function of r and v when the spectrum interval is $(10^{-3}, 1.0)$.

both the upper and lower spectral truncation points were changed. It was found that if the lower spectral truncation point was set at $k_c = k_{peak}/4$, where k_{peak} was the wavenumber for which the spectrum achieved its maximum, and the upper point was set at 1.0 cm^{-1}, σ^o was essentially the same as with the infinite spectrum. From these calculations, it may be concluded that the backscattering is most sensitive to that portion of the spectrum between $k_{peak}/4$ and approximately one centimeter^{-1}.

Based on a power series expansion of the correlation function about r = o, Barrick [10] and others have interpreted backscattering in terms of the mean-square slope s_m^2 of the surface. That is, for an analytic correlation function at r = o, we will assume that for purposes of the σ^o integration

$$\widetilde{\rho}_n(r) \approx \widetilde{\rho}_n(o) + \frac{1}{2} \left. \frac{\partial^2 \widetilde{\rho}_n}{\partial r^2}\right|_{r = o} r^2$$

then (9) becomes

$$\sigma^o(\theta) \approx \frac{\kappa^2 |Q_o|^2}{\pi \cos^2\theta} \int_o^{R_o} J_o(2\kappa r \sin\theta)\ e^{\left. + 2\kappa^2 \cos^2\theta h_m^2 \frac{\partial^2 \widetilde{\rho}_n}{\partial r^2}\right|_{r = o} r^2}\ r\,dr\ .$$

Defining the mean-square slope s_m^2 as

$$s_m^2 = - 2h_m^2 \left. \frac{\partial^2 \widetilde{\rho}_n}{\partial r^2}\right|_{r = o}$$

and letting $R_o \to \infty$, the expression for $\sigma^o(\theta)$ is integrable, and

$$\sigma^o(\theta) \approx \frac{|Q_o|^2}{2\pi s_m^2 \cos^4\theta}\ \exp\left(- \frac{\tan^2\theta}{s_m^2}\right) \tag{17a}$$

For the infinite spectrum, the mean-square slope is of course infinite. For the truncated spectrum, s_m^2 may be obtained directly from (12), i.e.,

$$s_m^2 = \frac{\beta}{2} b_1$$

or

$$s_m^2 = \frac{\beta}{2} \left\{ -\frac{11}{6} + \log\left[\frac{k_c^2 + a^2}{a^2}\right] + \frac{3a^2}{(k_c^2 + a^2)} - \frac{3a^4}{2(k_c^2 + a^2)^2} + \frac{a^6}{3(k_c^3 + a^2)^3} \right\} .$$

Although the correlation function $\tilde{\rho}_n(r)$ does not change in value* once the spectral truncation point exceeds $1(\text{cm})^{-1}$, it is obvious from the above that s_m^2 increases without bound as $k_c \to \infty$. Figure 13 compares value of $\sigma^o(\theta)$ computed using (17a) and a numerical integration of (9) using $\tilde{\rho}_n(r)$. Whereas the curves for numerical integration of (9) show no variation once $k_c \geq 1.0$, the plots of (17a) continue to change with the greatest change occurring at low wind speeds. We also note that as k_c increases beyond $1(\text{cm})^{-1}$, (17a) yields a $\sigma^o(\theta)$ vs. θ curve which becomes increasingly flat. Thus, compared to a direct computation of $\sigma^o(\theta)$ from $\tilde{\rho}_n(r)$, we see that the mean-square slope approximation is highly sensitive to spectral truncation. This observation is a consequence of the fundamental property that s_m^2 is more sensitive to the high end of the spectrum than $\tilde{\rho}_n(r)$, for r near zero.

The logarithmic dependence of mean-square slope on wind speed agrees favorably with the data obtained by Cox and Munk [6]. That is, for an oil covered sea, their mean-square slope data indicates a logarithmic dependence on wind speed. Since the oil slick should attenuate the high wavenumber components of the surface height spectrum, such a situation is analogous to spectral truncation. For a noncontaminated surface, their data shows a somewhat different dependence upon wind speed; Cox and Munk [6] interpret the curve to be linear while Phillips [1] maintains that the dependence is still logarithmic but with a change in spectral constant β. Further oceanographic analysis and data will be required to resolve this point.

---

*for $r \in (0, R_o)$, or that range of r which influences the $\sigma^o(\theta)$ integrand.
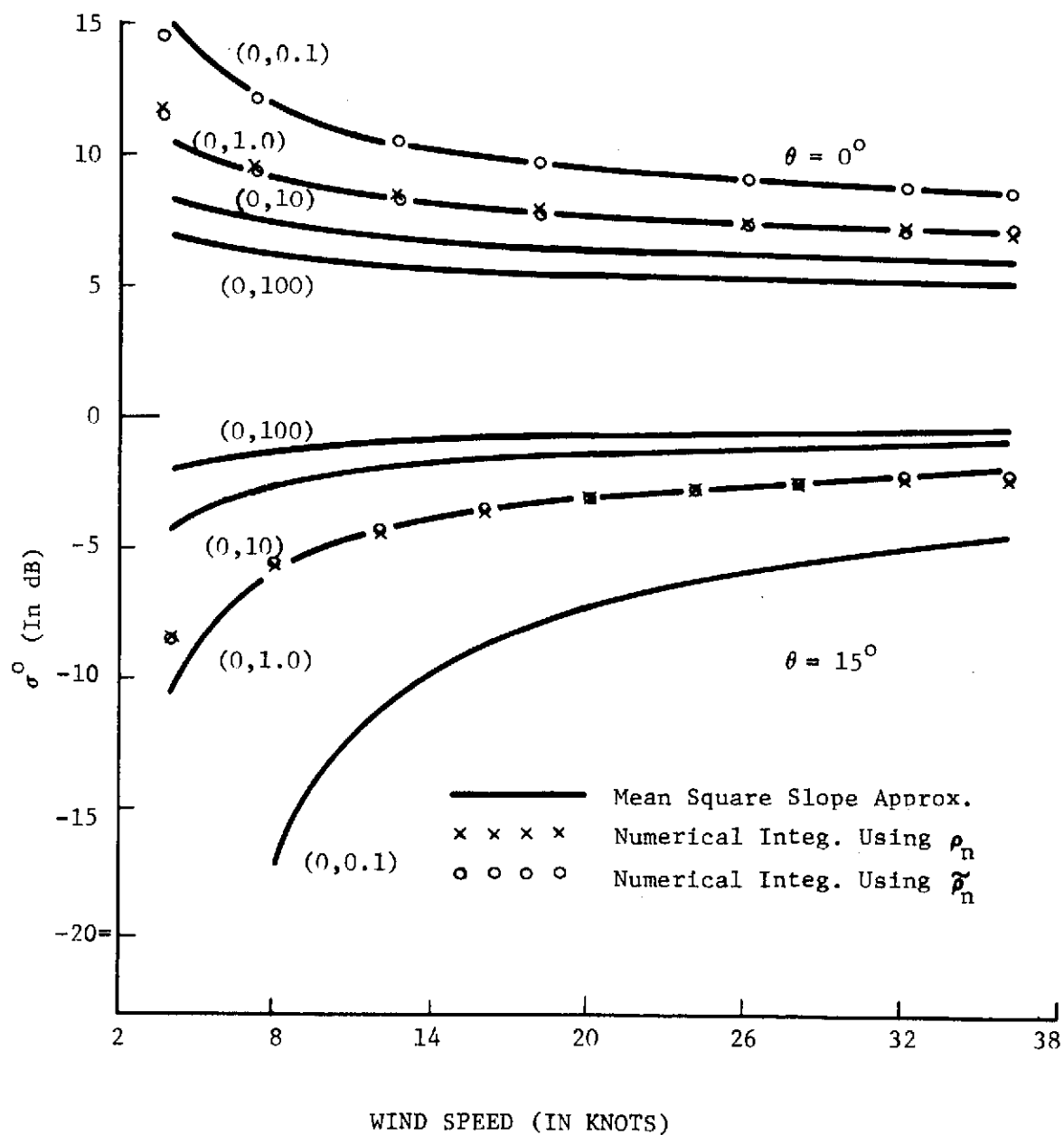
Figure 13. A comparison of the mean-square slope approximation with numerical integration results.

3.4 DIRECTIONAL EFFECTS

To this point only isotropic wavenumber spectra have been considered, but a meaningful analysis must take account of angular variations in the wavenumber power spectrum. Unfortunately, two-dimensional wavenumber spectra are extremely difficult to obtain; two such spectra are available from the work of Cote et al. [15] and of Longuet-Higgins [17], and the σ^o result will be examined for each of these directional spectral forms.

A point of possible confusion arises in connection with the directional spectra and the so-called π(or 180°) ambiguity in the two-dimensional wavenumber spectrum $\Psi(\vec{k})$. Because $\Psi(\vec{k})$ is the Fourier transform of a real surface autocovariance function $\rho(\vec{r})$, the necessary assumption of spatial homogeneity and, hence, the even symmetry of $\rho(\vec{r})$ in $\vec{r}$ leads immediately to $\Psi(\vec{k})$ being even in $\vec{k}$, i.e., $\Psi(\vec{k}) = \Psi(-\vec{k})$ or for $\vec{k}$ in polar form (k,ψ), $\Psi(k,\psi) = \Psi(k,\psi-\pi)$. Conversely, if $\overline{\Psi}$ is a spectrum such that $\overline{\Psi}(k,\psi) \neq \overline{\Psi}(k,\psi-\pi)$ then $\rho(\vec{r})$ found by Fourier transforming this $\overline{\Psi}(k,\psi)$ will have imaginary components and will lead to erroneous results if used in the σ^o integral.

In most oceanographic literature, the ambiguity has been removed by application of additional physical information. That is, a surface-based observer knows which direction the wind is blowing and can remove the ambiguity for at least the longer ocean wavelengths. If the barred $\overline{\Psi}$ denotes the directional spectrum as used in oceanographic literature, the correct spectrum to use in obtaining $\rho(\vec{r})$ for the σ^o problem is as follows:

$$\Psi(k,\psi) = G \ [\overline{\Psi}(k,\psi) + \overline{\Psi}(k,\psi-\pi)] \ .$$

Here, G is a normalization constant to preserve proper mean square height, and $\overline{\Psi}(k,\psi)$ is the "oceangraphers' directional spectrum". The expression is in effect a recipe for putting the π ambiguity back into the problem. Cote et al. [15] have obtained the following approximate directional spectrum expression from stereo photos taken at 18.7 knots;

$$\overline{\Psi}_c(k,\psi) = \begin{cases} 0 & \dfrac{\pi}{2} < \psi < \dfrac{3\pi}{2} \\ \\ S_c(k) \, F(k,\psi) & |\psi| \leq \pi/2 \end{cases} \tag{18}$$

where

$$F(k,\psi) = [1 + (0.5 + 0.82e^{-bk^2}) \cos 2\psi + 0.32e^{-bk^2} \cos 4\psi]$$

The factor b is $3.6(v^4)$ for k in centimeters and v in knots and the wind is assumed to be blowing from the direction of $\psi = 0$. Even though (18) is only approximate for 18.7 knots, for purposes of this study it will be assumed to be valid for all wind speeds.

The two-dimensional spectrum $\Psi_c(k,\psi)$ follows from the previous definition, i.e.,

$$\Psi_c(k,\psi) = S_c(k)[2F(k,\psi)] \ (1/2) \ , \qquad 0 \leq \psi \leq 2\pi \quad .$$

After replacing $S_c(k)$ by $S_a(k)$ and performing the ψ-integration, the two-dimensional height correlation function becomes

$$\rho_n{}^c(r,\phi) = \frac{1}{h_m{}^2} \int_0^\infty \left\{ J_0(kr) - J_2(kr)[0.5 + .82e^{-bk^2}]\cos 2\phi + J_4(kr)(.32)e^{-bk^2}\cos 4\phi \right\}$$
$$\cdot \ S_a(k)kdk \quad . \tag{19}$$

With the following substitutions

$$\rho_0(r) = \frac{1}{h_m{}^2} \int_0^\infty S_a(k)J_0(kr)kdk$$

$$\rho_{21}(r) = \frac{0.5}{h_m{}^2} \int_0^\infty S_a(k)J_2(kr)kdk$$

$$\rho_{22}(r) = \frac{0.82}{h_m{}^2} \int_0^\infty S_a(k)J_2(kr)e^{-bk^2}kdk$$

$$\rho_4(r) = \frac{0.32}{h_m{}^2} \int_0^\infty S_a(k)J_4(kr)e^{-bk^2}kdk$$

equation (19) becomes

$$\rho_n{}^c(r,\phi) = \rho_o(r) - [\rho_{21}(r) + \rho_{22}(r)]\cos 2\phi + \rho_4(r)\cos 4\phi \quad . \tag{20}$$

$\rho_o(r)$ is the correlation function for the isotropic spectrum ($\rho_n(r)$) and
is given by equation (7). The $\rho_{21}(r)$ function may be integrated directly,
i.e.,

$$\rho_{21}(r) = - \frac{(ar)^3}{16} K_1(ar) + \frac{3}{8} (ar)^2 K_o(ar) \quad . \tag{21}$$

The equation for $\rho_{22}(r)$ may be expressed in the following form,

$$\rho_{22}(r) = 2.46 \ a^2 \int_o^\infty J_2(r\sqrt{\tau})e^{-b\tau-4\log(\tau+a^2) + 2\log\tau}d\tau \quad . \tag{22}$$

Due to the additional factor $e^{-b\tau}$, the integrand in (22) converges to zero
before the Bessel function starts to oscillate, even for r relatively large.
Integrals of this type may be evaluated by a slightly modified form of
Laplace's method [16], with the result being

$$\rho_{22}(r) \approx 0.335 \ J_2(\frac{ra}{1.047}) \quad . \tag{23}$$

In a similar fashion, the following is derived for $\rho_4(r)$;

$$\rho_{44}(r) \approx 0.125 \ J_4(\frac{ra}{1.047}) \quad . \tag{24}$$

The various r-dependent components given in equations (20), (21), (23), and
(24) are graphed in Figure 14. This plot indicates that $\rho_4(r)$ can be neglected
in comparison to the other components. Since the integral for σ^o is sensitive
to $[1-\rho_n{}^c(r)]$, Figure 15 shows that the isotropic component, $[1-\rho_o(r)]$, dominates

For 2-Dimensional Cote Spectrum

$$\rho_n^c(r,\phi) \simeq \rho_0(ar) - [\rho_{21}(ar) + \rho_{22}(ar)]\cos 2\phi$$

$$+ \rho_4(ar)\cos 4\phi$$

Correlation Function Components

1.0

0.8

0.6

0.4

0.2

0

0.2

$\rho_0(ar)$

$\rho_{22}(ar)$

$\rho_{21}(ar)$

$\rho_4(ar)$

0.4 0.8 1.2 1.6 2.0 2.4 2.8 3.2 3.6 4 4.4

ar →
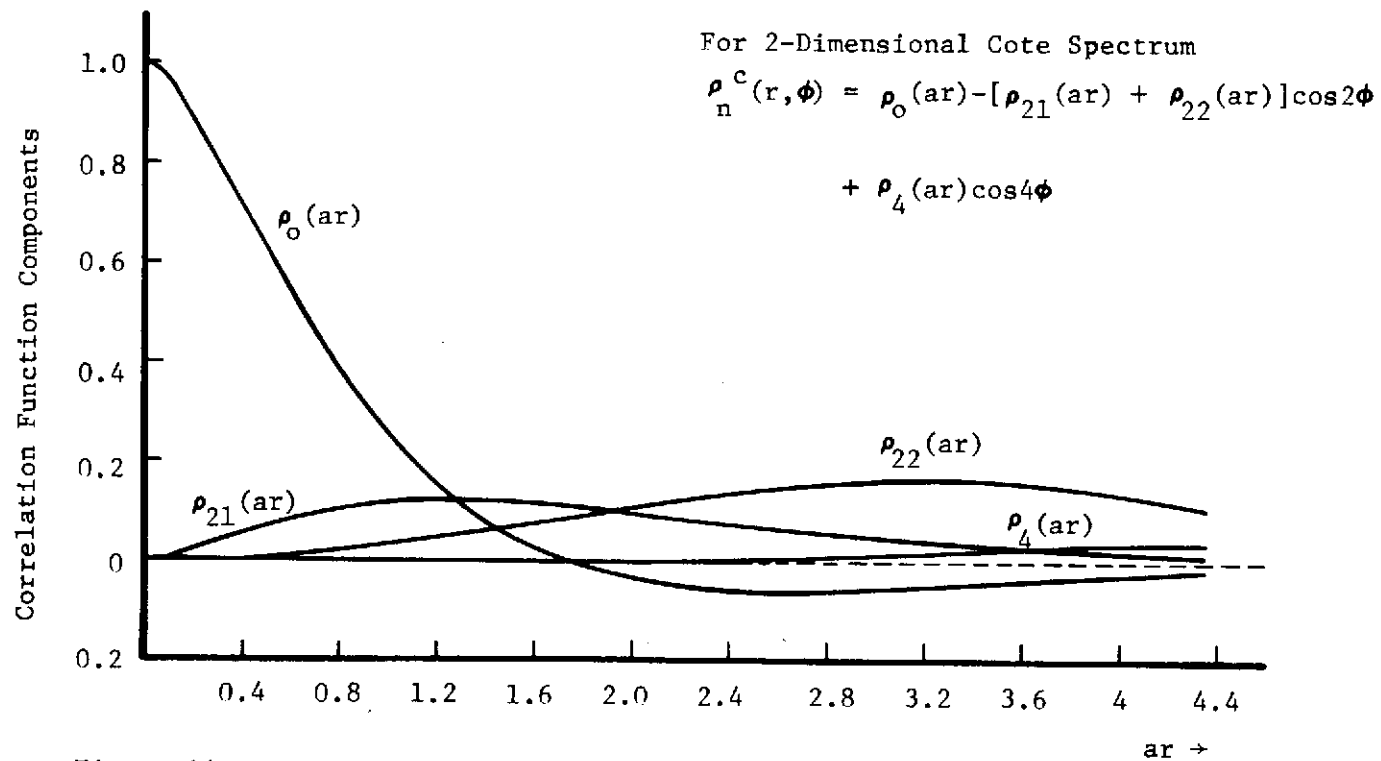
Figure 14. A comparison of the various radially dependent components of the
correlation function for the two-dimensional Cote spectrum.
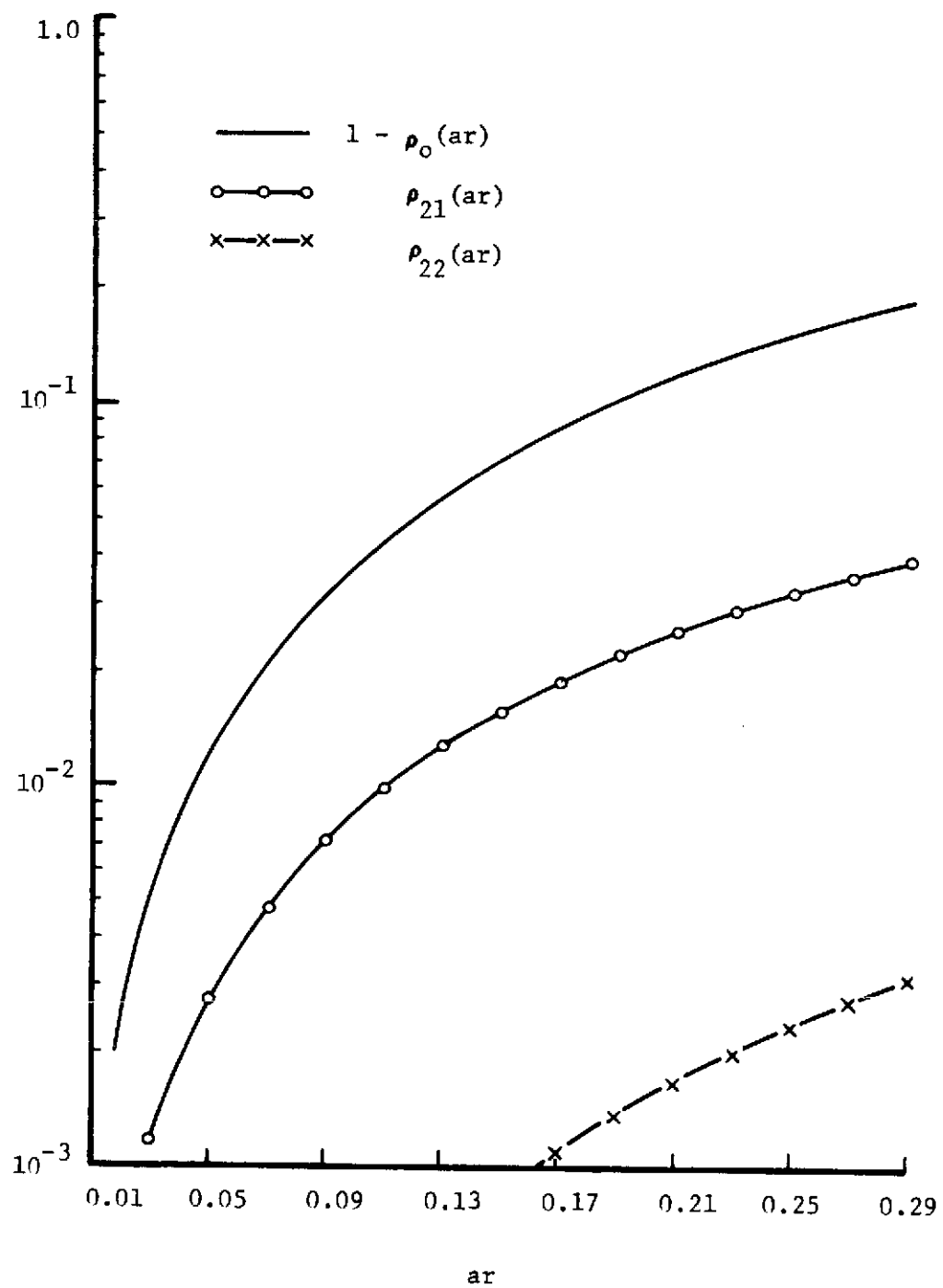
Figure 15. The Cote spectrum correlation function components as they appear in the σ^0 integral ($\phi=0$).

the σ^o integral. Neglecting $\rho_4(r)$, the σ^o integration becomes

$$\sigma^o(0) = \frac{\kappa^2|Q_o|^2}{2\pi^2\cos^2\theta} \int_0^{R_o}\int_0^{2\pi} e^{j2\kappa r\cos\phi\sin\theta}$$

$$\cdot e^{-4\kappa^2 h_m^2 \cos^2\theta}[1-\rho_o + (\rho_{21} + \rho_{22})\cos2\phi]_{rdrd\phi} \quad .$$

Using the following expansion and $\Gamma= 4\kappa^2 h_m^2 \cos^2\theta$,

$$e^{-\Gamma(\rho_{21} + \rho_{22})\cos2\phi} = I_o[\Gamma(\rho_{21} + \rho_{22})] + 2\sum_{n=1}^{\infty}(-1)^n I_n[\Gamma(\rho_{21} + \rho_{22})]\cos(2n\phi) \quad ;$$

the $\sigma^o(\theta)$ integral is

$$\sigma^o(\theta) = \frac{\kappa^2|Q_o|^2}{2\pi^2\cos^2\theta} \int_0^{R_o}\int_0^{2\pi} e^{-\Gamma[1-\rho_o]+j\alpha r\cos\phi}$$

$$\cdot \left\{ I_o\left[\Gamma(\rho_{21} + \rho_{22})\right] + 2\sum_{n=1}^{\infty}(-1)^n I_n[\Gamma(\rho_{21} + \rho_{22})]\cos(2n\phi)\right\}_{rdrd\phi}$$

where $\alpha = 2\kappa\sin\theta$. Accomplishing the ϕ-integration leads to

$$\sigma^o(\theta) = \frac{\kappa^2|Q_o|^2}{\pi\cos^2\theta} \int_0^{R_o} e^{-\Gamma[1-\rho_o]} \left\{I_o(\xi)J_o(\alpha r) + 2\sum_{n=1}^{\infty}I_n(\xi)J_{2n}(\alpha r)\right\} rdr \qquad (25)$$

with $\xi = \Gamma(\rho_{21} + \rho_{22})$. For normal incidence ($\theta=0$), (25) reduces to the following form;

$$\sigma^o(0) = \frac{\kappa^2|Q_o|^2}{\pi} \int_0^{R_o} e^{-4\kappa^2 h_m^2 [1-\rho_o]} I_o\left[4\kappa^2 h_m^2 (\rho_{21} + \rho_{22})\right] rdr \qquad (26)$$

Although the I_o function grows exponentially for large argument, the exponential factor in the integrand of (26) is much more dominant. When the integral in (26) was accomplished numerically, the resultant value of $\sigma^o(0)$ differed by less than 0.2dB from the isotropic case. For $\theta > 0^o$, the infinite sum in (25) is somewhat cumbersome and difficult to treat numerically. However, if the small (ar) approximations are made, i.e.,

$$1 - \rho_o(r) \approx 1.5 \log(\tfrac{1}{a}) \ (ar)^2$$

$$\rho_{21}(r) \approx \tfrac{3}{8} \log(\tfrac{1}{a}) \ (ar)^2$$

$$\rho_{22}(r) \approx .04 \ (ar)^2 \ *$$

and analytic continuation is used to convert $I_n(\xi)$ to $J_n(j\xi)$, i.e.,

$$I_n(\xi) = e^{-j\frac{n\pi}{2}} J_n(j\xi),$$

equation (25) may be expressed as follows

$$\sigma^o(\theta) = \frac{\kappa^2 |Q_o|^2}{\pi \cos^2\theta} \int_0^R e^{-c_1 r^2} \left\{ J_o(c_2 r^2) J_o(\alpha r) + 2 \sum_{n=1}^{\infty} e^{-j\frac{n\pi}{2}} J_n(c_2 r^2) J_{2n}(\alpha r) \right\} r \, dr$$

where

$$c_1 = \kappa^2 \beta \cos^2\theta \log(\tfrac{1}{a})$$

$$c_2 = j\tfrac{1}{4}\kappa^2 \beta \cos^2\theta \log(\tfrac{1}{a}) = jc_3 \quad .$$

---

*ρ_{22} is much less than ρ_{21}, thus $\rho_{21} + \rho_{22} \approx \rho_{21}$ for (ar) $\ll 1$ and a$\ll$1.

The above integral may be evaluated in closed form with following result

$$\sigma^{o}(\theta) = \frac{\kappa^2 |Q_o|^2}{2\pi\cos^2\theta} \quad \frac{e^{-\frac{1}{4}\left(\frac{\alpha^2 c_1}{c_1^2 + c_2^2}\right)}}{\sqrt{c_1^2 + c_2^2}} \left\{ J_o\left(\frac{c_2\alpha^2}{4c_1^2 + 4c_2^2}\right) \right.$$

$$\left. + 2\sum_{n=1}^{\infty} e^{-j\frac{n\pi}{2}} J_n\left(\frac{c_2\alpha^2}{4c_1^2 + 4c_2^2}\right) \right\}$$

or

$$\sigma^{o}(\theta) = \frac{\kappa^2 |Q_o|^2}{2\pi\cos^2\theta} \quad \frac{e^{-\frac{1}{4}\left(\frac{\alpha^2 c_1}{c_1^2 - c_3^2}\right)}}{\sqrt{c_1^2 - c_3^2}} \left\{ I_o\left(\frac{c_3\alpha^2}{4c_1^2 - 4c_3^2}\right) \right.$$

$$\left. + 2\sum_{n=1}^{\infty} I_n\left(\frac{c_3\alpha^2}{4c_1^2 - 4c_3^2}\right) \right\} \quad .$$

Since the series in $I_n(z)$ can be summed to e^z, the following equation results:

$$\sigma^0(\theta) = \frac{\kappa^2 |Q_0|^2}{2\pi\cos^2\theta} \; \frac{e^{-\frac{1}{4}\left(\frac{\alpha^2}{c_1 + c_3}\right)}}{\sqrt{c_1^2 - c_3^2}}$$

or, finally,

$$\sigma^0(\theta) = \frac{|Q_0|^2}{2\pi\cos^4\theta} \; \frac{\exp\left[\frac{-\tan^2\theta}{1.25\beta\log(1/a)}\right]}{0.97\beta\log(1/a)} \; . \tag{26a}$$

Comparing (26a) with the equivalent approximate relation for the isotropic spectrum (equation (10a)), it is obvious that there is little significant difference. It has, therefore, been conclusively demonstrated that the Cote, et al. two-dimensional spectrum and the isotropic spectrum lead to the same scattering cross-section when the two spectra yield the same mean-square height.

A second directional spectral form which has found rather wide acceptance in the oceanographic community is that proposed by Longuet-Higgins, et al. [17], i.e.,

$$\overline{\Psi}_L(k,\psi) = S_L(k) \left|\cos\frac{\psi}{2}\right|^{2s(k)} \tag{27}$$

where the parameter $s(k)$ is a function of the quantity $v\sqrt{k}/10\sqrt{g}$* and g is the gravitational acceleration constant. Measurements [17,18] indicate that $s(k)$ ranges from about twenty (0.164 $v\sqrt{k}$ <0.1) to zero (0.164 $v\sqrt{k} \gtrsim 1$). That is, for a small wavenumber-velocity product the directional spectrum becomes almost unidirectional while for a large $\sqrt{k}\cdot v$ the spectrum is nearly isotropic. In light of some oceanographers' feeling that the capillary waves spread almost isotropically, this spectral representation would appear to be somewhat more realistic than the Cote, et al. form.

---

*For k in (centimeters)$^{-1}$ and v in knots, this factor becomes (0.164) $v\cdot\sqrt{k}$.

The two-dimensional spectrum follows from previous definition, i.e. ,

$$\Psi_L(k,\psi) = S_L(k) \; G(s) \left\{ \left|\cos\frac{\psi}{2}\right|^{2s} + \left|\sin\frac{\psi}{2}\right|^{2s} \right\}$$ (28)

where $G(s)$ is a normalization factor. Assuming that $S_L(k) = S_a(k)$, $G(s)$ may be found by requiring that the mean-square height is the same as for the isotropic spectrum considered in Section 2. That is,

$$h_m^2 = \frac{\beta}{6a^2} = \frac{1}{2\pi} \int_0^\infty \int_0^{2\pi} \Psi_L(k,\psi) \; kdkd\psi$$

which leads to the following form for $G(s)$,

$$G(s) = \frac{\sqrt{\pi}}{2} \frac{\Gamma(s+1)}{\Gamma(s+1/2)}$$

where $\Gamma(\;)$ is the gamma function. The two-dimensional correlation function is;

$$\rho_n^L(r,\phi) = \frac{1}{2\pi h_m^2} \int_0^\infty \int_0^{2\pi} S_a(k)G(s) \left[\left|\cos\frac{\psi}{2}\right|^{2s} + \left|\sin\frac{\psi}{2}\right|^{2s}\right]$$

$$\cdot \; e^{jkr\cos(\psi-\phi)} kdkd\psi \quad \cdot$$ (29)

Expanding the phase term in the integrand of (29) and performing the ψ-integration results in the following:

$$\rho_n{}^L(r,\phi) = \frac{1}{h_m{}^2} \int_0^\infty S_a(k) \left\{ J_0(kr) \right.$$

$$\left. + 2\sum_{n=1}^\infty (-1)^n J_{2n}(kr)\cos 2n\phi \left[\frac{\Gamma^2(s+1)}{\Gamma(s+1+n)\ \Gamma(s+1-n)}\right] \right\} \quad kdk \quad .$$

For the time being, let the infinite sum be approximated by its first two terms, i.e.,

$$\rho_n{}^L(r,\phi) \approx \frac{1}{h_m{}^2} \int_0^\infty S_a(k)J_0(kr)kdk - \frac{2}{h_m{}^2}\cos 2\phi \int_0^\infty S_a(k)J_2(kr)\left[\frac{s(s-1)}{(s+1)(s+2)}\right]kdk$$

$$+ \frac{2}{h_m{}^2}\cos 4\phi \int_0^\infty S_a(k)J_4(kr)\left[\frac{s(s-1)(s-2)(s-3)}{(s+4)(s+3)(s+2)(s+1)}\right] \quad kdk \quad . \tag{30}$$

Since $s(k) \approx 0$ for $(.164)v\ \sqrt{k} \gtrsim 1$, the last two integrals in (30) will be zero for $k \gtrsim 200a = \hat{k}$. That is

$$\rho_n{}^L(r,\phi) \approx \frac{1}{h_m{}^2} \int_0^\infty S_a(k)J_0(kr)kdk - \frac{2}{h_m{}^2}\cos 2\phi \int_0^{\hat{k}} S_a(k)J_2(kr)\left[\frac{s(s-1)}{(s+1)(s+2)}\right]kdk$$

$$+ \frac{2}{h_m{}^2}\cos 4\phi \int_0^{\hat{k}} S_a(k)J_4(kr)\left[\frac{s(s-1)(s-2)(s-3)}{(s+4)(s+3)(s+2)(s+1)}\right]kdk \quad . \tag{31}$$

Because of the dominant (and peaked) behavior of $S_a(k)$ and the finite limits, the last two integrals in (31) may be evaluated by the asymptotic method previously applied [16], i.e.,

$$\rho_n^L(r,\phi) \approx \rho_o(r) + 1.44 \left\{ -\cos(2\phi)J_2(kr)\left[\frac{s(s-1)}{(s+1)(s+2)}\right]_{k=\tilde{k}} \right.$$

$$\left. + \cos4\phi J_4(kr) \left[\frac{s(s-1)(s-2)(s-3)}{(s+4)(s+3)(s+2)(s+1)}\right]_{k=\tilde{k}} \right\}$$

where $\tilde{k} = 1.29_a$. When $k = \tilde{k}$, $(.164)v\sqrt{k} = 0.08$ and $s(\tilde{k}) \approx 8$ [17], thus

$$\left. \frac{s(s-1)}{(s+1)(s+2)} \right|_{k=\tilde{k}} = 0.62$$

$$\left. \frac{s(s-1)(s-2)(s-3)}{(s+4)(s+3)(s+2)(s+1)} \right|_{k=\tilde{k}} = 0.122$$

and

$$\rho_n^L(r,\phi) \approx \rho_o(r) - 0.89J_2(\tilde{k}r)\cos2\phi + 0.176\, J_4(\tilde{k}r)\cos4\phi \qquad . \tag{32}$$

For purposes of $\sigma^o(\theta)$ computation, it is unnecessary to carry the last term in (32) since it has little effect on the subsequent integration. The procedure for calculating $\sigma^o(\theta)$ is exactly the same as in the case of the Cote, et al. spectrum and need not be repeated. The approximate closed form result is;

$$\sigma^o(\theta) \approx \frac{|Q_o|^2}{2\pi\cos^4\theta} \; \frac{\exp\left[\frac{-\tan^2\theta}{\beta[\log(1/a) + 0.07]}\right]}{\beta\sqrt{[\log(1/a)]^2 - 0.07}} \qquad . \tag{32a}$$

As in the case of the Cote, et al. angular dependent spectrum, the Longuet-Higgins, et al. spectral form is seen to yield the same scattering cross-section as the isotropic spectrum. Since both of the spectral forms considered have significantly different behavior, it may be concluded that angular variation in the surface height spectrum has little, if any, effect on the near-normal incidence scattering cross-section. These results have a very significant impact on the ground truth requirements for a near-normal incidence backscattering experiment, such as in the case of Skylab. That is, it would appear that the two-dimensional spectrum need not be measured and simple wave-staff measurements will suffice, i.e., to yield $S_a(k)$ and $h_m{}^2$. Of course, the spectra studied in this report are only truly applicable for fully developed, no swell, large fetch seas. Consideration of what happens when any of these conditions are violated must be necessarily left to future studies.

This result for directional effects together with the gravity-range dominance of the σ^o integral lead to the important conclusion that spectral information needed as ground truth for a σ^o experiment could be acquired at a single point on the ocean's surface by what will be called below a "R(t)-determining experiment." First, however, a number of spectral relationships must be briefly reviewed and, in particular, a relationship between the surface frequency power spectrum and S(k) will be established by assuming the gravity-range dispersion relation.

Let the ocean surface coordinates be $(\vec{r}, \zeta, t)$ where $\vec{r}$ is measured in the plane of the ocean surface, ζ is the surface elevation relative to the plane of mean sea level, and t is time. We will write ζ as a function of $\vec{r}$ and t, i.e., $\zeta = \zeta(\vec{r}, t)$. We will make the usual assumptions of stationarity in t and $\vec{r}$, and then define a generalized surface autocovariance function $Z(\vec{r}, t)$ by

$$Z(\vec{r}, t) = \int_{\vec{r}_1} \int_{t_1} \zeta(\vec{r} + \vec{r}_1, t + t_1) \, \zeta(\vec{r}_1, t_1) \, d\vec{r}_1 \, dt_1 \quad . \tag{33}$$

The three-dimensional (two spatial, one temporal dimension) Fourier transform of $Z(\vec{r}, t)$ is the generalized ocean surface height power spectrum $X(\vec{k}, \omega)$ where $\vec{k}$ is the wavenumber and ω is (radian) frequency.

Let us also define two less general surface autovariance functions $R(t)$ and $\rho(\vec{r})$ by their relationship to $Z(\vec{r},t)$ as follows:

$$R(t) = Z(\vec{r},t)\Big|_{\vec{r} = 0} \tag{34}$$

$$\rho(\vec{r}) = Z(\vec{r},t)\Big|_{t = 0} \tag{35}$$

Note that (34) implies that $R(t)$ could be determined if one had an instrument at a single point in space ($\vec{r} = 0$) which produced a perfect record of ζ vs. t for a sufficiently long t. Such an instrument might be an idealized wave-staff, fixed point laser altimeter, etc.

Similarly $\rho(\vec{r})$ requires an instrument producing a record of ζ vs. $\vec{r}$ over sufficiently large $\vec{r}$ for a fixed time ($t = 0$). Some sort of photographic method seems implied here such as stereo photographs or possibly a Stilwell or related process.

Examining departures from the assumed perfect instruments, there are, clearly, difficulties in experimentally estimating either $R(t)$ or $\rho(\vec{r})$ but, of the two, the $R(t)$ estimation process is much the easier. It is the purpose of this discussion to show that determination of $R(t)$ is sufficient for purposes of a σ^O experiment ground truth program.

Continuing with the general power spectrum properties, two more restricted (and more familiar) surface height power spectra may be defined in terms of the general spectrum $X(\vec{k},\omega)$ as follows;

$$\Phi(\omega) = \int_{\vec{k}} X(\vec{k},\omega)\,dk, \qquad \text{the frequency spectrum} \tag{36}$$

and

$$\Psi(\vec{k}) = \int_{\omega} X(\vec{k},\omega)\,d\omega, \qquad \text{the directional wavenumber spectrum.} \tag{37}$$

Also, $\Phi(\omega)$ is the one-dimensional (time) Fourier transform of $R(t)$, and $\Psi(\vec{k})$ is the two-dimensional (spatial) Fourier transform of $\rho(\vec{r})$. The wavenumber spectrum $\Psi(\vec{k})$ can be written in a polar coordinate form as $\Psi(k,\psi)$ with ψ the

angle relative to the windspeed (assumed equilibrium conditions and a
unidirectional steady wind having been present over infinite fetch and
infinite time) and k the radial wavenumber. Also, without loss of
generality,

$$\Psi(k,\psi) = S(k)F(k,\psi) \tag{38}$$

and the isotropic assumption of the earlier part of the chapter is simply
the assumption that $F(k,\psi) = 1$ for all k and ψ.

There is, in general, no simple relationship between $S(k)$ and $\Phi(\omega)$
unless a unique relationship can be established between ω and k. In many
cases, however, the small amplitude gravity-range dispersion relation
$\omega^2 = gk$ provides a reasonable approximation to surface behavior, and we
will now assume this relationship valid and examine the consequences of
this assumption. In this case for any arbitrary wavenumber $\vec{k}_1$ the gen-
eralized spectrum becomes

$$\chi(\vec{k}_1,\omega) = \Psi(\vec{k}_1)\ \delta(\omega-\omega_1) \tag{39}$$

because with the delta function the dispersion relation asserts that for
any $|\vec{k}_1|$ there is an ω-contribution only at $\omega = \omega_1$. Then equation (36)
for $\Phi(\omega)$, in terms of $\chi(\vec{k},\omega)$, leads to

$$\Phi(\omega) = \int_{\vec{k}_1} \Psi(\vec{k}_1)\ \delta(\omega-\omega_1)\ d\vec{k}_1$$

or in polar wavenumber coordinates,

$$\Phi(\omega) = \int_{\psi=-\pi}^{\pi} \int_{k_1=0}^{\infty} \Psi(k_1,\psi)\ \delta(\omega-\omega_1)\ k_1 dk_1\ d\psi\ . \tag{40}$$

Then using $k_1 = \omega_1^2/g$, $dk_1 = 2\omega_1\ d\omega_1/g$, and from (38), $\Psi(k_1,\psi) = S(\omega_1^2/g)$
$F(\omega_1^2/g,\psi)$,

$$\Phi(\omega) = \int_{-\pi}^{\pi} \int_{0}^{\infty} \frac{2\omega_1^3}{g}\ S(\omega_1^2/g)\ F(\omega_1^2/g,\psi)\ \delta(\omega-\omega_1)\ d\omega_1 d\psi\ , \tag{41}$$

3-48

and because of the properties of the δ-function,

$$\Phi(\omega) = \frac{2\omega^3}{g} \; S(\omega^2/g) \int_{-\pi}^{\pi} F(\omega^2/g, \psi) \, d\psi \quad . \tag{42}$$

Equation (42) may also be written entirely in terms of k with the result

$$S(k) = \frac{g^{1/2}}{2k^{3/2}} \; \frac{\Phi(\sqrt{gk})}{\displaystyle\int_{-\pi}^{\pi} F(k,\psi) \, d\psi} \quad . \tag{43}$$

Recall that $\Phi(\omega)$ is derived from R(t), the single-point and the experimentally more desirable measurement. Equation (43) says that if the gravity wave dispersion relationship can be used and if the ψ-integration can be performed, then S(k) can be derived from $\Phi(\omega)$ and thus from R(t). For the Cote, et al. and Longuet-Higgins, et al. spectra, $F(k,\psi)$ was defined so that

$$\int_{-\pi}^{\pi} F(k,\psi) \, d\psi = 1$$

and (43) reduces to the following:

$$S_{C_L}(k) = \frac{g^{1/2}}{2k^{3/2}} \; \Phi(\sqrt{gk}) \quad . \tag{44}$$

The result of the examination of directional effects on σ^o concluded that $S_{C_L}(k)$ dominated the σ^o integral for an $S_{C_L}(k)$ of a particular form, i.e., $S_{C_L}(k) = S_a(k)$. It would be very surprising to find that the earlier conclusion in this chapter regarding k-ranges of importance to σ^o were to change radically for small changes in the exact form of S(k), so we expect the general

conclusion concerning the gravity range dominance of σ^o to remain valid. This in turn supports the use of the dispersion relation $\omega^2 = gk$ in the derivations just presented. The overall conclusion then is that for directional spectra described by a Cote or Longuet-Higgins form, the σ^o ground truth needs concerning spectral information are met by knowledge of what we have called $R(t)$ since from $R(t)$ we get $\Phi(\omega)$ which through (44) provides the needed $S(k)$. This is an important result given the difficulty of a $\rho(\vec{r})$-determining experiment relative to a $R(t)$-determining experiment.

3.5 SUMMARY & CONCLUSIONS

The subject of this chapter has been the relationship between the ocean surface wavenumber spectrum and the backscattering cross-section σ^o obtained by evaluating the physical optics (or tangent plane) backscattering integral for near-normal incidence microwave scattering. A particular isotropic spectral representation was chosen for the ocean surface based on its k^{-4} limiting behavior for large wavenumber, the existence of a Hankel transform (and hence a closed-form expression for the autocorrelation function), and a not unreasonable fit to the limited low-k data available. This last behavior was not originally expected to be particularly important because of previous analyses based on series approximations or asymptotic expansions which had argued that scattering would be heavily dependent on capillary-range wavelengths; these arguments were in general based on σ^o being proportional to mean-square slope of the ocean surface [10].

Numerically evaluating the physical optics integral after obtaining the autocorrelation function for the isotropic infinite-extent spectrum assumed, it was found that the behavior of the integrand could not be accurately described by asymptotic solutions. A set of results was obtained for σ^o as a function of wind speed and scattering angle which compared favorably with Guinard's experimental data. These results indicated a saturation effect near normal incidence and so predicted a negative result for σ^o vs. windspeed experiments.

Approximate expressions were developed for the correlation function corresponding to a truncated wavenumber spectrum as a means of examining relative importance of different wavenumber regions to the σ^o result. This method showed that the σ^o integral was dominated by the long wavelength range of the ocean spectrum and was effectively independent of the capillary range contrary to predictions of mean square slope arguments as noted above. It was found that for centimeter range rf wavelengths, σ^o depends heavily on ocean surface characteristics in the ocean wavelength range of 0.06 to 60 meters, and therefore ground truth activities for support of near-normal incidence radar scattering experiments should be planned on this basis.

Finally the consequence of the assumption of isotropic ocean surface spectra was investigated. The directional spectra of Cote et al. and Longuet-Higgins et al. were assumed, and another set of approximations was developed to obtain a two-dimensional autocorrelation function which was then used in the physical optics integral. It was demonstrated that the dominant component for the σ^o calculation was the isotropic component of $\rho(r,\phi)$. Since σ^o for near-normal incidence depends on components in the gravity wave range, the gravity wave dispersion relation is valid for the ocean wavelengths dominating σ^o. These results have the important consequence that the only ocean surface characterization needed for ground truth is what Cote et al. call the "wave pole spectrum"; that is, the frequency (power) spectrum obtained at a single point on the surface (by a wave pole, or other means of obtaining a surface height vs. time record) and transformed to wavenumber space by use of the gravity wave dispersion relation.

REFERENCES

1. Phillips, O. M., "The Equilibrium Range in the Spectrum of Wind Generated Waves," J. Fluid Mech., 4, pp. 426-434, 1958.

2. Pierson, W. J., Jr. and L. Moskowitz, "Proposed Spectral Form for a Fully Developed Wind Seas Based on the Similarity Theory of S. A. Kitaigrodskii," J. Geophys. Res., 69, No. 24, pp. 5181-5190, 1964.

3. Hess, G. D., G. M. Hidy, and E. J. Plate, "Comparison Between Waves at Sea and in the Laboratory," J. Marine Res., 27, No. 2, pp. 216-225, 1969.

4. Bass, F. G., et al., "Very High Frequency Radiowave Scattering by a Disturbed Sea Surface," Trans. on Antennas and Propagation, AP-16, No. 5, pp. 554-568, 1968.

5. Valenzuela, G. R., et al., "Ocean Spectra for the High Frequency Waves Determined from Airborne Radar Measurements," Journ. of Marine Research, 29, pp. 69-84, 1971.

6. Cox, C. and W. Munk, "Measurement of the Roughness of the Sea Surface from Photographs of the Sun's Glitter," J. Opt. Soc. Am., 44, pp. 838-850, November, 1954.

7. Hagfors, T., "Backscattering from an Undulating Surface with Applications to Radar Returns from the Moon," J. Geophys. Res., 69, No. 18, pp. 3779-3784, 1964.

8. Peake, W. H., D. E. Barrick, A. K. Fung, and H. L. Chan, "Comments on 'Backscattering of Waves by Composite Rough Surfaces," IEEE Trans on Antennas and Propagation, AP-18, pp. 716-726, September, 1970.

9. Abramowitz, M. and I. A. Stegun, Handbook of Mathematical Functions, NBS Applied Math Series, Vol. 55, U.S.G.P.O., pp. 488, June, 1964.

10. Barrick, D. E., "Rough Surface Scattering Based on the Specular Point Theory," IEEE Trans. Antennas and Propagation, AP-16, pp. 449-454, 1968.

11. Hagfors, T., "Relationship of Geometric Optics and Autocorrelation Approaches to the Analysis of Lunar and Planetary Radar," J. Geophys. Res., 71, pp. 379-383, 1966.

12. Fung, A. K. and H. L. Chan, "Backscattering of Waves by Composite Rough Surfaces," IEEE Trans. Antennas and Propagation, AP-17, pp. 590-597, September, 1969.

13. Barrick, D. E., "Unacceptable Height Correlation Coefficients and the Quasi-Specular Component in Rough Surface Scattering," Radio Science, 5, pp. 647-654, April, 1970.

14. Guinard, N. W., "The Variation of the RCS of the Sea with Increasing Roughness," Microwave Observations of the Sea, Proceedings of the Spacecraft Oceanographic Project, pp. 175-203, 11-12 June, 1969, NASA HQ, Washington.

15. Cote, L. J., et al., "The Directional Spectrum of a Wind Generated Sea as Determined from Data Obtained by the Stereo Wave Observation Project," Meteorological Papers, Vol. 2, No. 6, pp. 88, New York, New York: New York Univ. Press, 1960.

16. Evgrafov, M. A., Asymptotic Estimates and Entire Functions. Gordon and Breach Publ., New York, pp. 20-22, 1961 (English Translation).

17. Longuet-Higgins, M. S., D. E. Cartwright, and N. D. Smith, "Observations of the Directional Spectrum of Sea Waves Using the Motions of a Floating Buoy," Ocean Wave Spectra, pp. 111-131, Englewood Cliffs, New Jersey: Prentice-Hall, 1963.

18. Ewing, J. A., "Some Measurements of the Directional Wave Spectrum," J. Marine Res., 27, No. 2, pp. 163-171, 1969.

19. Chia, R., "The Theory of Radar Backscatter from the Sea Ph. D. Dissertation, University of Kansas, 1968.

20. M. I. T. Staff, The Terrestrial Environment: Solid-Earth and Ocean Physics, NASA Contractor Rpt. No. NASA CR-1579, Prepared by MIT, page 3-9, 1970.

21. Schule, J. J., L. S. Simpson, and P. S. DeLeonibus, "A Study of Fetch-Limited Spectra with an Airborne Laser," J. Geophys. Res., 76, No. 18, pp. 4160-4171, 1971.

CHAPTER 4

DISCUSSION OF ALTIMETER SEA STATE BIAS AND SEA-TRUTH
INSTRUMENTATION CONSIDERATIONS

4.0 BACKGROUND

If a radar altimeter were to illuminate a perfectly smooth, flat and
highly conducting ocean surface, there is no question that the time delay
between transmission and reception of the radar pulse would be proportional
to the radar's height above the surface. When the surface becomes rough,
the proportionality will still hold provided the probability density of the
surface height, as seen by the radar, is symmetric about the true geometric
"mean-sea-level" (MSL). If the height probability density, as seen by the
radar, is not symmetric about the true geometric MSL, the height above the
mean surface as measured by the radar will differ from the true geometric
height. This difference between the true and radar measured heights is due
to the so-called sea-state bias. For conventional applications, such a
difference would not appear to be significant, however, for precision altimetry
the difference may be on the order of the desired altitude accuracy. Although
the difference could conceiveably be calibrated out, such an approach would
require knowledge of the scattering surface which is most certainly not known,
at least in real time. For this reason, the sea-state bias problem is of great
importance to precision radar altimetery.

Since Yaplee, et al. have presented the only experimental evidence of the
existence of sea state bias, their work will be discussed in this report. In
particular, we present one interpretation of their results in Section 4.2 which
indicates that the backscattering cross section of the ocean's surface as
observed by the radar may be considered to be a linear function of the wave
height below mean-sea-level. That is to say, the average power backscattered
by the wave troughs is greater than the average power backscattered by the
crests on the ocean's surface. It should be noted that such reasoning is not
in conflict with the backscattering cross-section analysis presented in
Chapter 3 since that analysis applied only to the CW cross-section and not to
the time or range dependent σ^o.

In Section 4.3 we present an initial investigation of the experimental
techniques required to assess the magnitude of the sea-state bias problem. In
particular, we first attempt to resolve what statistical information on the
ocean's surface is pertinent to the problem. We conclude that flying a laser
profilometer over the surface of the ocean would be the most accurate method
of obtaining the desired statistics, although this approach does have some

shortcomings. In the process of investigating the various sea-state measurement methods, we found some shortcomings in the Stilwell photographic technique. Although the Stilwell method does not appear to be applicable to the sea-state bias problem, it has been proposed for use in obtaining the statistics required for the CW backscattering cross-section discussed in Chapter 3. For this reason, some comments on the Stilwell technique are presented in Section 4.4 and it is concluded that further refinements in the method will be required and that it is premature to rely on the method as the principal sea truth sensor.

4.1 The Bias Problem

In earlier reports [1, 2], we concluded that for times and distances of interest in the satellite altimeter problem, the sea surface scattering was incoherent and independent. In the following discussion it will be assumed that the satellite antenna is pointed at nadir and that the antenna beamwidth is sufficiently broad that antenna effects can be ignored during the leading edge (or "ramp") portion of the radar return waveform. Transmitter and receiver bandwidths will be ignored, and we will assume a sufficiently large number of pulses that we have adequate estimates for sea surface ensemble averages. It is convenient to talk in terms of a large number of scattering regions or "scatterers" distributed on the ocean's surface, and without loss of generality the vertical or z-direction distribution of these scatterers can be described by a probability density function $p(z)$. The z-axis origin is at the plane of mean sea level. It is worth noting that $p(z)$ can be written as an equivalent $p(t)$ describing the distribution of radar return times relative to the time for a flat-sea return by use of the two-way relationship $t = \frac{2z}{c}$ (c is the speed of light); this $p(t)$ is the time function to be determined from the waveform analysis discussed in Chapter 2 of this report.

The quantity $p(z)$ will also be referred to as the radar-observed waveheight distribution, as opposed to the "true" waveheight distribution $q(z)$ which would be measured by a perfect profilometer or an idea wavepole. The bias problem concerns the possibility of a relative shift between the means of $p(z)$ and $q(z)$, while the objective of the altimeter is to determine distance to the mean of $q(z)$. This possible shift or bias may be a function of rms ocean surface roughness, and this means that the bias could not simply be treated as a constant systematic error since the altimeter looks at regions of different ocean roughness.

It is possible to restrict the bias problem to asking to what extent $p(z)$ is an odd function of z since we showed earlier [2] that for a scattering process which could be described by an equivalent $p(z)$, the receiver power was completely symmetric in behavior about the half power point $T_{1/2} = \tau_R + T/2$ if $p(z)$ was an even function of z. Here, $T_{1/2}$ is measured from the start of transmission of a radar pulse of width T, and τ_R is ranging time from satellite to the plane $z = 0$ and back. By "symmetric in behavior about $T_{1/2}$" we mean

that for any time increment, Δ, exactly as much additional power (in excess of that expected if the sea were completely flat or smooth) is received at time $t_- = T_{1/2} - \Delta$ as is lost (again relative to the flat sea case) at time $t_+ = T_{1/2} + \Delta$. Thus for any tracking scheme which is not affected by this effect of signal removed at t_+ and added to t_- no sea state bias is introduced if $p(z)$ is even in z; both double-delay differencing and the S-193 split-gate tracker satisfy this tracker criterion.

With but one exception, no experiments are available to allow estimates of possible sea state bias, and one can only regard this as an open question; it is important to realize that there is no solid basis for the often-made assumption that $p(z) = q(z)$. The one exception is the experiment of Yaplee et al. [3] which is discussed immediately below. Following that, other experi- mental techniques are discussed for possible application to the bias problem.

4.2 Yaplee's Data and Sea State Bias

The experimental data recently published by Yaplee et al. [3], on their nanosecond radar measurements, represents the first instance in which the sea state bias problem has been experimentally investigated. The bias figures given in Yaplee are much larger than generally anticipated for low sea state; however, the data base is quite limited. It is of interest at this time to examine Yaplee's data in terms of its inferences regarding the radar $p(z)$. That is, on physical grounds we expect the radar wave height profile to be a distorted version of the wave height profile. His data may be interpreted as indicating that this distortion appears as mainly a displacement in the two distributions. In the following we find that this apparent displacement can be accounted for, within experimental error, by assuming a linear wave height dependence in the radar cross-section data. Much more data will be needed to test the generality of this linear model.

Yaplee's experimental configuration is that of a beamwidth limited exploration of the sea surface. The surface area investigated is that due to an essentially collimated beam. The data we wish to discuss are contained in Yaplee's Figures (6a), (6b), (7a), and (7b); these are reproduced herein for convenience. Figures (1) and (2) represent radar cross-section per unit projected area when they occur. These figures do not reflect the probability of an echo occurring at a particular delay and they represent only two of the infinitude of possible sea surface conditions.

In attempting to model rough sea effects, it has been universally assumed that the cross-section is a function of the area of the ocean surface illuminated. There can be no large quarrel with this assumption; however, there is presently no basis for assuming that the scattering cross-section per unit area is independent of height above "mean sea level," MSL (and only a function of the projected area above that height). Figure (1) and (2) can, in fact, be interpreted as showing that radar cross-section of the ocean surface over the range of wave heights increases essentially linearly with increasing distance below the wave crests. For these figures, the slope of the linear increase is approximately

$$m_a - \frac{.185}{h} \qquad \text{for Figure (1) (calm seas)}$$

$$m_a = \frac{.141}{h} \qquad \text{for Figure (2) (21 knot wind)}$$

where h is the rms wave height.

If we take the geometrical centers of the delay expanse in Figures (1) and (2) as identifying mean sea level (MSL), then the variation of radar cross-section about MSL is given by $\sigma(z)$

$$\sigma(z) = \sigma^o (1-m \frac{z}{h})$$

where z is measured positive above MSL, and σ^o is the conventional radar back-scatter cross-section as in Chapter 3. We can take Yaplee's result in Figures (3) and (4) as an evaluation of $p(z)$, which can therefore be interpreted as the product of two terms:

$$p(z) = q(z) \frac{\sigma(z)}{\sigma^o}$$

where $\sigma(z)^o$ describes the variation of radar cross-section per unit area and $q(z)$ is the probability of finding a surface element z meters above MSL. Note that $\sigma(z)$ can be experimentally determined by Yaplee's data, and $q(z)$ can be obtained from wave staff data.

CLT-17   WIND CALM
1240 HRS   6/19/70

RADAR
    2.*SIGMA = 3.46 NS

VERTICAL SCALE = 50/DIV

20   24   28   32   36   40
NANO-SEC
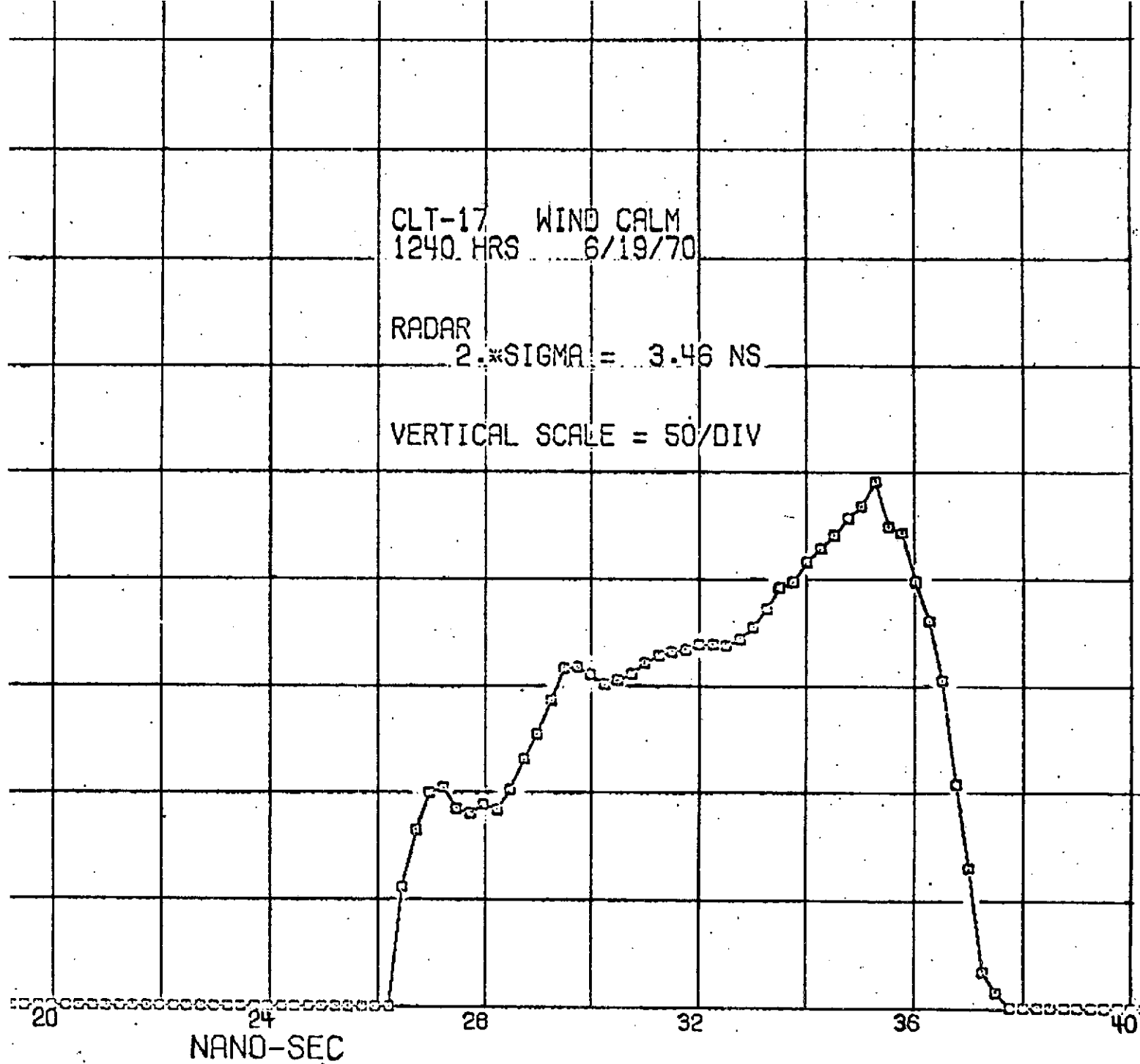
Figure 1.   Reflected Power versus Wave Depth (Calm Sea).
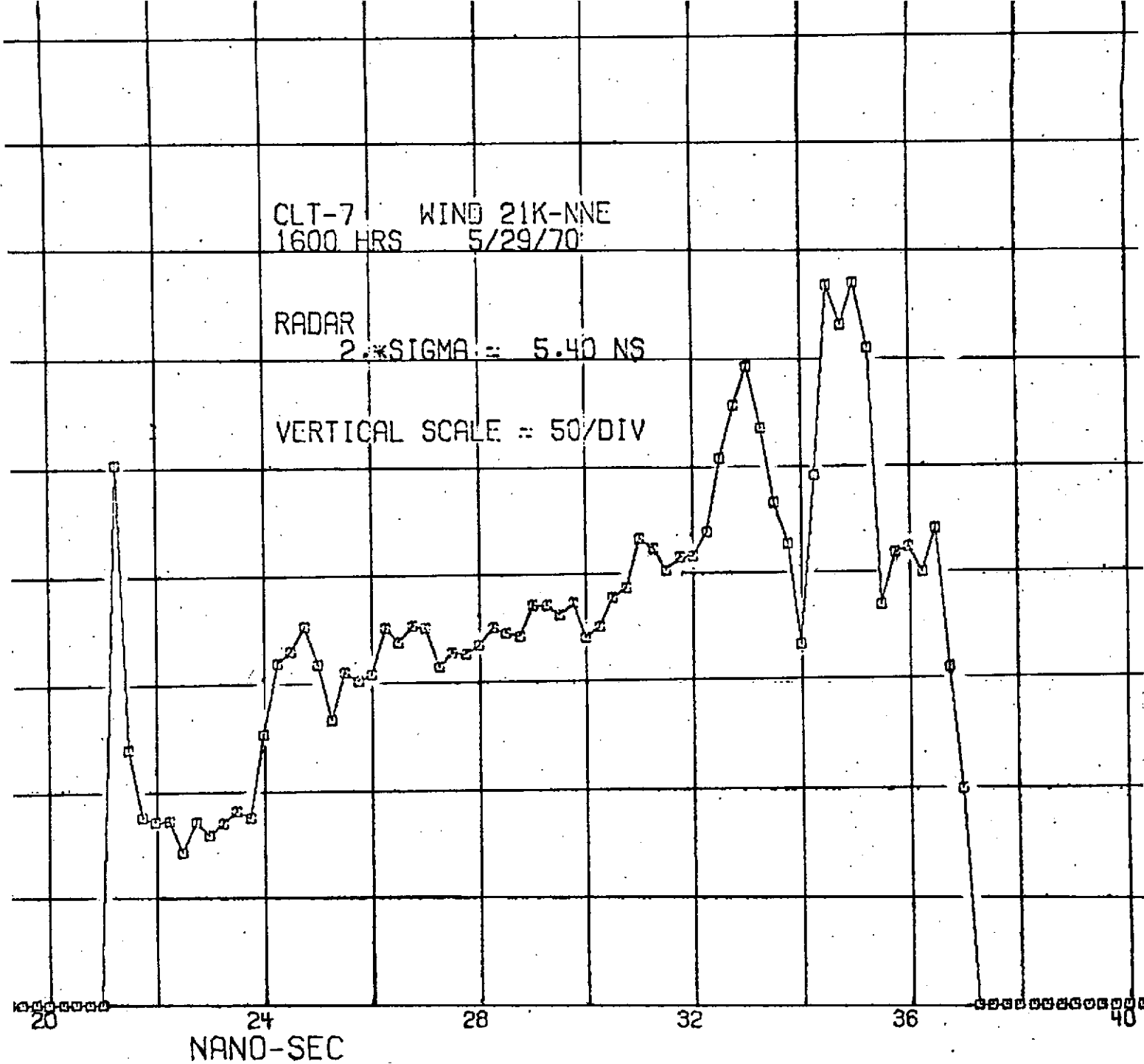
Figure 2. Reflected Power versus Wave Depth
(21 Knot Wind).
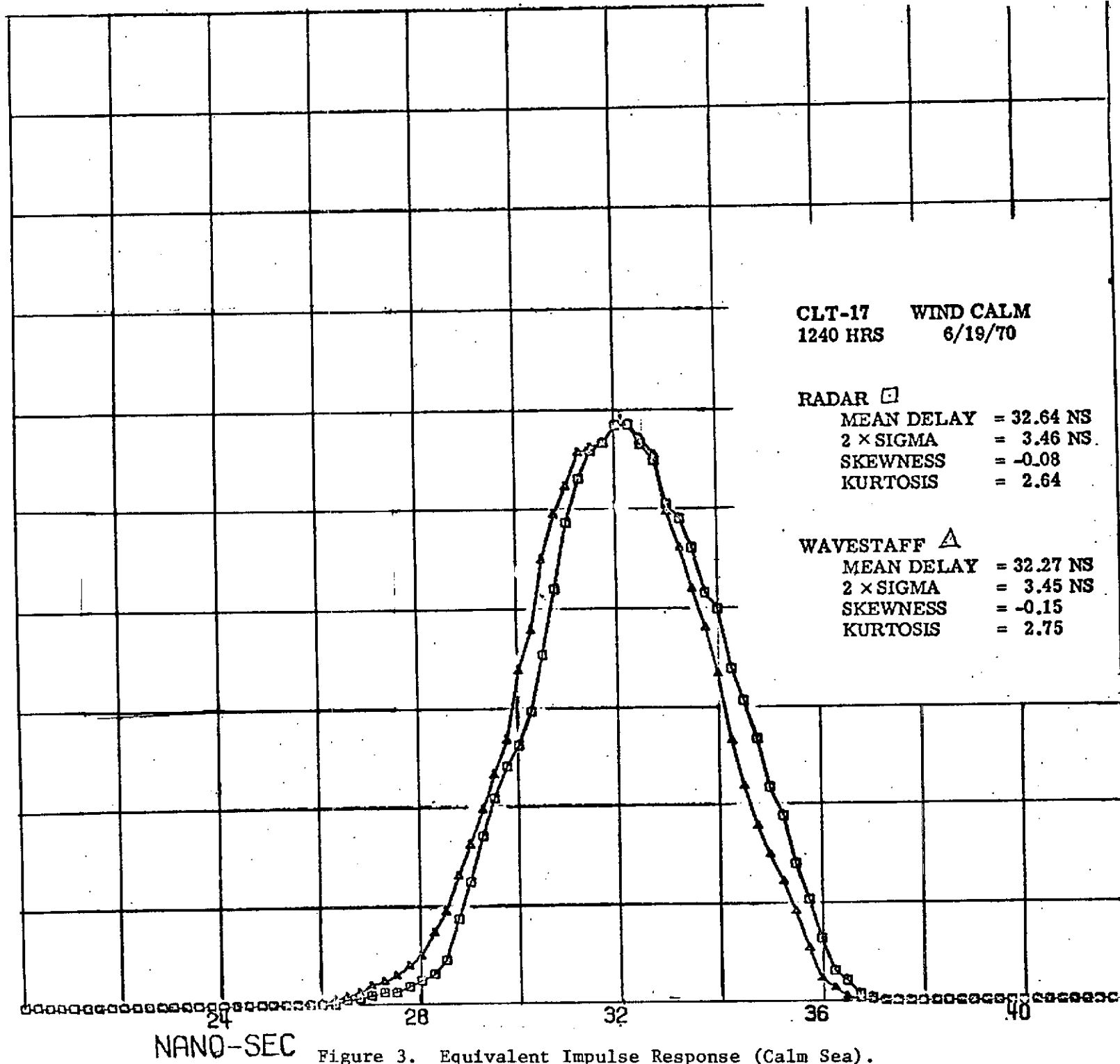
Figure 3. Equivalent Impulse Response (Calm Sea).

CLT-7   WIND 21K-NNE
1600 HRS   5/29/70

RADAR ▢

MEAN DELAY	=	29.36 NS
2 × SIGMA	=	5.40 NS
SKEWNESS	=	-0.06
KURTOSIS	=	2.95

WAVESTAFF △

MEAN DELAY	= 28.8 NS
2 × SIGMA	= 5.84 NS
SKEWNESS	= -0.19
KURTOSIS	= 3.08

NANO-SEC

Figure 4.   Equivalent Impulse Response
(21 Knot Wind).

We might expect that $q(z0$ may well be of the form proposed by Pierson and Mehr [5]. However, for the conditions at the time the data of Figures (1) and (3) were taken (calm sea-swell), the skewness parameter λ is expected to be quite small. Accordingly, we take

$$q(z) = \frac{1}{\sqrt{2\pi h^2}} \exp \left\{ - \frac{z^2}{2h^2} \right\} .$$

We are concerned, therefore, with the behavior of $q(z)$ and $p(z) = \sigma(z) q(z)$.

4.2.1 Numerical Calculations

In Figure 5, three curves are plotted, i.e.,

$$p(x) = \sigma(x) \, q(x) = \exp \left\{ - \frac{x^2}{2} \right\} [1-mx] \qquad \text{weighted Gaussian}$$

$$q(x) = \exp \left\{ - \frac{x^2}{2} \right\} \qquad\qquad\qquad \text{true Gaussian}$$

$$q(x + .175) = 1.02 \exp \left\{ - \frac{(x - .175)^2}{2} \right\} . \qquad \text{displaced Gaussian}$$

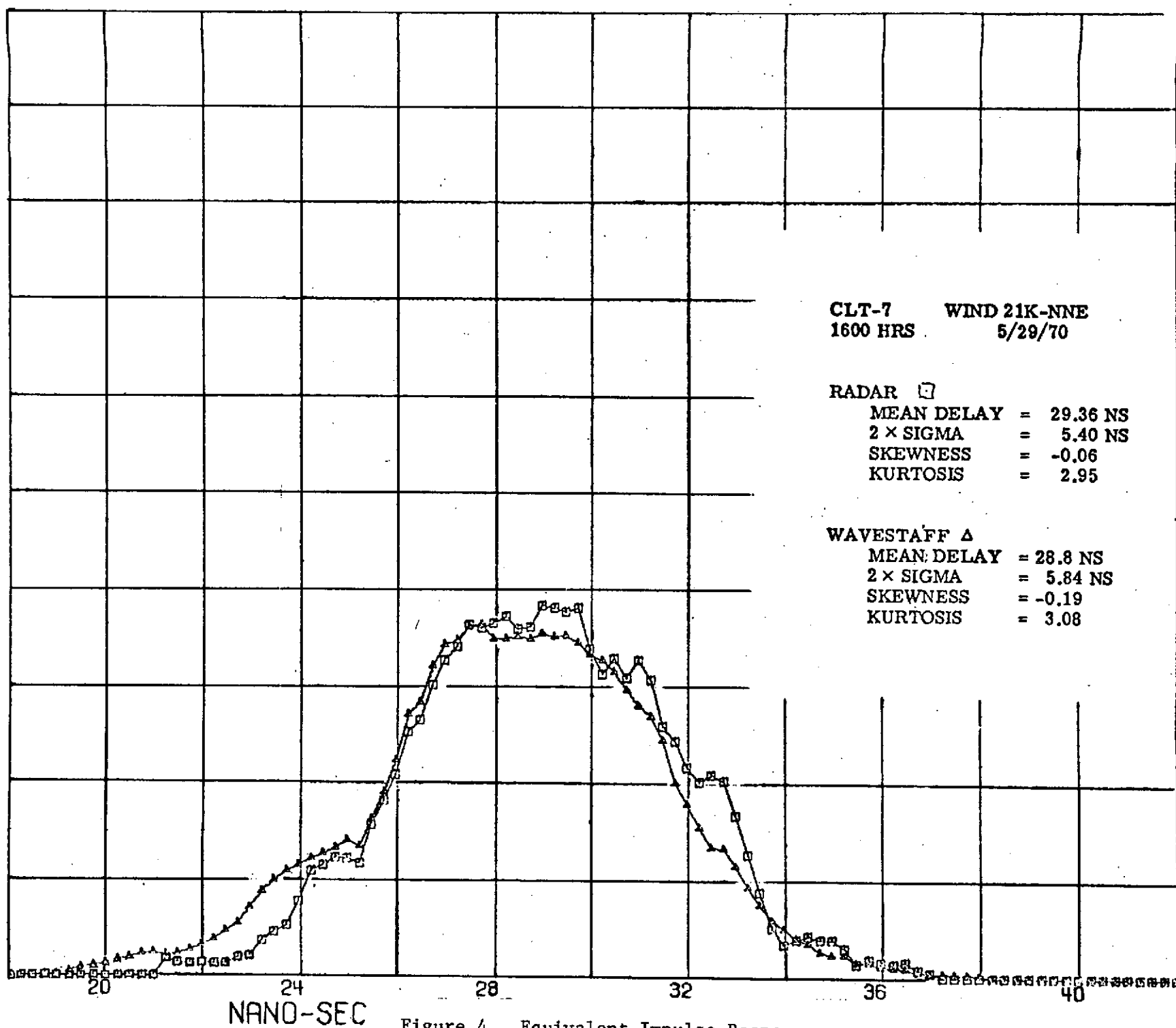In these curves, which attempt to model the data in Figures (1) and (3), m is taken to be .115. Comparison of the curves for $p(x)$ and $q(x)$ indicates that the $p(x)$ curve is displaced from the wave height distribution, just as is the data in Figure (3). The x variable used in these calculations is the height normalized by the rms wave height. From Figure (3), we find that the rms wave height expressed in nanoseconds is 1.725. The delay between the peaks of the two curves ($p(x)$ and $q(x)$) in Figure 4 is therefore .30 nanoseconds. The third curve (merely the Gaussian curve shifted and re-normalized) shows the extent to which $p(x)$ can be approximated by a shifted Gaussian curve. The reader may satisfy himself that Yaplee's radar data in Figure (3) can be obtained by simply shifting the wave staff data .3 nanoseconds to the right.

4-10

It would appear that we can explain the shift in Yaplee's radar curve in Figure (3) by simply accounting for the height dependence of the scattering cross-section with the $\sigma(z)$ term. Note that for this sea condition, the original Pierson-Mehr formulation cannot support the data-- it would require a λ of approximately .37 for a calm sea! Note further that the Pierson-Mehr correction to a Gaussian curve is essentially a cubic $[1 + \frac{\lambda x}{6} (x^2-3)]$ and that there will be three places at which the Gaussian intercepts the composite curves. Yaplee's data show only one intersection between the radar and wave staff data--which would be expected if the radar data are just shifted wave staff data. This may be taken as further proof that for this sea condition the wave staff data are essentially Gaussian.

4.2.2 Effects of Cross-Section Varying with Height Above MSL

The data of Figures (1) and (2) suggest that for swell conditions, $p(x)$ might be represented by:

$$p(x) = \exp \left\{ -\frac{x^2}{2} \right\} [1-mx].$$

It is further shown that this curve can be approximated by a renormalized shifted Gaussian. To get an estimate of the shift:

$$\frac{dp(x)}{dx} = e^{-x^2/2}[-x(1 - mx) - m] = 0$$

$$x_o = \text{shift to maximum} = \frac{1}{2m} - \sqrt{\left(\frac{1}{2m}\right)^2 + 1}$$

$$z_o = \text{height shift of maximum} = h\left(\frac{1}{2m} \sqrt{\left(\frac{1}{2m}\right)^2 + 1}\right).$$

As the slope of the cross-section versus height curve (Figures (1) and (2), for example) increases, the offset asymptotically approaches the rms wave height and the curve becomes more and more non-Gaussian. For moderate values of m, the curve should be a reasonable offset. Such an offset in $p(z)$ will result in an identical bias error in the altimeter experiment.
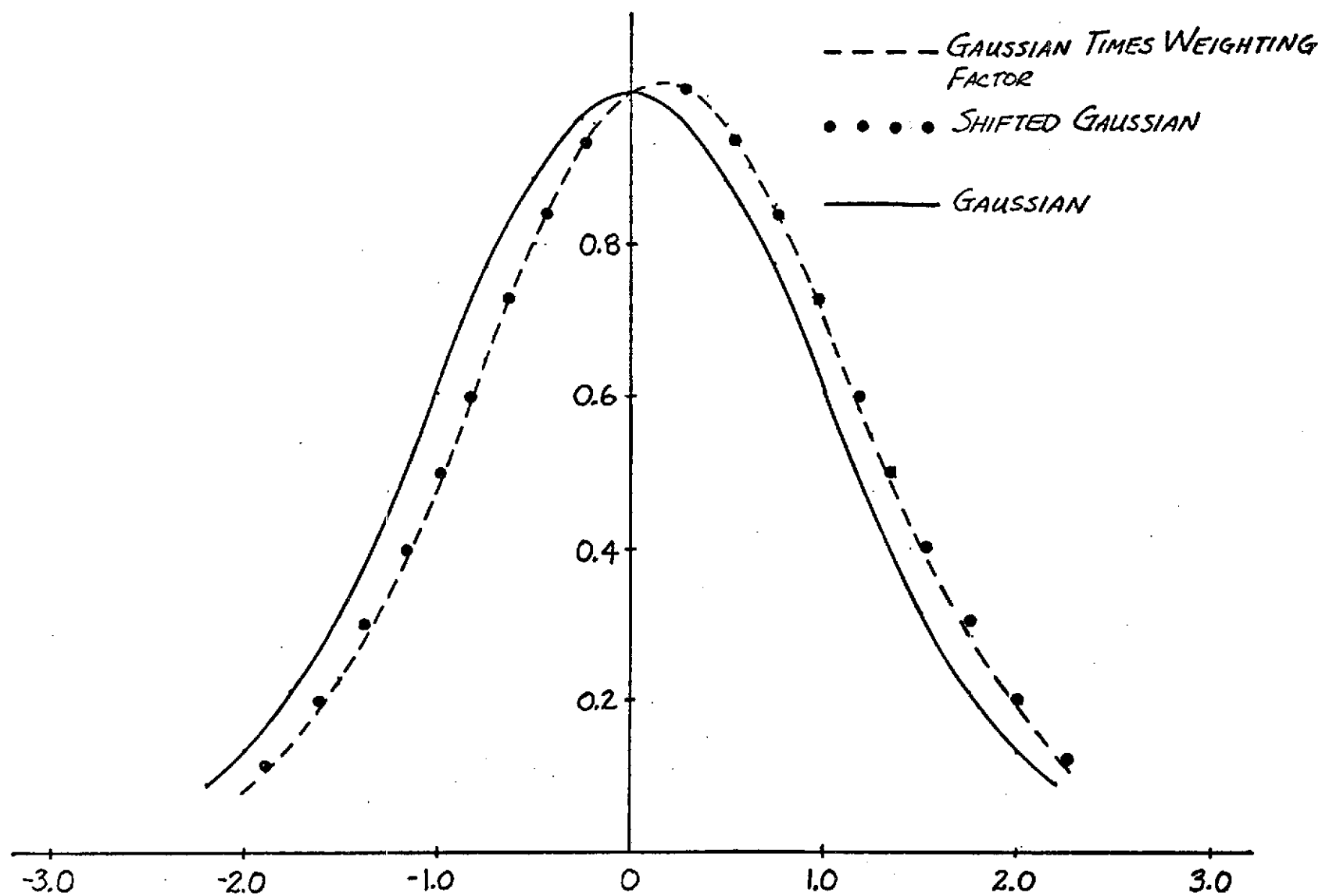
Figure 5. Comparison of linearly weighted Gaussian Model of p(z) and shifted curve.

4.2.3 Possible Variation of Offset with Sea State

Under conditions of a true wind-driven sea, one might expect that the variation of radar cross-section with height above mean sea level may change. It is not inconceivable that "m" might decrease. With increasing wind speed, one might also expect the value of λ, the skewness parameter in the wave height distribution, to increase. The overall effect on sea surface bias will still be contained in the formula for p(z)

$$p(z) = \exp\left\{-\frac{z^2}{2h^2}\right\}\left[1 + \frac{\lambda}{6}\left\{\left(\frac{z}{h}\right)^3 - \frac{3z}{h}\right\}\right]\left[1 - m\frac{z}{h}\right].$$

These detailed variations with wind speed and sea state are not known and must be measured. In any event, Yaplee's data makes a clear case for the inclusion of a term which reflects the increasing radar cross-section per unit area with increasing distance below the wave crests.

4.3 Experimental Techniques Related to the Bias Problem

One possible approach is to determine what sea surface geometric features actually are important to the electromagnetic scattering process, then to measure a sufficiently large ocean profile to be able to derive reasonable estimates of the z-variation of these features. Which features are important will depend on which scattering theory is assumed, and the available comparisons between theory and experiment are largely inconclusive for the available scattering models so no strong basis exists for accepting or rejecting any of these.

We choose for the moment only two of the many different scattering models, the Kodis [5] specular point model, and Schooley [6] facet model as used by Sledge and George [7]. In the Kodis model, the scatterers are identified with specular points, local regions on the surface (of zero-slope for normal incidence backscattering) whose relative radar scattering is a function of the radius of curvature at the specular point; the model is based upon physical optics. In contrast to this, the various phenomenological facet theories define a facet by some arbitrary criterion and derive scattering properties based upon a distribution of flat plates whose dimensions are given by the facet lengths. Schooley defined facet angle by the tangent to the wave profile and the facet length by requiring that the actual profile deviate less than $\lambda_{rf}/10$ from this tangent. A distribution of facet length vs. angle was experimentally derived from a series of photographs of waves in a windtunnel wave-tank, and Sledge and George later used this experimental result to derive a radar scattering cross section on the flat disk basis.

It is important to realize that all backscattering theoretical work to date has been directed toward σ°, the backscattering cross section which would be measured by a CW experiment and that whole-surface averages of the relevant surface geometry properties have been used. This is inadequate for the non-CW processes of a radar altimeter and the appropriate surface properties must be defined as a function of z. Specifically, surface geometry should be used to determine the effective cross-section as a function of height $\sigma(z)$, and the relationships between $\sigma(z)$, $p(z)$, σ°, and the geometric waveheight distribution

q(z) are:

$$p(z) = \sigma(z) \ q(z)$$

$$\sigma^\circ = \int_{-\infty}^{\infty} p(z) \ dz \quad .$$

The next paragraphs discuss geometric or profiling types of approach to the determination of $\sigma(z)$ as a means of estimating bias to be expected. The alternative to a geometric approach is a pulse amplitude vs. time experiment of the Yaplee type, and the possible use of a laser profilometer for this is discussed later.

4.3.1 Geometry Measurements

Although the ocean's surface is anisotropic, we will assume in this entire section that the surface is isotropic and can be represented adequately by a one-dimensional (spatial) spectrum. It will turn out to be quite difficult enough to find experimental evidence to answer the sea-state bias question for the isotropic sea, and we will wait until this problem is in better shape before moving to the increased complexity of the anisotropic sea. The immediately obvious difficulty is that the electromagnetic theories require statistical descriptions of the spatial properties of the sea at a given instant of time while the simpler oceanographic information to experimentally obtain (by means of a wave staff) gives information on the time behavior of a single spatial location. One can derive the spatial statistics from the temporal statistics only to the extent that the wave dispersion relation is valid. Let us first assume that a perfect one-dimensional ocean surface profile is available for some instant of time and describe the processing of that record for the specular point and the facet models.

To get at the sea-state bias problem via the specular point theories, we need to determine the joint probability density of z and its first and second derivatives, $p(z_{xx}, z_x, z)$. For any fixed height z above mean sea level then we

would have $p(z_{xx}, z_x, z)$ which would allow evaluation of quantities appearing in scattering theory. Specifically, the relative number of specular points for vertical incidence radar backscattering would be given by integrating $p(z_{xx}, 0, z)$ over the range of allowable z_{xx} for the different z values of interest to find the quantity $\sigma(z)$. Using the geometric distribution $q(z)$ and $\sigma(z)$, one could then examine the symmetry of $p(z)$ about $z = 0$. In practice the determination of $p(z_{xx}, z_x, z)$ would be an enormous job even given a perfect profile record and one would instead find several pairs of density functions $p(z_{xx}, 0, + z_1)$ and $p(z_{xx}, 0, - z_1)$, $p(z_{xx}, 0, + z_2)$, and $p(z_{xx}, 0, - z_2)$ etc., symmetrically located at $\pm z_1$, $\pm z_2$, etc., relative to mean sea level, $z = 0$. These pairs of corresponding "horizontal slices" through the ocean surface would then allow comparison of $p(z_1)$ with $p(-z_1)$, $p(z_2)$ with $p(-z_2)$, etc. In this way we should be able to fix limits on the sea-state bias.

The other approach is to define facets in the manner of Schooley. Then processing the profile data to find facet length ℓ, facet angle α, and the facet height relative to mean sea level z, the joint probability distribution $p(\ell_1, \alpha_1, z)$ can be determined. This again would be done at the pairs of z values $\pm z_1$, $\pm z_2$, etc., to get the sea-state bias.

Given the perfect record assumed here, all of the above processing would be carried out to determine the possible sea-state bias expected from the several different possible scattering models. Actual details of the processing of a real surface profile record would depend upon such factors as resolution, noise, stability, length of record and so forth. Since a perfect record is unavailable, let us examine next what kind of actual record might be obtained.

All of the preceding discussion has emphasized the need for a spatial record, and methods which might give such information include Stilwell techniques, wave staff arrays, stereo photographs, or some type of flying profilometer. We will discuss these in turn, with the conclusion that a helicopter-borne laser profilometer represents the only possibility with even a chance of yielding the required information.

First consider the Stilwell [8] technique of obtaining the two-dimensional wave-number spectrum of the sea surface by optical transform analysis of a photograph of the surface. This method looks promising for the future but it

is not a fully operational quantitative method yet. Perhaps more important for purposes of the sea-state bias problem, the Stilwell technique does not produce the necessary information on variation with height of surface geometry features (for instance, slopes and specular points). So although the Stilwell technique may, with enough development, become important for obtaining the overall surface backscatter cross-section (for CW measurements), it will not be useful now for the bias problem.

Wave staff arrays have been described by Barber [9]; their drawback is that the wavestaff spacing used must be half the smallest wavelength that one wishes to study and, with our interest in ocean wavelengths comparable to the incident 3 cm radar wavelength, the wave staff separation required becomes prohibitively small.

Stereo photographic techniques can obviously reproduce the structure of the ocean surface at a single instant, and their main difficulty is in the cost of analysis of the photographs. The well-known SWOP project, described by Cote et al. [10], resolved wavelengths down to about 60 feet. Of more interest for the radar problem is a more recent series of measurements performed July and December 1965 in a joint effort by the Applied Physics Laboratory of the Johns Hopkins University, the Naval Research Laboratory, and Oceanics, Incorporated. In this case the cameras were separated by about 20 feet and covered a 20 by 20 foot area of the ocean surface with 60% overlap. Various stages of this experiment were described by Katz [11], Valenzuela and Dobson [12], and Dobson [13]. The wave height is measured at 4mm intervals in some of the analyzed results, and at 25mm intervals in others; Dobson [13] reports vertical resolution of 0.3 inches but the profile shown as Figure 1 of that paper looks much better than 0.3 inches, possibly as good as 0.03 inches. Attempts had been made to determine mean squared slopes from the stereo photographs but the results were inconclusive, and the Applied Physics Laboratory group has doubts about the overall usefulness of stereo photographic methods because of the cost of the photographic analyses.

The most promising type of experiment would be to fly some sort of profiling device over the ocean's surface, and the two candidates for this

would be the laser profilometer or the nanosecond radar of Yaplee's group at Naval Research Laboratory. The spot size of the radar is approximately one meter while the average facet length as defined by Schooley is only about 8 cm, so the radar return can come from one or several facets (at least in terms of this particular model). Because of this, we feel that an appropriate experiment for the radar is a thorough study of the radar return signal amplitude as a function of height of the illuminated area of the sea (with the height measured by non-radar means) as well as correlation of the results with oceanographic conditions. This series of measurements is best done at a fixed location. This leaves the laser profilometer to be considered for the sea state bias problem.

Flying a laser profilometer at low altitude and relatively low speeds in both upwind-downwind and cross wind directions appears to be the only currently feasible technique for obtaining the geometric data needed to attack the sea-state bias problem. Only a portion of the one-dimensional wave number spectrum can be obtained by this technique, depending on flying speed and on the profilometer's bandwidth or response time. Figure 6 shows the upper and lower ocean wavelengths detectable as a function of speed of the profilometer-carrying helicopter or airplane, based on the following discussion.

We are assuming the following characteristics for the profilometer: spot size, 2-1/2 cm, height resolution, 1/4 cm, and a bandpass of 0-1000 Hz for height measurements. (Notice that the height resolution is only $\lambda_o/10$ for the X-band radar λ_o, and that this is just on the edge of what is needed on any kind of facet model basis.) If this is flown at speed v over a stationary corrugated surface of wavelength λ, the minimum λ for a given v is fixed by the 1000 Hz limit at $\lambda_{min} = v/(1000 \text{ sec}^{-1})$.

There is also an upper wavelength limit, λ_{max}, set by a requirement that the profilometer traverse any given wavelength, λ, within a time equal to or less than T/10 where T is the period corresponding to that λ. The reason for this is that unless the record of a wave can be made in a time short compared to the wave's frequency, it is necessary to take account of the wave's motion and correct the airplane speed taking account of the relative motion of profilometer and ocean wave. Such a correlation requires use of the phase speed of
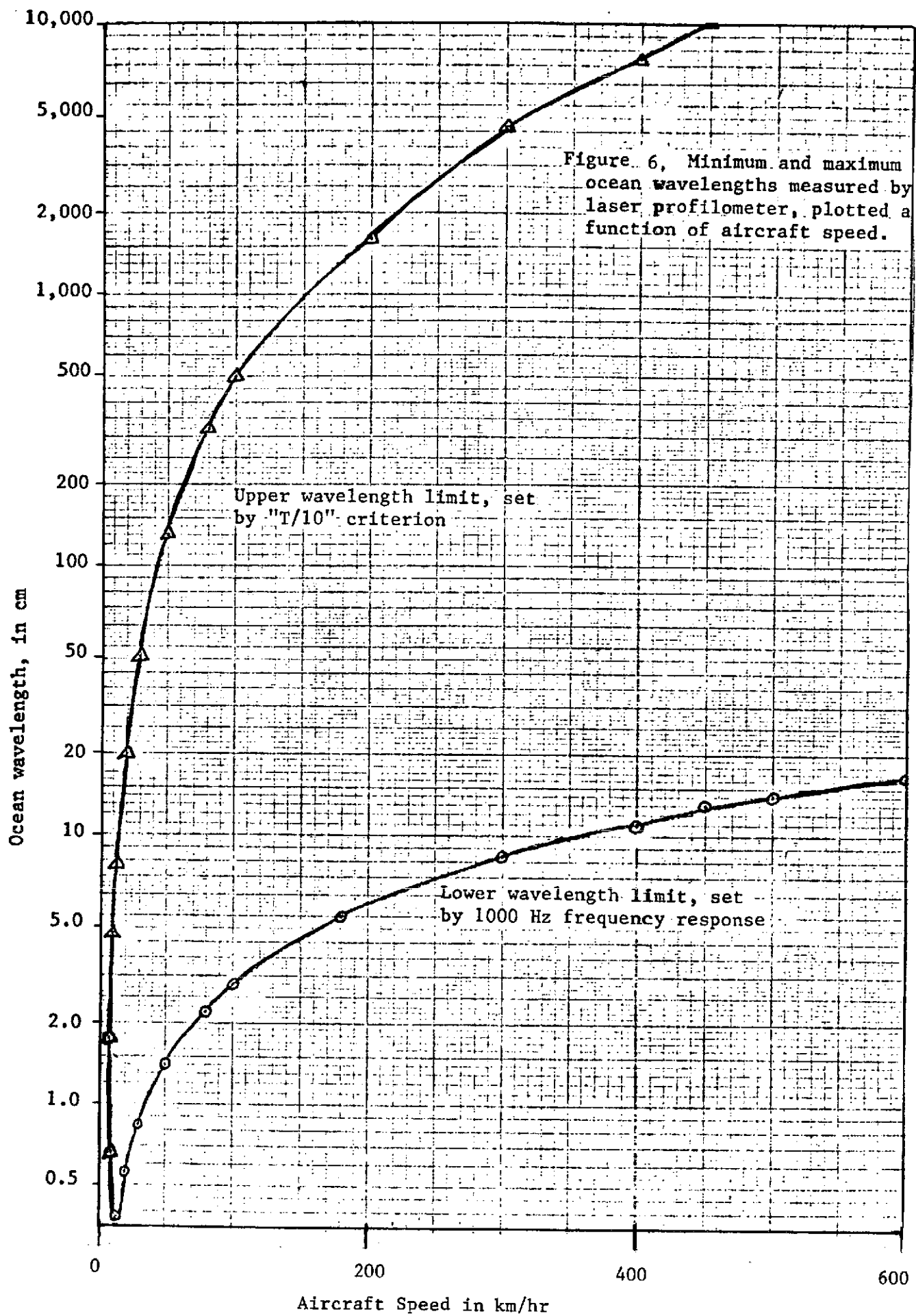
the ocean wave which can be derived approximately from the wave dispersion relation $\omega^2 = gk + sk^3$ where $g = 980$ cm/sec^2 and $s = 74$ cm^3/sec^2. Our basic approach is to get the wave number spectrum and surface properties directly from surface profile data insofar as possible and avoid use of the wave dispersion relation. The criterion of T/10 is quite arbitrary and is used here to provide a simple illustration of a typical upper wavelength limit imposed by a "nearly motionless sea" requirement.

Table I below lists λ_{min} and λ_{max} as a function of the profilometer speed. The entries in Table I are taken directly from Figure 6. (We are assuming the profilometer is translated at a constant speed and constant altitude above mean sea level, carried by a helicopter or by an aircraft, as appropriate to the speed finally chosen.)

Table I

Profilometer Speed/km/hr and knots	λ_{min}	λ_{max}
10 km/hr = 5.4 knots	0.66 cm	4.3 cm
50 km/hr = 27 knots	1.4 cm	130 cm
100 km/hr = 54 knots	2.8 cm	500 cm
300 km/hr = 162 knots	8.4 cm	4200 cm
450 km/hr = 243 knots	13 cm	10000 cm

On the basis of this information, it appears that a speed of about 50 km/hr would provide the type of information we need. This represents a compromise which provides two decades of wavelength (or of wave numbers) in the region of high probable interest to the radar problem. Lower speeds yield too stringent a λ_{max} limitation due to the "T/10 criterion," while higher speeds limit too severely the λ_{min} because of the instrument's frequency response. This speed of 50 km/hr of course assumes the availability of a helicopter to carry the profilometer. If an airplane only is available, the λ_{min} becomes higher because of the profilometer's frequency response.

Figure 6, Minimum and maximum ocean wavelengths measured by laser profilometer, plotted a function of aircraft speed.

Upper wavelength limit, set by "T/10" criterion

Lower wavelength limit, set by 1000 Hz frequency response

Ocean wavelength, in cm

Aircraft Speed in km/hr

It is clear that this proposed experiment is severely straining at the capabilities of the laser profilometer and that even a modest increase in both the vertical resolution and the bandpass of the device would greatly improve the chances of obtaining the data needed for experimentally investigating ocean surface geometry related to the sea-state bias problem. Even with the present instrument, this moving profilometer experiment seems the best hope in attempting to assess the bias problem by geometry measurements.

4.3.2 Pulse Amplitude vs. Time Experiments

We have already discussed the Yaplee experiment as providing the only experimental data available at this time for the bias problem. There are a number of open questions concerning this experiment, and the entire body of data available is still very small; this type of experiment should certainly be continued. It represents the best chance of getting the needed information, although the extrapolation of these results to deep water and to satellite geometry represents a large unknown area at this time.

It is interesting to consider a related experiment using the laser profilometer. If one argues that the radar scattering processes of interest to a radar altimeter are described by the class of electromagnetic theories which assume surface roughness large compared to the incident electromagnetic wavelength, then the incident laser radiation should serve as a very good test of these theories, and the laser backscattering cross-section at the ocean surface should vary in exactly the same manner as does the radar backscattering. This is a highly suspect argument since the ratio of laser to radar wavelength is so high and the illuminated spot size at the ocean surface so different. Selection of an appropriate spot size is much simpler at optical frequencies. A record of the laser profilometer's photodetector's output signal vs. time taken concurrently with the normal profilometer range vs. time signal might be very valuable. A cross-correlation of these two records would immediately give optical frequency backscatter cross-section as a function of sea surface height, leading to estimates of properties of the very high wave number end of the sea surface spectrum.

This return light amplitude vs. range experiment could be done at the same time the profilometer was being flown over the sea surface, or could be done at the Chesapeake tower with a fixed position profilometer. This would make a very valuable addition to further experiments with the NRL nanosecond radar, recording simultaneously the radar return data, the laser profilometer range output and photodetector output, as well as wave staff data.

4.3.3 Summary and Conclusion in the Bias Problems

In discussing the sea-state bias problem, we argued that the bias problem may be restated in terms of the vertical probability density $p(z)$ describing the "scattering element" distribution about mean sea level and discussed the relationship of the parameters appearing in rough surface scattering theories to this $p(z)$; if $p(z)$ is an even function of z, there is no sea state bias for a class of trackers including double delay differencing and 2:1 weighted split gates. We discussed possible experimental surface measurements from which $p(z)$ could be found without having to invoke the wave dispersion relation and concluded that only stereophotographs or moving profilometer techniques could get the needed information, and that the laser profilometer was the more promising of these. A flying laser profilometer can only measure without distortion a limited range of the entire ocean surface wave number spectrum and we presented the upper and lower surface wavelengths measurable for any given flying speed. Finally, we recommended an experiment correlating the laser profilometer photodetector output with surface height, and this probably should be done simultaneously with future Chesapeake light tower experiments using the NRL nanosecond radar.

The bias problem is a most complex one and all promising experimental approaches should be considered. If further tests can show that the nanosecond radar is observing individual scattering centers, or that the data can be suitably compensated, radar data will be of definite value to the bias problem. Note that it involves a minimum of theoretical assumptions. The laser technique merits further work and appears to offer the best opportunity for uncovering basic physical processes involved in the bias problem. Direct measurement of the bias error is of course recommended using over-water passive or active radar reflectors, once a satellite radar is in operation.

4.4 COMMENTS ON STILWELL'S DIRECTIONAL ENERGY SPECTRA OF THE SEA FROM PHOTOGRAPHS

Although the theoretical analyses presented in Chapter 3 clearly show that (for the purposes of backscattering computations) the wave height spectrum can be considered isotropic, such results must be experimentally verified. Therefore, the question of how best to obtain ocean spectral information is of vital concern to the altimeter program. At present, the Stilwell technique [8] and the laser profilometer method are considered to offer the most promising ground truth approaches: other proven methods for obtaining the wave number spectra such as stereophotography are not attractive because of the expense entailed.

This section presents the results of a brief investigation of the Stilwell technique, which was initiated with the objective of documenting characteristics of the method and specifying aircraft measurement procedures. In the course of the investigation, several questionable points in the Stilwell derivation were uncovered. These are discussed in detail below, in the order of their occurrence in the original paper. Until these deficiencies are incorporated into the derivation and the ensuing results shown to be related to an ocean slope spectrum we must plan on other ground truth methods.

Comment 1

Although the small-slope assumption is almost universally adopted in wave study, there is a real danger of using it in the present case.

The slope of a single train of waves whose height is given by $\zeta(x,t)$, where

$$\zeta(x,t) = a \cos (kx - \omega t), \tag{1}$$

is given by

$$\frac{\partial \zeta}{\partial x} = - a k \sin (kx - \omega t). \tag{2}$$

The magnitude of the slope is on the order of (ak) which is always small. However, for a random wave field, superimposed waves can make this assumption

questionable. For a random surface, the surface height is a superposition of all the elemental wave train amplitudes, i.e.,

$$\zeta(\underset{\sim}{x}, t) = \int\limits_{\underset{\sim}{k}} \int\limits_{\omega} dB(\underset{\sim}{k}, \omega) \; e^{i(\underset{\sim}{k} \cdot \underset{\sim}{x} - \omega t)} \tag{3}$$

where $dB(\underset{\sim}{k}, \omega)$ is a complex-valued random amplitude function of $\underset{\sim}{k}$ and ω. In this case the surface slope is

$$\nabla \zeta(\underset{\sim}{x}, t) = \int\limits_{\underset{\sim}{k}} \int\limits_{\omega} i \underset{\sim}{k} dB(\underset{\sim}{k}, \omega) \; e^{i(\underset{\sim}{k} \cdot \underset{\sim}{x} - \omega t)} \; . \tag{4}$$

Therefore, the slope is on the order of $|\underset{\sim}{k}| \zeta$. This quantity may be small for all observed $\underset{\sim}{k}$ in studies with emphasis on wave energy since most of the energy of a random wave field is contained in the low wave number range (see Figure 7). However, for wave slope studies, the major contribution comes from the higher wave number range, hence $|\underset{\sim}{k}| \zeta$ is not necessarily small for all $\underset{\sim}{k}$. The small slope assumption made by Stilwell seems to need additional study.

Aside

Before proceeding any further, it will be necessary to develop a relationship for the angle (θ) between the sun's ray and the vertical axis in terms of the angle (β_0) between the sun's ray and the local normal to the rough surface. Referring to Figure 8, we define the necessary geometrical quantities as follows;

$\underset{\sim}{r}$ = unit vector pointing to the camera
$\underset{\sim}{n}$ = unit normal to the sea-surface
$\underset{\sim}{s}$ = unit vector pointing toward the sun
$\underset{\sim}{i}, \underset{\sim}{j}, \underset{\sim}{k}$ = unit vectors in the x, y and z-directions, respectively
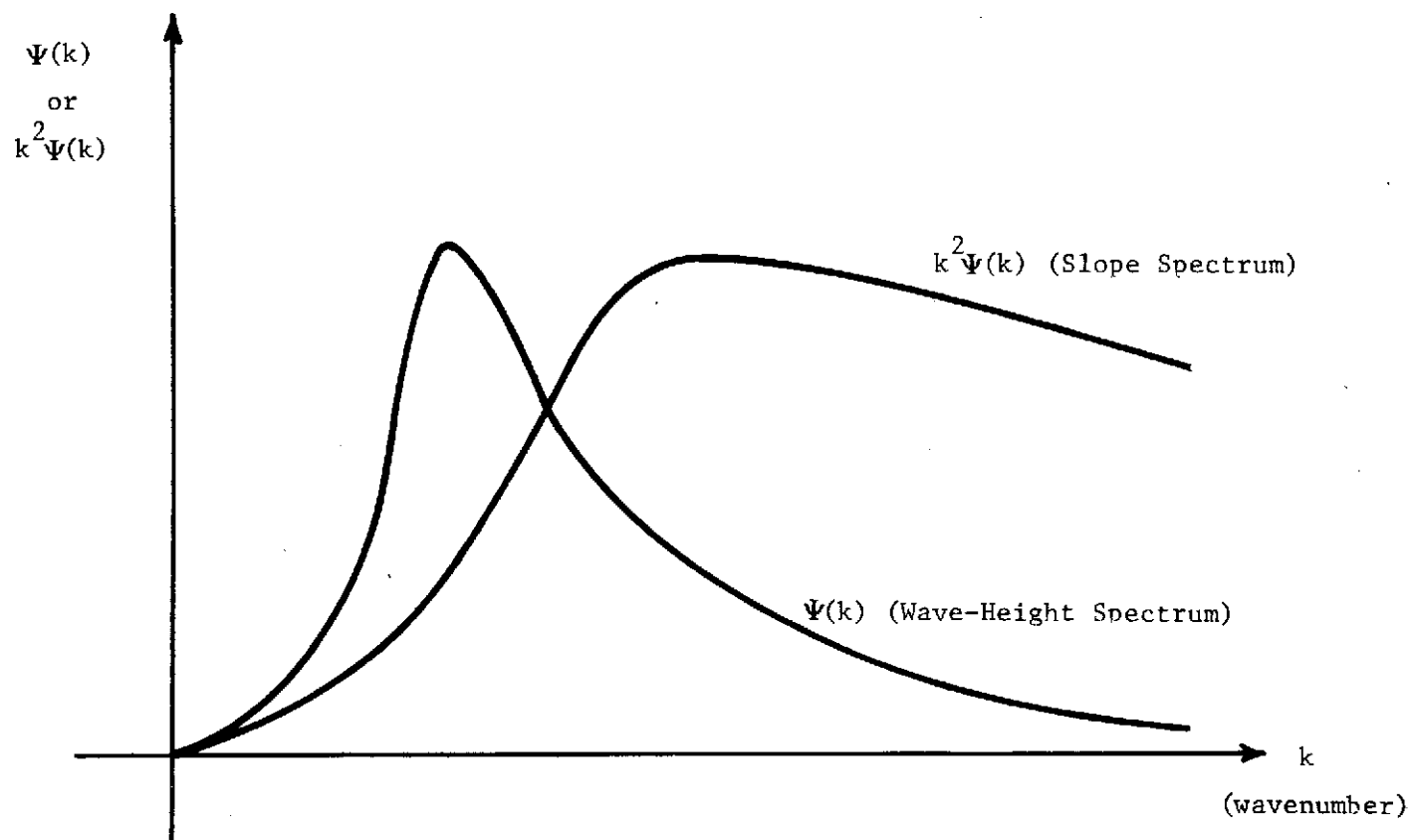$\underset{\sim}{r}, \underset{\sim}{n}, \underset{\sim}{s}$ are coplanar by definition .

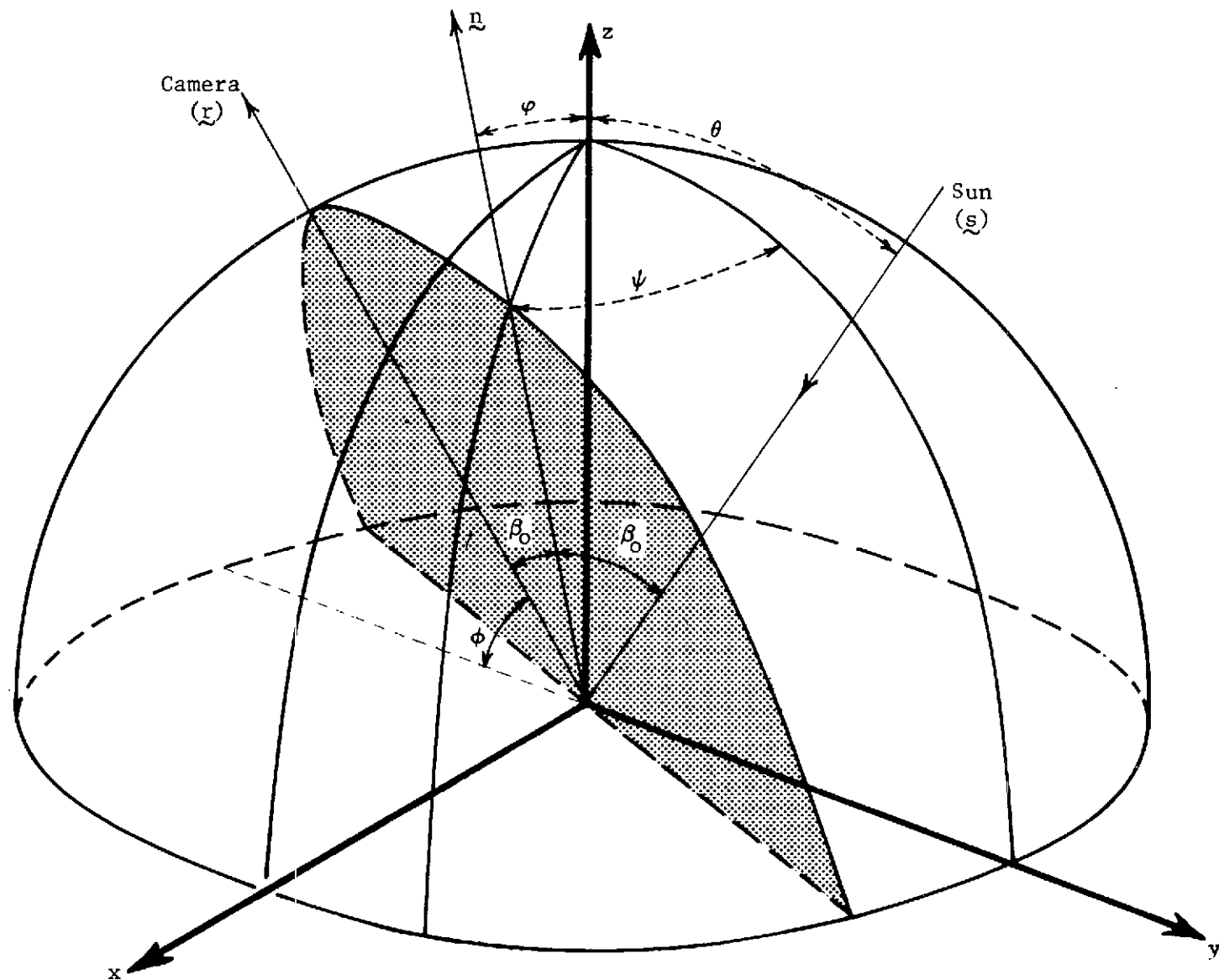Figure 7. Wave height and slope spectra as a function of wavenumber.

Figure 8. Ray reflection geometry.

From Figure 8, the unit vectors $\underset{\sim}{r}$, $\underset{\sim}{n}$ and $\underset{\sim}{s}$ may be reduced to their equivalent representation, i.e.,

$$\underset{\sim}{r} = -\cos\phi\underset{\sim}{j} + \sin\phi\underset{\sim}{k}$$

$$\underset{\sim}{n} = \sin\varphi\sin\psi\underset{\sim}{i} + \sin\varphi\cos\psi\underset{\sim}{j} + \cos\varphi\underset{\sim}{k}$$

$$\underset{\sim}{s} = \cos\beta_o\underset{\sim}{n} + \sin\beta_o\underset{\sim}{t}$$

where $\underset{\sim}{t}$ is a unit vector in the plane of $\underset{\sim}{r}$, $\underset{\sim}{n}$, $\underset{\sim}{s}$ and perpendicular to $\underset{\sim}{n}$. The angle θ is as follows;

$$\theta = \cos^{-1}(\underset{\sim}{s}\cdot\underset{\sim}{k})$$

or

$$\theta = \cos^{-1}\left\{\cos\beta_o\ \underset{\sim}{n}\cdot\underset{\sim}{k} + \sin\beta_o\ \underset{\sim}{r}\cdot\underset{\sim}{k}\right\} \qquad . \tag{5}$$

Thus, θ can be found once the unit vector $\underset{\sim}{r}$ is known. The most straightforward way of finding $\underset{\sim}{r}$ is to construct an orthogonal coordinate system comprising $\underset{\sim}{n}$, $\underset{\sim}{r}$ and $\underset{\sim}{n}^*$, where $\underset{\sim}{n}^*$ is perpendicular to $\underset{\sim}{n}$ and $\underset{\sim}{r}$ or

$$\underset{\sim}{n}^* = \frac{\underset{\sim}{n}\ \times\ \underset{\sim}{r}}{|\underset{\sim}{n}\ \times\ \underset{\sim}{r}|} \qquad . \tag{6}$$

From the definitions, it can easily be shown that

$$\underset{\sim}{n}\ \times\ \underset{\sim}{r} = (\sin\varphi\sin\phi\cos\psi + \cos\varphi\cos\phi)\underset{\sim}{i} - \sin\varphi\sin\phi\sin\psi\underset{\sim}{j} - \sin\varphi\cos\phi\sin\psi\underset{\sim}{k}$$

and

$$|\underset{\sim}{n}\ \times\ \underset{\sim}{r}|^2 = \sin^2\varphi\sin^2\phi + \cos^2\varphi\cos^2\phi + \sin^2\varphi\cos^2\phi(1 + \cos^2\psi)$$

$$+ 2\sin\varphi\cos\varphi\sin\phi\cos\phi\cos\psi \qquad .$$

The unit vector $\underline{r}$ is then given by the following

$$\underline{r} = \underline{n} \times \underline{n}^*$$

and $\underline{r} \cdot \underline{k}$ becomes

$$\underline{r} \cdot \underline{k} = - \frac{1}{|\underline{n} \times \underline{r}|} \left\{ \sin^2\varphi \sin\phi + \sin\varphi \cos\varphi \cos\phi \cos\psi \right\} \quad . \tag{7}$$

Substituting (7) in (5), there results

$$\theta = \cos^{-1} \left\{ \cos\beta_0 \cos\varphi - \frac{\sin\beta_0}{|\underline{n} \times \underline{r}|} \left[\sin^2\varphi \sin\phi + \sin\varphi \cos\varphi \cos\phi \cos\psi \right] \right\} \tag{8}$$

which is the desired relation.

Comment 2

The approximation to get from equation (s-4) to (s-5), i.e., for φ small, $\beta_0 \approx \theta_0$, is inaccurate. To prove this statement, we note that for small φ* equation (8) becomes

$$\theta \approx \cos^{-1} \left\{ \cos\beta_0 - \varphi\sin\beta_0 \cos\psi \right\}$$

or

$$\theta \approx \cos^{-1} \left\{ \cos(\beta_0 + \varphi\cos\psi) \right\}$$

and finally

$$\theta \approx \beta_0 + \varphi\cos\psi \quad . \tag{9}$$

---

*Small φ is equivalent to the small slope assumption.

Thus, we see that the approximation of $\theta \approx \beta_0$ is only zeroth order and the actual relation is directionally sensitive. In addition, it is not obvious that β_0 will be large when compared to $\varphi\cos\psi$. Equation (9) is only accurate to linear terms in φ and should not be used to compute derivatives. To see this, we note from (8) that

$$\theta = \cos^{-1}(\alpha) \tag{10}$$

or

$$\frac{d\theta}{d\varphi} = -\frac{\dfrac{d\alpha}{d\theta}}{[1 - \alpha^2]^{1/2}} \tag{11}$$

and

$$\frac{d\alpha}{d\theta} = -\sin\beta_0 \frac{d\beta_0}{d\varphi} \cos\varphi - \cos\beta_0\sin\varphi - \frac{\cos\beta_0}{|\underset{\sim}{n} \times \underset{\sim}{r}|} \frac{d\beta_0}{d\varphi} \quad [A]$$

$$-\frac{\sin\beta_0}{|\underset{\sim}{n} \times \underset{\sim}{r}|} \left[2\sin\varphi\cos\varphi\sin\phi - \sin^2\varphi\cos\varphi\cos\psi \right.$$

$$\left. + \cos^2\varphi\cos\phi\cos\psi \right] + \frac{A \sin\beta_0}{2|\underset{\sim}{n} \times \underset{\sim}{r}|^3} \left[2\sin\varphi\cos\varphi\sin^2\phi \right.$$

$$- 2\sin\varphi\cos\varphi\cos^2\phi + 2\sin\varphi\cos\varphi\cos^2\phi(1 - \cos^2\psi)$$

$$\left. + 2\cos^2\varphi\sin\phi\cos\phi\cos\psi - 2\sin^2\varphi\sin\phi\cos\phi\cos\psi \right]$$

where

$$A = \sin^2\varphi\sin\phi + \sin\varphi\cos \cos \cos\psi$$

$$\alpha = \cos\beta_0\cos\varphi - \frac{\sin\beta_0}{|\underset{\sim}{n} \times \underset{\sim}{r}|} \left[\sin^2\varphi \sin\phi + \sin\varphi\cos\varphi\cos\phi\cos\psi \right]$$

when φ is small,

$$|\underset{\sim}{n} \times \underset{\sim}{r}| \approx \cos\phi[1 + \varphi\tan\phi\cos\psi]$$

$$A \approx \varphi\cos\phi\cos\psi$$

$$\alpha \approx \cos\beta_o - \varphi\sin\beta_o\cos\psi$$

$$[1 - \alpha^2]^{1/2} \approx \sin\beta_o(1 + \varphi\cot\beta_o\cos\psi),$$

and (11) reduces to

$$\frac{d\theta}{d\varphi} \approx \frac{d\beta_o}{d\varphi} + \cos\psi + \varphi\left\{\cot\beta_o(1 + \cos^2\psi) + 2\tan\phi\sin^2\psi\right\} \tag{12}$$

and the approximation used by Stilwell, i.e.,

$$\frac{d\theta}{d\varphi} \approx \frac{d\beta_o}{d\varphi} ,$$

is not even a valid zeroth order approximation.

Comment 3

Equation (s-6), i.e.,

$$\frac{d\beta_o}{d\varphi} \approx \cos\psi \tag{13}$$

is once again only a zeroth order approximation. A more accurate expression may be derived by noting that

$$\beta_o = \cos^{-1}\left\{\underset{\sim}{r}\cdot\underset{\sim}{n}\right\}$$

4-30

or

$$\beta_o = \cos^{-1}\left\{-\cos\phi\sin\varphi\cos\psi + \cos\varphi\sin\phi\right\}$$ (14)

and

$$\frac{d\beta_o}{d\varphi} = \frac{\cos\phi\cos\varphi\cos\psi + \sin\phi\sin\varphi}{\left\{1 - [\cos\phi\sin\varphi\cos\psi - \sin\phi\cos\varphi]^2\right\}^{1/2}} \quad .$$

Under the small slope assumption,

$$\frac{d\beta_o}{d\varphi} \approx \cos\psi + \varphi\tan\phi\sin^2\psi \quad .$$ (15)

The difference between (13) and (15) is obvious. Since ψ is the angle between the y axis (which is arbitrary) and the horizontal projection of local surface normal (see Figure 8), its value is highly variable. When $\psi = \frac{\pi}{2}$ or $\frac{3\pi}{2}$, the leading term vanishes, hence the first order term dominates, especially when $\phi > \frac{\pi}{4}$.

One shortcoming of the zeroth order approximation (13) is that it creates an artificial blind-zone or false directionality in the derived spectrum since

$$\frac{d\beta_o}{d\varphi} = 0 \quad \text{for} \quad \psi = \frac{\pi}{2}, \frac{3\pi}{2} \quad .$$

The approximation shown in equation (13) could lead to severe distortion in a given measurement. Since signal strength depends on surface slope which, in turn, depends heavily on the high wave number waves; it is observed that

waves at high wave number tend to spread isotropically. Such observations are backed up by theoretical analysis (see, for example, Phillips [14]). An approximation in the form of equation (13) will limit the useful field to a narrow range.

Comment 4

The expansion in Equation (s-10) is incomplete. Since the photograph views a finite field,

$$I(\phi) = K \ L(\theta) \ \Gamma(\beta_o)$$

should at least be ϕ dependent. This is easy to see in a simple example. Let us take a perfectly smooth surface; then φ should be identically zero. By equation (s-10),

$$I = I_o = const.,$$

however, different reflection zones correspond to different ϕ angles. I_o is therefore altered as shown in Figure 9. Hence, I_o should be a function of ϕ and therefore position. This gradual change of ϕ will contribute to the low wave number end of the spectrum, not as a delta function at origin as the author claimed. This argument, of course, applies to the cases when φ is not identically zero. A consequence of this argument is to invalidate the claim at the bottom of Page 1978:

> "The light amplitude can be seen to consist of a constant term plus a term proportional to the normal angle φ of the wave system. The constant term will transform into a finite aperture equivalent of a delta function."

Comment 5

Equation (s-12)

$$\frac{dD}{d\varphi} = \bar{D}_\varphi = \frac{1}{2} \left(\frac{\delta D}{\delta \phi}\right) \tag{16}$$
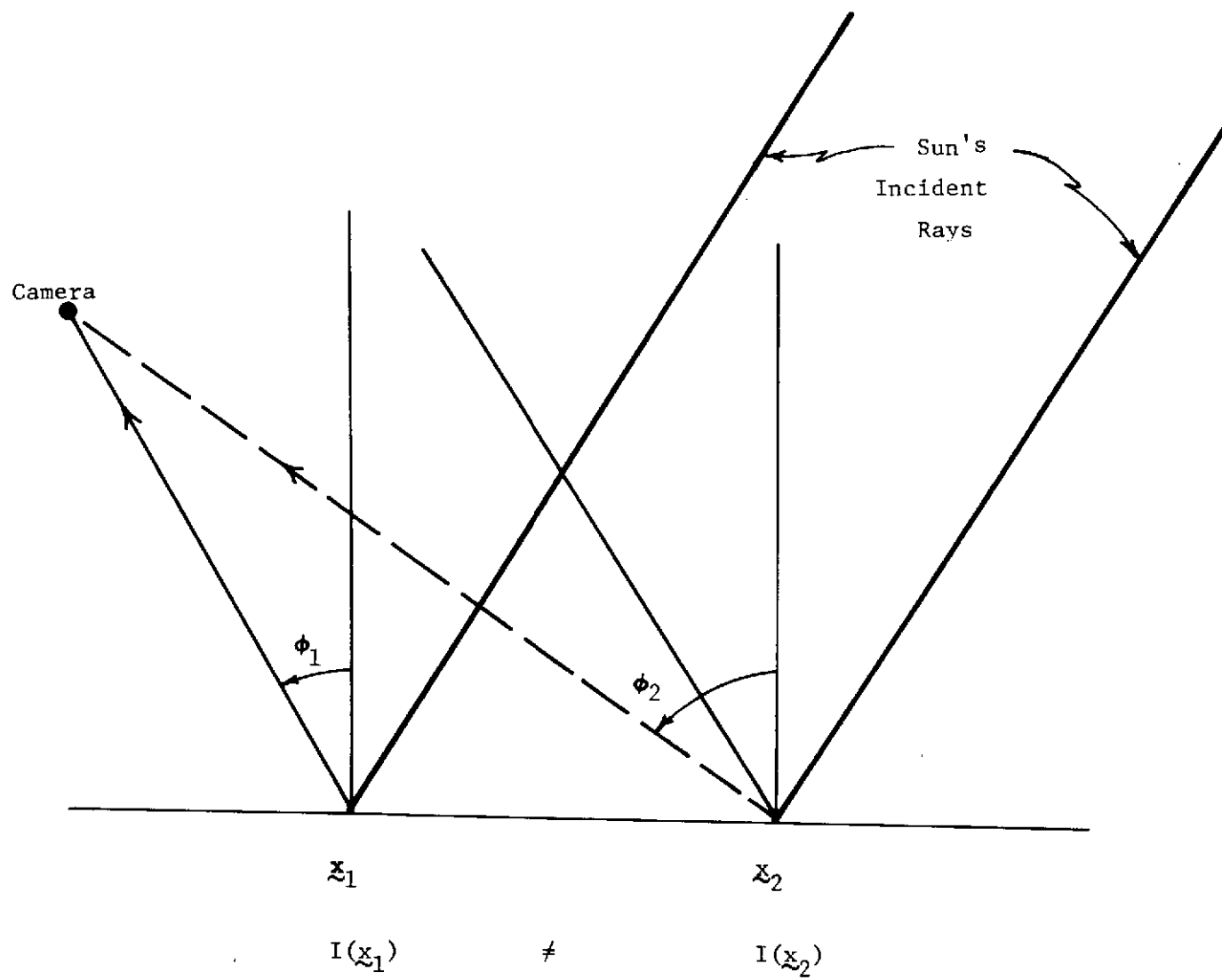
Figure 9.   Diagram illustrating the φ-dependence of the reflection process.

is only true for the two-dimensional case, i.e.,line scattering rather than surface scattering. For the three-dimensional case, the proper relation may be derived as follows. In order to relate $\frac{\partial D}{\partial \varphi}$, and $\frac{\partial D}{\partial \phi}$, use of the chain rule

$$\frac{\partial D}{\partial \varphi} = \frac{\partial D}{\partial \phi} \frac{\partial \phi}{\partial \varphi}$$

gives

$$\frac{\partial \phi}{\partial \varphi} = - \frac{\frac{\partial \theta}{\partial \varphi}}{\frac{\partial \theta}{\partial \phi}} \; .$$

With θ as given in equation (10),

$$\frac{\partial \theta}{\partial \phi} = \frac{\partial}{\partial \phi} \cos^{-1}(\alpha) = - \frac{\frac{\partial \alpha}{\partial \phi}}{(1 - \alpha^2)^{1/2}} \; .$$

To evaluate $\frac{\partial \alpha}{\partial \phi}$, knowledge of $\frac{\partial \beta_o}{\partial \phi}$ is also needed. From equation (14) it can be shown that for small φ,

$$\frac{d\beta_o}{d\phi} \approx -1 + \varphi^2 \tan^2\phi \cos^2\psi,$$

$$\frac{d\alpha}{d\phi} \approx \sin\beta_o + \varphi\cos\beta_o\cos\psi.$$

Therefore

$$\frac{d\phi}{d\varphi} \approx \frac{2 \sin \beta_o \cos\psi + \varphi\{3\sin \beta_o \tan\phi \sin^2\phi + \cos \beta_o (1 + \cos^2\psi)\}}{\sin \beta_o + \varphi\cos \beta_o \cos\psi}$$

$$= 2 \cos\psi + \varphi\{3 \tan\phi \sin^2\psi + \cot \beta_o \sin^2\psi\}.$$

It is, therefore, obvious that the connecting factor between $\frac{\partial D}{\partial \varphi}$ and $\frac{\partial D}{\partial \phi}$ is not a single constant $= \frac{1}{2}$, rather, it is a complex function.

REFERENCES

1. "A Study of the Capabilities of the Geodetic Satellite Altimeter to Measure Ocean Surface Characteristics," Final Report, Contract No. NASw-1909, Research Triangle Institute, April 1970.

2. Miller, L. S. and G. S. Hayne, "System Study of the Geodetic Altimeter Concept," Final Report, Contract No. NAS6-1829, Research Triangle Institute, March 1971.

3. Yaplee, Benjamin S., et al., "Nanosecond Radar Observation of the Ocean Surface from a Stable Platform," IEEE Trans. on Geoscience Electronics, Vol. GE-9, No. 3, pp. 170-174, July 1971.

4. Pierson, W. J. and E. Mehr, "The Effects of Wind Waves and Swell on the Ranging Accuracy of a Radar Altimeter," Report on Contract No. N62306-70-A-0075, New York University, School of Engineering and Science, January 1970.

5. Kodis, R. D., "A Note on the Theory of Scattering from an Irregular Surface," IEEE Trans. Antennas Propagation, Vol. AP-14, pp. 77-82, January 1966.

6. Schooley, A. H., "Upwind-Downwind Ratio of Radar Return Calculated from Facet Size Statistics of a Wind-Distributed Water Surface," Proceedings of the IRE, Vol. 50, pp. 456-461, April 1962.

7. Sledge, O. D. and S. F. George, "A Study of Sea-Return at Normal and Near-Normal Incidence," NRL Report No. 7005, Naval Research Laboratory, January 1970.

8. Stilwell, Denzil, Jr., "Directional Energy Spectra of the Sea From Photographs," Journ. of Geophys. Res., Vol. 74, No. 8, pp. 1974-1986, April 1969.

9. N. F. Barber, "The Directional Resolving Power of an Array of Wave Detectors," in Ocean Wave Spectra, Englewood Cliffs, New Jersey: Prentice-Hall, Inc., 1961.

10. L. J. Cote et al., "The Directional Spectrum of a Wind Generated Sea as Determined from Data Obtained by the Stereo Wave Observation Project," Meteor. Papers Vol. 2, No. 6, New York University College of Engineering, 1960.

11. I. Katz, "Ocean Wave Measurements," APL Technical Digest 3, 2-6, 1964.

12. G. R. Valenzuela and E. B. Dobson, "Radar Scattering from the Sea," Research and Development Programs, Applied Physics Lab, Johns Hopkins Univ., Silver Springs, Md., March, 1967.

13. E. B. Dobson, "Measurement of the Fine-Scale Structure of the Sea,"
     J. Geophys. Res. 75, 2853-2856, 1970.

14. Phillips, O. M., "The Dynamics of the Upper Ocean," Cambridge University
     Press, London and New York, 1966.